UNIVERSITÀ DI PARMA

UNIVERSITA' DEGLI STUDI DI PARMA

DOTTORATO DI RICERCA IN

"SCIENZE CHIMICHE"

CICLO XXXV

CELLULOSE NANOCRYSTALS:

FROM EXTRACTION TO APPLICATIONS

Coordinatore:

Chiar.ma Prof.ssa Alessia Bacchi

Tutore:

Prof.ssa Claudia Graiff

Co-Tutore:

Prof.ssa Laura Bergamonti

Dottoranda: Marianna Potenza

Anni Accademici 2019/2020 – 2021/2022

Ai nostri sorrisi..

STRUCTURE OF THE THESIS

The research activity has been focused on the development of innovative materials for application in different fields: cultural heritage, medicine, environmental and building. This work can be divided in two parts: the first part regards the extraction, functionalization, characterization and application of cellulose nanocrystals-based materials; the second part concerns the development of geopolymer materials for sustainable building.

Part I is divided into three chapters:

- Chapter 1:

The first Chapter is focused on the possibility of extracting nanocellulose from different sources, such as cotton, wastepaper and waste from agricultural production. Particular attention has been paid to the characterization of the obtained products to establish the morphology, the type of polymorph and the degree of crystallinity of each sol. Some surface functionalizations of the nanocrystals are presented, with particular attention to the presence of the newly added functional groups. The ability of nanocellulose to act as a carrier for silver nanoparticles, whose biocidal activity against gram+ and gram- bacteria has been reported, is also studied;

- Chapter 2:

The second Chapter regards the application of nanocellulose suspensions as new and sustainable material as preservative and consolidant for lignocellulosic substrates in the field of cultural heritage. The ability to not alter the substrate chromatically, before and after accelerated artificial ageing cycles, and the mechanical properties of the treated samples have been evaluated. The results

obtained have been compared with those observed by using Aquazol 500, a commercial product still utilized in restoration;

- Chapter 3:

In the last Chapter two different matrices based on nanocellulose are proposed for medical and environmental applications, respectively. For the first application, 3D printed hydrogel scaffolds made of nanocellulose and alginate, mixed with silver nanoparticles to promote antimicrobial action are studied. For the second type of application, three-dimensional hydrogel scaffolds, made of carboxymethylcellulose mixed with nanocellulose, obtained by freeze-thaw method, for the removal of heavy metals in water are presented.

LIST OF ACRONYMS

CNC: Cellulose Nanocrystals

CNC-CL: Cellulose Nanocrystals extracted from cotton linter

CNC-WP: Cellulose Nanocrystals extracted from wastepaper

CNC-H: Cellulose Nanocrystals extracted with hydrochloric acid

CNCII: Cellulose Nanocrystals polymorph II

CMF: Cellulose Micro Fibrillated

CMC: Carboxymethylcellulose

TOCNC: TEMPO oxidate cellulose nanocrystals

TEMPO: 2,2,6,6-Tetramethylpiperidine 1-oxyl

APTES: 3-Aminopropyl triethoxysilane

PDMS: Polydimethylsiloxane

EDC HCl: 1-ethyl-3-(3-di- methylaminopropyl) carbodiimide hydrochloride

NHS: N-hydroxysuccin-imide

PVA: Poly vinyl alchol

Culminal $_{8367\text{-}1500\text{-}6000}$: commercial methyl cellulose (viscosity number subscript)

MK: metakaolinite

$S_{505\text{-}510}$: silica sand

$PV_{0,5\text{-}2}$: expanded glass

Dynamon SR4: superplsticizer

Dehscofix: plasticizer, water reducing agent

Starvis S35F: water reservoir

Silopon 8010: air entraining agent

L1-6: geopolymer binder for mortar

LP1-7: geopolymer binder for plaster

M1-M8: geopolymer mortar

INDEX

PART I

EXTRACTION, FUNCTIONALIZATION, CHARACTERIZATION AND APPLICATION OF CELLULOSE NANOCRYSTALS-BASED MATERIALS

1- Introduction

1.1- Cellulose, nanocellulose, extraction and functionalization of nanocrystals

Cellulose

Cellulose is the most abundant biopolymer produced on earth[1], it is present in higher plants, marine animals (tunicates) and algae, fungi, bacteria, invertebrates. It was first isolated in 1838[2]. Cellulose appears as a high molecular weight homopolymer, whose anhydro-D-glucose units are linked by a-1,4 bonds, rotated by 180°. The number of glucose units or degree of polymerization (DP) is up to 20.000[3]. Figure 1 shows the chemical structure of cellulose. Two glucose units form the repeating segment known as cellobiose. In each cellobiose moiety there are six hydroxyl groups able to form inter and intramolecular hydrogen bonds. Each cellulose chain possesses an asymmetry about its molecular axis: one end is a chemically reducing functionality and the other has a pendant hydroxyl group, the nominal non-reducing end. It is known from the literature that approximately 36 cellulose chains aggregate to form protofibrils which led to the

formation of microfibrils, that in turn form fibers that are the basis of plant cell walls[4].

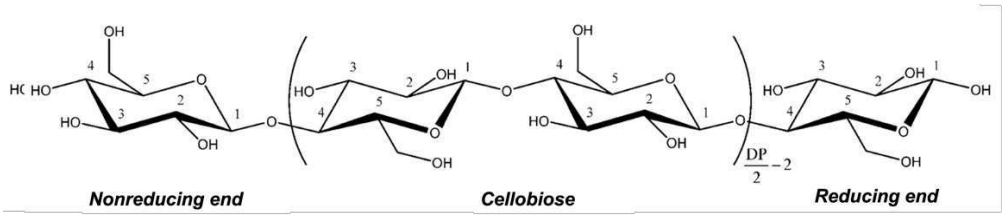

Figure 1- Cellulose structure

Cellulose can occur in four different polymorphs: cellulose I, cellulose II, cellulose III and cellulose IV. The most common are polymorph I and polymorph II. Crystal packing of polymorph I is characterized by parallel chains. Polymorph I is then divided in two crystalline phases: polymorph Iα is present in bacterial cellulose and polymorph Iβ is typical in wood cellulose. The conversion of polymorph I to polymorph II can take place irreversibly by mercerization with NaOH acqueous solution at high percentage concentrations or by chemical regeneration with a suitable solvent and reprecipitation. Polymorph II has a more rigid structure due to the anti-parallel arrangement of the chains; this characteristic is exploited in paper industry[5]. Type III cellulose is obtained by treating polymorphs I or II with liquid ammonia (at low temperature) or organic amines, such as ethylenediamine (EDA); the transformation is reversible. Polymorph IV is obtained by high temperature treatment of polymorph III.

Nanocellulose extraction

Cellulose nanocrystals (CNC) are advanced biomaterials obtained by chemical or mechanical treatments of cellulose. The term nanocellulose refers to cellulosic extracts having structural dimensions on the nanometric scale. Even if the structure of the cellulose appears ordered, there are some amorphous areas that

result from the distortion of the fibers. The removal of these zones takes place on the hydroxyl groups –OH, that can be esterified by organic or inorganic acids, and on the oxygen atom of the glycosidic bond, that can be broken by mechanical or chemical treatment. As a result, partially crystalline nanocellulose is obtained. According to the type of treatment applied for the extraction, and to the cellulose source, three different nanocelluloses can be obtained: (i) nanocrystalline cellulose (CNC), mainly obtained by chemical treatment of cellulose, (ii) nanofibrillated cellulose (CNF), obtained by mechanical disaggregation of cellulose, (iii) bacterial nanocellulose (BNC), produced by some bacteria, such as *acetobacter*. Nanocrystalline cellulose (CNC) is the most widespread: its nanocrystals have a diameter of 2-30 nm and a length of several hundred nanometers. Cellulose nanocrystals exhibit interesting properties such as large surface area, high elastic modulus, high thermal stability and optical clarity, biocompatibility, non-toxicity and low production cost. They are obtained during the acid hydrolysis of the cellulose fibers due to the degradation of the glycosidic bonds of the amorphous areas which are more easily attacked by the acid. The cellulose sources suitable for extraction can be of different kinds and among these are wood pulp, cotton, wheat straw, algae, banana fibers, sugar beet[6]. The most commonly used acids for hydrolysis are sulfuric acid, hydrochloric acid, hydrobromic acid, phosphoric acid or a mixture of acids. As regards the reaction with sulfuric acid, this reagent is consumed, in addition to the catalysis of the hydrolysis, in the formation reaction of the sulfuric ester between the primary OH of the glycosidic ring and the acid itself. The colloidal solutions of nanocrystals produced are stable thanks to the electrostatic repulsion of the sulphate anions present on the surface of the crystals, originated by the treatment. Two reaction mechanisms for the acid hydrolysis, shown in figure 2, are reported[7]. Hydrolysis with hydrochloric acid[8] (figure 3), does not modify the

primary hydroxyl groups of cellulose, therefore non-functionalized nanocrystals are produced.

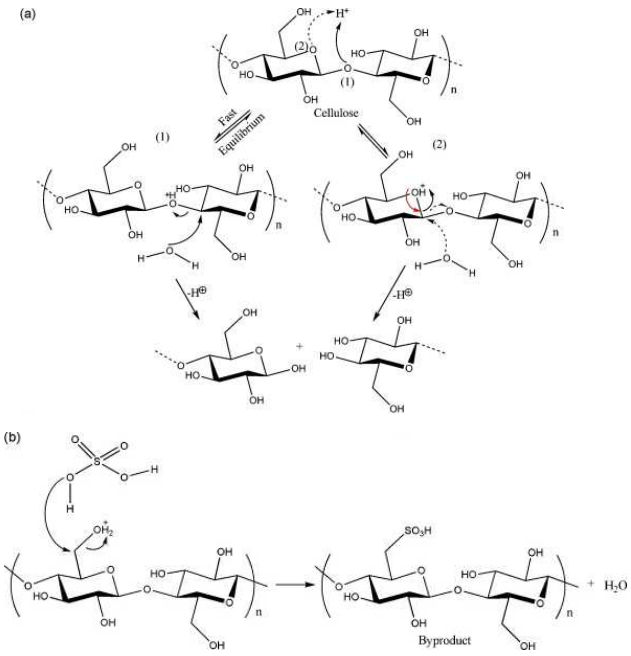

Figure 2- a) Acid hydrolysis and b) esterification with sulfuric acid [7]

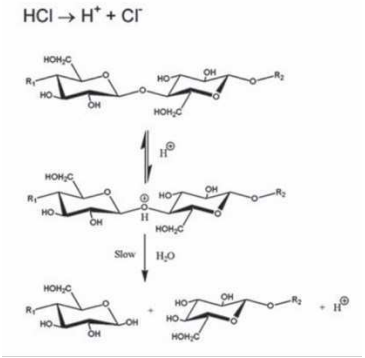

Figure 3- Acid hydrolysis with hydrochloric acid[3]

Surface functionalizations of nanocellulose

Nanocellulose can be chemically functionalized[3,9] to modify and improve its properties. The presence of numerous surface -OH groups make esterification, oxidation, anchoring of polymers, etc., easily feasible (figure 4). All these chemical functionalization reactions aim to introduce reactive functional groups or surface charges. The change must occur exclusively on the surface, maintaining the original morphology, avoiding a polymorphic conversion and maintaining the integrity of the crystalline structure[3].

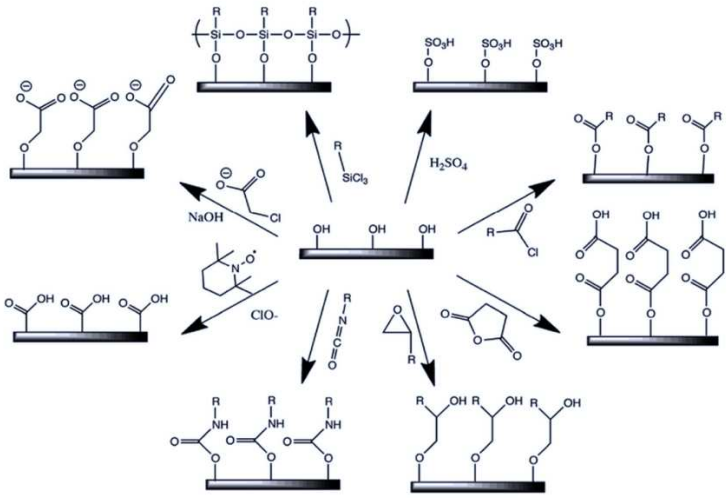

Figure 4- Possible surface functionalizations of cellulose nanocrystals

Below are reported two types of possible functionalizations that have been tested during this research: covalent modifications, in which the primary OH groups on the surface are substituted, and non-covalent modifications, in which the molecules are adsorbed on the surface of the nanocrystals through electrostatic and van der Waals interactions.

Covalent functionalizations concern the possibility of introducing molecules on the primary alcohol group, for example using the 3-Aminopropyl triethoxysilane (APTES) (figure 5): the primary hydroxyl group of the glycosidic rings are reacted with this molecule following the reaction proposed by Khanjanzadeh[10]. The reaction can be divided in 3 steps: hydrolysis of the alkoxide groups of the starting silane to give the corresponding silanol; adsorption of silanols on the surface of the nanocellulose substrate; condensation reaction between silanol OH and between silanol OH and primary cellulosic OH. The amino group (of the initial APTES) is then grafted onto the nanocellulose via Si-O-C siloxane bond and furthermore the creation of a 3D network around the nanocellulose via Si-O-Si bonds occurs.

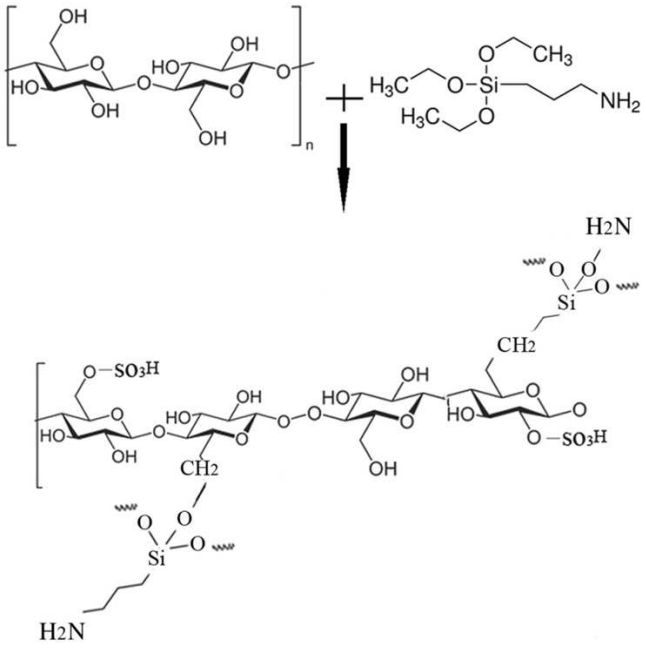

Figure 5- Functionalization of cellulose nanocrystals with APTES[11]

One of the most investigated CNC functionalizations is the oxidation of the primary hydroxyl group to a carboxyl group. The oxidation mediated by 2,2,6,6-TetraMethylPiperidine-Oxyl (TEMPO) is the most studied oxidation method[12] (figure 6). TEMPO is a commercially available, stable, water-soluble nitroxyl radical. This is a highly selective oxidation: primary hydroxyl groups are converted into the carboxyl form, mediated by TEMPO in the presence of NaBr (co-catalyst) and NaClO (primary oxidant). Optimal conditions are pH 10 and temperature between 0 and 10 °C. These conditions allow oxidation on the nanocrystals surface, leaving the internal structure of the crystal unchanged.

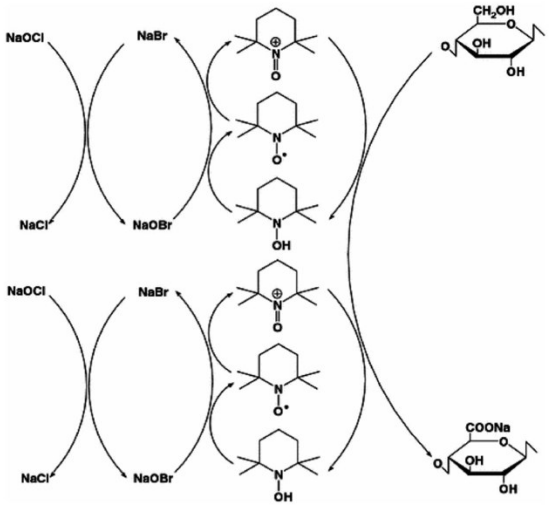

Figure 6- Reaction of CNC oxidation with TEMPO[3]

The surface charges of nanocellulose can impart specific properties to the suspensions. In this regard nanocellulose suspensions can be used as carrier for metal nanoparticles[13]. Made these premises, the present work aims to study the possibility of extracting nanocellulose starting from different sources, such as cotton, wastepaper and agricultural production waste. The characterizations of the products obtained have allowed us to define the goodness of the reactions and to study the morphology, the type of polymorph and the degree of crystallinity of

the samples. Some surface functionalization reactions of the nanocrystals have been investigated, with particular attention to the presence of the newly added functional groups, such as carboxylate negatively charged groups. The ability of nanocellulose to act as a carrier for silver nanoparticles has been also studied.

1.2- Nanocellulose-based materials for consolidation of ligno-cellulosic artworks

Considering the interesting properties of nanocellulose (in particular the mechanical resistance, the transparency, the gas and vapor barrier and the possibility of functionalization), its suspensions can be considered versatile material for different uses in the field of cultural heritage. Cellulose nanocrystals have recently been introduced in the restoration thanks to their natural affinity with the cellulose of the substrates of many artworks: wood, natural textile fibers and paper[13–15]. Moreover, the interest of nanocellulose derives from the low environmental impact and the non-toxicity for the operators. These parameters satisfy the stringent regulations on the use of chemical products. Other aspects to highlight are the preventive restoration and minimum intervention. In the last decades a progressive decrease of invasive approaches in the restoration of works of art has been observed[16]. Attention has been paid to the importance of prevention and to the introduction of external materials into artifacts in very limited quantities. Great attention has been paid to nanostructured materials, thanks to their high surface area, which allows the use of minimal quantities, obtaining very high efficiency[17]. Thanks to its properties, nanocellulose can be used in this context: for example, it can be utilized as consolidant for lignocellulosic substrates such as paper and canvas paintings. The nanocellulose can provide reinforcement to the degraded cellulose fibers of the substrates, avoiding invasive operations. It is important to note that in a painting, in addition

to the cellulose fraction, there are other materials that form different layers[18–20] (figure 7):

- canvas (linen, cotton, hemp, jute, etc.) tied to a frame;
- animal glues or starch to stiffen the canvas and fill the interstitial voids;
- preparatory layer consisting of plaster and animal glue, white lead and linseed oil, calcium carbonate, flour, etc., to provide a smooth and homogeneous surface for the painting;
- a pictorial layer with mineral or organic pigments and a binder (linseed oil, animal glue, egg, milk, etc.);
- varnish (terpene resins to protect the color layer).

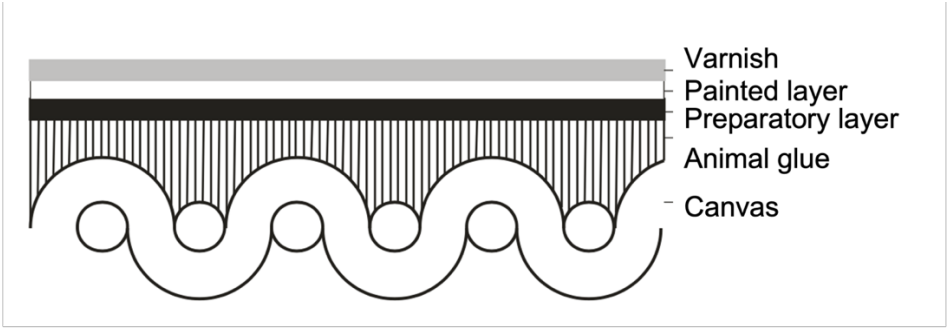

Figure 7- Description of painting canvas layers

The first cause of deterioration of cellulose-based materials concerns the photochemical reactions or oxidation of the hydroxyl groups. When the carboxyl is formed, it can dissociate, and the proton catalyzes the hydrolysis of the glycosidic bond, causing a chain scission. A progressive depolymerization of the chains is noted, with a decrease in the mechanical properties[21].

Some researchers used nanocellulose and functionalized nanocellulose for consolidation of paper[13] and painting canvas[22–24]. The products were applied in suspension and after evaporation of the solvent, were deposited on the surface of

the fibers, forming dense and cohesive films. This implemented the Young's modulus and tensile strength of the degraded substrate, especially after multiple treatment cycles. Furthermore, it has been observed that this material does not cause any transformations in the appearance of the original canvases, even after changes in relative humidity[24].

Despite the advantages deriving from the use of nanocellulose, it must be considered that the aqueous medium represents a problem for the works of art. Studies are few and many problems remain open. For example, it should be important to understand if the amount of water on artistic artefacts can be reduced using application methods (nebulization, rigid gels…); if the high surface area and the reactivity of the product can favor oxidation phenomena and lead to the development of acid groups during ageing; if the functionalization can bring advantages in terms of product reversibility, dispersion in a wider range of solvents, reduction of hydrophilicity.

The present work aims to add a piece to the knowledge of the behavior of nanocellulose as a consolidant for paper and painting canvas. For comparison, the behavior of commercial material currently used in the restoration, was evaluated. The phenomenon of accelerated artificial aging was investigated to evaluate if the consolidants lead to changes of mechanical resistance of the cellulosic fibres. In addition, any chromatic variations caused by the consolidants used were evaluated. The results obtained before and after artificial ageing were compared.

1.3- Three dimensional scaffolds based on nanocellulose for application in medical and environmental fields

Due to growing environmental problems, the use of renewable and sustainable biopolymers to design environmentally friendly matrices has been extensively

explored. These supports can be applied in environmental (i.e. wastewater remediation), pharmaceutical (i.e. drug delivery systems), medical (i.e. regenerative medicine) and many other fields [25–27].

Biopolymers, due to their properties such as low density, low cost, easy availability also from renewable sources, biodegradability and easy processing, have aroused great interest among researchers, as a possible alternative to synthetic polymeric materials. The most used biopolymers for the creation of tailored structures are cellulose, chitosan, alginate, polylactic acid and its derivatives, to name a few. In the medical field, the development of innovative biomaterials for advanced therapeutic solutions is of great concern. Innovative devices based on biopolymers for the treatment of infected wounds are particularly interesting[28,29]. Alginate is a biocompatible polysaccharide found in the cell walls of brown algae[30]. It has been used for many medical devices, due to its low toxicity, biocompatibility and mild gelling ability after addition of divalent cations[31,32]. Cellulose nanocrystals due to their high surface area and crystallinity, good mechanical properties and biocompatibility are good candidate to be used in biomedical applications and especially in the use of 3D printing for tissue engineering and wound healing scaffolds[3,26]. Nanocellulose mixed in the formulation with alginate improves the elasticity and fracture resistance of the scaffolds. Silver is a broad-spectrum antimicrobial agent, which uses various non-specific mechanisms and is therefore suitable for overcoming the problem of antibiotic resistance[33,34]. The incorporation of silver nanoparticles in alginate-based hydrogels reinforced with cellulose crystals combines the biocidal properties of metal nanoparticles with the physical characteristics of the hydrogel. Hydrogel scaffolds with a well-defined 3D structure, were builded by a method developed by Elviri et al[35].

In the environmental field, due to the increase of the air and water pollution, the development of new technology based on ecofriendly material and processes, has become a priority. In recent decades, the contamination of aqueous systems by toxic heavy metals has become a serious environmental problem. Even at trace level these metals can cause ecological and health damage, due to their toxicity and bio-accumulation tendency, high solubility and stability in aqueous media, migration activity. Among the various processes employed to remove heavy metals from water systems adsorption is one the most used and effective techniques[36]. The removal of pollutants from wastewater and the study to develop their purification represent the challenges to improve the quality of water[37,38]. Fundamental parameter to consider is that the adsorbent material is not released into the environment during the pollutant removal activity in the water. One solution could be the immobilization of biopolymers forming membranes or hydrogels[39–41]. In this work, a simple and effective method is proposed which involves the use of freeze-thaw cycles on carboxymethylcellulose as a substrate for the formation of a stable hydrogel scaffold, obviating the use of further polymers or crosslinkers[42–45]. The efficiency of this material is then studied with the possibility of implementing its adsorbent capacity with the interaction with functionalized cellulose nanocrystals and with its different polymorphs[36,46]. Moreover, the nanocellulose and its functionalized suspensions have been employed in the preparation of the hydrogel to increase the intrinsic mechanical properties of this biopolymer (elasticity and resistance to breakage)[46]. In hydrogels produced using carboxymethylcellulose there is the advantage of using a matrix that interacts with nanocellulose and acts as a cross-linker through intermolecular or covalent interactions. A further advantage is offered by the improvement of the mechanical properties given by the synergy of the cellulose-based materials used, which allows us to obtain a compact and stable hydrogel over time.

CHAPTER 1

CNC EXTRACTION, CHARACTERIZATION AND SURFACE FUNCTIONALIZATION

1- Abstract

This Chapter mainly regards the extraction methods of nanocrystalline cellulose from different sources. Cotton, wastepaper and biomass from agricultural wastes have been considered. Several factors[47]such as nature of the acid, temperature, reaction time, acid/cellulose ratio have been taken into account. Sulfuric acid and hydrochloric acid have been primarily utilized as reagents. Time and temperature of the hydrolysis reactions have also been considered, observing that high temperatures lead to reduced reaction times, reduced dimensions of the nanocrystals and consequent increase in surface charges. High reaction times together with a high acid/cellulose ratio resulted in a tighter size distribution of the nanocrystals[48]. Cellulose polymorph II has been obtained by irreversible chemical regeneration of cellulose I, through mercerization with NaOH[49]. Polymorphs Iβ and II have been extensively characterized by means of spectroscopic and diffractometric methods. The crystallinity index and the thermal stability have also been evaluated.

Cellulose nanocrystals have been functionalized to obtain new materials with interesting properties. The modification of nanocellulose can be different: there

can be non-covalent modifications, in which small molecules or macromolecules are adsorbed on the surface of the nanocrystals by exploiting the electrostatic and van der Waals interaction, or covalent modifications where the primary OH groups are replaced on the units of surface glucose. Part of the research was then dedicated to finding the optimal conditions to carry out the selective oxidation of nanocellulose using the TEMPO reagent. In this system the reaction conditions have been modified, paying attention to the influence of the co-catalysts. This reaction allowed to obtain CNC with carboxylic surface functions, high surface charge and consequently different reactivity, compared to the unmodified CNC, and represented the starting material for a further reaction involving EDC-NHS system, leading to the formation of a pendant amide groups on the nanocrystals. A second type of modification of nanocellulose regarded the mixing of CNC aqueous suspensions with different materials imparting specific properties. CNC suspensions have been mixed with polymers such as PDMS, obtaining products with interesting hydrophobic function. Finally, the ability of CNC to act as a carrier for metal nanoparticles was explored. CNC suspensions have been mixed with silver nanoparticles, whose biocidal activity against gram $^{+}$ and gram $^{-}$ bacteria has been investigated.

2- Experimental

2.1- Materials

Cotton linter was purchase by Parchin Chemical Industries Co., Tehran, Iran, the recycled paper was Palucart®. Sulfuric acid (95–97%, Merk, Darmstadt, Germany) and Hydrochloric acid (Fluka, Darmstadt, Germany) were used for the hydrolysis. The dialysis tube (cellulose membrane, molecular weight cut-off 10000-12000 Da) was used for the purification. Cellulose microfibrillated was purchased by Arbocel ® R 200. The artichoke waste was purchased in local

market. Sodium hydroxide and sodium bicarbonate (Carlo Erba, Emmendingen, Germany), glacial acetic acid, sodium chloride and ethanol (Merck, Darmstadt, Germany), were used for separation of cellulose from *Cynara* stems and bracts. The oxidation reaction involves the use of 2,2,6,6-Tetramethylpiperidine 1-oxyl (TEMPO), and MeOH (Merck, Darmstadt, Germany), NaBr and NaClO (Carlo Erba, Emmendingen, Germany). The reaction with EDC, NHS involves the use of Ethylendiamine, N-hydroxysuccin-imide (NHS), 1-ethyl-3-(3-di-methylaminopropyl) carbodiimide hydrochloride (EDC·HCl), Triethylamine and Ethyl acetate (Merck, Darmstadt, Germany), Dichloromethane (VWR Chemicals BDH®). $AgNO_3$ and Poly vinyl alchol (PVA) (Merck, Darmstadt, Germany), and $NaBH_4$ (Carlo Erba, Emmendingen, Germany) were used for the silver nanoparticles sol. (3-Aminopropyl) triethoxysilane (APTES) (Merck, Darmstadt, Germany), were used to impart chain with terminal NH_2. Polydimethyl siloxane (PDMS) (Merck, Darmstadt, Germany) gives the hydrophobicity.

2.2- CNC extraction from cotton linter

The extraction of CNC was carried out by hydrolysis using H_2SO_4 (64%) or HCl. The acid/sample ratio was 8.75 ml g^{-1} for each hydrolysis[13]. Time and temperature for the reaction were included in 40-60 °C and 30-60 minutes range. The acid, the temperature and the reaction time have been varied to ensure better reaction efficiency. The reaction was quenched with ice water (5:1 (v/v) ratio with acid) and left to cool at room temperature. The products were washed repetitively with distilled water in order to resuspend the nanocrystals, after centrifugation. The sols obtained were purified in dialysis tube, for one week, until neutral pH. The sols were called CNC-CL and CNC-H for CNC obtained from cotton linter in sulfuric acid hydrolysis and CNC obtained in hydrochloric acid, respectively.

2.3- CNC extraction from wastepaper

This extraction was performed modifying time, temperature and acid concentration, respect to the extraction from cotton linter, to allow the reaction to take place in a controlled way. The acid/sample ratio was maintained at 8.75 ml g^{-1}. The reaction temperature was maintained at 45 °C for 30 minutes and the sulfuric acid was diluted at 40 wt%. The procedure to obtain CNC was the same as reported above. The final suspension was called CNC-WP.

2.4- Reaction of mercerization

The use of NaOH solution (20%) at 60 °C for 2 h allows to obtain polymorph II from microfibrillated cellulose powder. To remove the excess of sodium hydroxide, the samples were washed several times with distilled water, until neutral pH. The powder, obtained by evaporation, was called CMF II. Hydrolysis with sulfuric acid (following the procedure described in paragraph 2.2), led to the formation of stable suspension called CNC-MF.

2.5- CNC extraction from Cynara scolymus L.

The use of a high concentration alkaline treatment is a fundamental step for the removal of lignin from raw samples. At the same time this allows to obtain the polymorph II of cellulose and after acid hydrolysis, the suspension of CNC II (CNC polymorph II). Therefore, to eliminate the parts that are not of interest and obtain pure cellulose to be processed further, an alkaline treatment of the sample is foreseen. In detail, the artichokes waste was washed in water at 40 °C, dried in a ventilated oven at 40 °C for 24 hours and finally minced. Two different

procedures were tested to eliminate all components other than cellulose[50]. The first procedure (A) includes:

- a solution of toluene / ethanol (2: 1, v / v) in a Soxhlet apparatus for 6 hours
- vacuum pump to dry the solid residue
- ethanol for 2 h to remove residual toluene and vacuum drying

Soluble and insoluble fractions (mainly waxes and fatty acids) are removed through mixtures of polar and non-polar solvents. The delignification takes place using 2.5M NaOH in solid/solution ratio 1/8 (w/v) at 95 °C for 2 hours, while for the bleaching procedure, the sample was dispersed in water at 80 °C. Sodium chloride and acetic acid, in a molar ratio of 4/1, were added at intervals of 30 minutes (in a 5/1 ratio with the pulp). The treatment was repeated 6 times. The use of sodium bicarbonate, in a concentration of 1M at 80 °C for 3 hours, guarantees the removal of the hemicellulose from the pulp washed in water and dried in an oven at 40 °C. The solid residue was then separated by centrifugation, washed with distilled water, filtered, and dried again.

For the second procedure (B):

- Cynara waste was boiled in distilled water at 80 °C for 2 h and dried at 40 °C for 24 h. The process was repeated twice
- NaOH (5M) was used for the delignification, with solid/ solution ratio 1/8 (w/v), at 80 °C for 2 h).
- The pulp was washed in distilled water and dried for 24 h at 40 °C.
- Sodium carbonate was used to remove the hemicellulose and to bleaching process with dry pulp/Na_2CO_3 ratio of 1/10 (w/w).
- The product was heated at 80 °C for two hours until the solid became white.

The dispersion was centrifuged to remove the excess reagents and cellulose fibers were washed and dried.

Through both procedures A and B it is possible to obtain the pulp and then extract the nanocellulose using sulfuric acid at 40% w/v, at 45 °C for 30 min, following the method described in chapter 1, paragraph 2.2.
As regards procedure (A) the sol was called CNC-S and for procedure (B) CNC-NS.

2.6- Reaction of oxidation of cellulose sources

2.6.1- Preparation of TEMPO-oxidated nanocellulose

The selective oxidation of primary alcohol was performed using 2,2,6,6-Tetramethylpiperidine 1-oxyl (TEMPO). The CNC suspension (CNC-CL or CNC-H, described in chapter 1, paragraph 2.2) was treated with the TEMPO/NaBr/NaClO reaction system under various conditions. TEMPO was added to a CNC suspension, keeping the mmol ratio of TEMPO/g of cellulose constant. The amounts of NaBr and NaClO were varied, as reported in Table 1. After the established reaction time, the reaction was quenched by adding 1mL of ethanol. Finally, a 0.1 M HCl solution was used to neutralize the reaction mixture, which was then purified in dialysis tube until neutral pH. Table 1 reports the experimental conditions to obtain oxidized CNC. The sample is labelled as "TOCNC" followed by the number of the experiment.

Table 1- Experimental data for TEMPO mediated oxidation reaction of CNC

Sample	*CNC source*	*Cellulose (g)*	*TEMPO (mmol/g)*	*NaBr (mmol/g)*	*NaClO (mmol/g)*	*T (°C)*	*Reaction time*
TOCNC 2	CNC-CL	0,22	2	0,5	6	25	6h
TOCNC 5	CNC-H	0,11	2	0,5	6	60	6h
TOCNC 6	CNC-CL	0,22	2	0,5	12	25	6h
TOCNC 7	CNC-CL	0,22	2	0,5	3	25	6h
TOCNC 8	CNC-H	0,11	2	1	6	25	6h
TOCNC 9	CNC-H	0,11	2	5	6	25	6h
TOCNC 10	CNC-H	0,11	2	10	6	25	6h
TOCNC 11	CNC-CL	0,11	2	4	6	25	6h
TOCNC 12	CNC-CL	0,11	2	4	6	25	6h
TOCNC 13	CNC-CL	0,11	2	4	6	25	6h
TOCNC 14	CNC-H	0,11	2	10	6	25	2h
TOCNC 15	CNC-H	0,11	2	10	6	25	3h
TOCNC 16	CNC-H	0,11	2	4	6	25	6h
TOCNC 17	CNC-H	0,11	2	5	6	25	6h
TOCNC 18	CNC-H	0,11	2	4	5	25	6h
TOCNC 19	CNC-H	0,11	2	5	5	25	6h

2.6.2- Non-selective oxidation of cellulose sources

Non-selective oxidation reactions of cellulose involve hydrogen peroxide as oxidation reagent. Microfibrillated cellulose powder was used as cellulose source. The reaction was carried out following the protocol reported by Fan[51]: 50 mL of H_2O_2 (30% wt) and 2 mg of $FeSO_4 \cdot 4H_2O$ were added to 1 g of microfibrillated cellulose. The suspension was sonicated for 10 minutes and then stirred at 60 °C for 6 hours. The product (CNC-ox) was centrifugated until neutral pH.

2.7- Reaction of amidation

Functionalization with amino groups was performed following two methods: the EDC/NHS system and the APTES addition on CNC or oxidated CNC suspensions. In both reactions the focus was the introduction of the -NH_2 moiety onto the cellulose nanocrystals.

2.7.1- CNC functionalization with EDC/NHS system

According to Ruiz-Palomero[52], oxidized nanocellulose (TOCNC samples with 1.4 mmol/g of carboxylate groups), EDC HCl (1.2 mmol) and NHS (1.2 mmol) were suspended in MeOH in an inert atmosphere for 20 minutes. Separately a MeOH solution was prepared containing 18 mmol of ethylenediamine and 2.2 mmol of triethylamine. The mix of the two solutions was kept under constant stirring for 12 hours at room temperature. The product was then purified with dichloromethane and ethyl acetate to remove impurities. Then, distilled water was used to neutralize pH. The powder was dried in the oven at 40 °C. The final product in form of powder was labelled as CNC-NH.

2.7.2- CNC functionalization with (3-Aminopropyl) triethoxysilane (APTES)

A certain amount of microfibrillated cellulose or cellulose nanocrystals was dispersed in distilled water under stirring and sonication cycles in a flask of the appropriate volume until a colloidal suspension was obtained to which APTES was added [1 (g, nanocellulose): 5 (mL, APTES): 100 (mL, H_2O)][10]. Glacial acetic acid was added to the reaction mixture to reach pH 4; the reaction was brought to reflux for 4 hours under stirring. The reaction mixture was transferred

to a crystallizer and left to evaporate under a hood, to form a film, which was transferred to the muffle and brought to 100 °C for one hour. The reaction raw product was then redispersed in water and sonicated for 10 minutes to obtain a suspension which was purified with 10 centrifugation/washing cycles with distilled water. The final suspensions were named CNC-APTES and CMF-APTES, respectively.

2.8- CNC functionalization with polydimethylsiloxane (PDMS)

Stable CNC suspensions were mixed with hydrophobic polydimethylsiloxane (PDMS-OH): 20 mL of aqueous suspension of CNC (1% w/v) was mixed with 2 mL of PDMS. The reaction was stirred at room temperature until completely mixed. The final suspension was called CNC-PDMS.

2.9- CNC functionalization with silver nanoparticles

The biocidal activity was evaluated introducing metallic silver nanoparticles into cellulose nanocrystals suspension. Ag^0 nanoparticles were synthesized in aqueous solution starting from $AgNO_3$, PVA (1% w/v) and $NaBH_4$ following a procedure described in the literature[13,53]. Afterwards the solution was used in a 9/1 volumetric ratio to a known volume of CNC (1% w/v). The final concentration of silver nanoparticles in the CNC suspension was 100 ppm. The sol was called CNC/Ag.

3- Characterization

3.1- pH measurements

The pH of the CNC aqueous suspensions was measured with a Crison Basic 20 pH meter. The pH measurements were made in triplicate and the average of these values was considered.

3.2- Yield % and Concentration determination

The yield % of CNC suspensions were calculated following the formula (1):

$$Yield\ (\%) = \frac{m_f * V_i}{m_i * V_f} * 100 \qquad (1)$$

where m_i is the initial mass of cellulose, V_i is the volume of the total CNC suspension obtained, m_f is the mass of dry CNC and V_f is the volume of the suspension.

The determination of the concentration of the samples was carried out gravimetrically, by drying an aliquot of the samples in an oven at 40 °C. The following formula (2) was applied to calculate the concentration:

$$\mathrm{C} = \frac{m(g)}{V(mL)} * 100 \qquad (2)$$

where m represents the weight in grams of the sample after drying in an oven and V the volume of dried suspension expressed in mL.

3.3- Dynamic light scattering (DLS) and Electrophoretic light scattering (ELS)

Brookhaven 90Plus Nanoparticle Size Analyzer operating in the range of 0.6 nm–6 μm, by dynamic light scattering (DLS) was used to determine hydrodynamic diameter of the samples obtained. The zeta potential measurements established the surface charge of the nanocrystals by electrophoretic light scattering (ELS). The measurements were collected at 25°C (6 scans for each analysis). All sols were diluted in distilled water with a final concentration of about 0.20 mg/mL.

3.4- Raman spectroscopy

All powder samples were investigated with Raman spectroscopy. The spectra were recorded at 632.8 nm (He-Ne, 15 mW) with a Horiba - Jobin Yvon LabRam microspectrometer, equipped with 1800 lines/mm holographic grating and a Peltier cooled CCD detector (1024 × 256), using an ultralong working distance x50 microscope objective (Olympus MSPlan ULWD, numerical aperture 0.55). The silicon band at 520.6 cm^{-1} was used to calibrate the system. The laser power on the samples was less than 1 mW, obtained by means of density filters. Typical exposures were 10−60s, with 5–9 repetitions. The data analysis was performed by Labspec 5 (Horiba) software.

3.5- Fourier Transform Infrared Spectroscopy (FTIR)

The FTIR spectra, in ATR mode, of all samples were obtained using the Thermo-Nicolet Nexus spectrometer equipped with Thermo Smart Orbit ATR diamond accessory, in the range 4000–400 cm^{-1}, with a spectral resolution of 4 cm^{-1}. For the study of polimorph I and II, the curve fitting was carried out by LabSpec 5 software (Jobin Yvon Horiba, Kyoto, Japan), after background subtraction by a

2nd degree polynomial. The number of peaks involved were determined based on the second derivative of FTIR spectra in the range 3300–3700 cm^{-1} [54].

3.6- X-Ray Diffraction (XRD)

The X-ray diffraction characterization was performed with a Thermo ARL X'TRA X-ray diffractometer with Si-Li detector, using Cu-Kα radiation at 40 kV and 40 mA. The samples were scanned in a 2θ range of 5–60°. The crystallinity index (*CI%*) of the CNCs was calculated according to the method proposed by Segal[55] (3):

$$CI(\%) = \frac{I_{200} - I_{am}}{I_{200}} * 100 \qquad (3)$$

where I_{200} is the maximum peak intensity corresponding to the (200) reflection at 2θ ≈ 22° for cellulose II and ≈ 23° for cellulose Iβ, which represents the crystalline region, while I_{am}, which concerns the amorphous portion, is the minimum intensity value at 2θ ≈ 16 ÷ 18° between the peaks relative to the (110) and (200) reflections[56]. To gain further structural details of the cellulose nanofibers in terms of crystal size, polymorph identification, preferred orientation, and amorphous fraction, a Rietveld refinement was carried out on the overall X-ray diffraction pattern. To define the diffraction peaks shape, a pseudo-Voigt profile function was adopted where the gaussian contribution (G(θ)) is expressed by (4):

$$G(\theta) = GU\tan 2\theta + GV\tan\theta + GW + GP/\cos 2\theta \qquad (4)$$

GU, GV, and GW correspond to the Caglioti parameters describing the instrumental contribution of the variation in full-width at half maximum (FWHM) as a function of the diffraction angle (obtained by the fitting of the standard Al_2O_3). The GP term is used in the Scherrer equation (5):

$$CS \text{ (crystal size)} = K\lambda/\pi \sqrt{GP} \qquad (5)$$

where CS is the average diameter of the crystals, K is a form factor (taken 0.90 in spherical approximation), and λ is the wavelength of the incident beam. GP is the FWHM correlated to the integral width for each reflection and dependent from the CS.

Origin 8 software (OriginLab Corporation, Northampton, USA) was used for peak deconvolution.

3.7- Conductimetric titration

The degree of oxidation of TOCNC samples was determined by conductometric titration following the method reported by Habibi[57] using a Dosimat 665 Metrohm doser and a Crison microCM 2201 conductivity meter. In details, 50 µL of 1.2 M HCl was added before starting the titration. The samples were titrated with a standardized 0.00978 M NaOH solution on potassium hydrogen phthalate and the titration was checked using the automatic burette. After each addition, the conductivity value of the solution was measured. Some trials were carried out to find the number of points that would be most suitable to record to construct the titration curve. 15 mL of titrant has been used and measure at 1 mL intervals between 0 - 4 mL, at 0.3 mL intervals between 4 - 8 mL, and at 1 mL intervals between 8 - 15 mL. Once the data for each sample was collected, the data was then processed by finding the equivalence volume corresponding to the strong acid titration and the equivalence volume corresponding to the weak acid titration. The difference between these two volumes of equivalence corresponds, as number of equivalents, to the quantity of weak acid present in the solution, associated with the quantity of oxidized nanocrystals. The first part of the curve (figure 1) corresponds to the titration of the strong acid, added in a known quantity to each sample: the measured conductivity decreases linearly with the volume of NaOH added, due to the consumption of free protons that contribute

to the conductivity of the solution. When the buffer system is reached, the curve shows a plateau ; carboxylated cellulose nanocrystals behaves like a weak acid

$$CNC\text{-}COOH \rightleftarrows CNC\text{-}COO^- + H^+$$

Finally, after the addition on NaOH excess, the conductivity increases following the addition of OH- ions to the solution. From the titration curve, to find the equivalent volume each time, it is necessary to find the length of the plateau, obtainable from the difference between the volume of titrant in which the buffer system ends and the volume in which it begins. The starting volume of the buffer system corresponds to the intersection between the line that best interpolates the points corresponding to the strong acid line (orange line in figure 1) and the line that best interpolates the points of the buffer section (black line in figure 1). Similarly, the end volume of the buffer system is given by the intersection between the line that best interpolates the points corresponding to the flat section of the curve and the line that interpolates the excess base (blue line in figure 1).

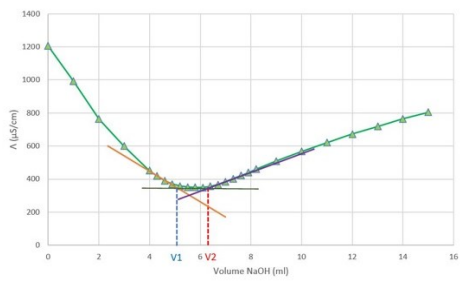

Figure 1- Illustration of the method used to calculate the equivalent volume

After obtaining the two equivalence volumes V_1 and V_2, formula (6) was used to calculate the degree of oxidation (*DO %*) of the individual samples[57]

$$DO\ (\%) = \frac{162\ x\ C\ x\ (V_2 - V_1)}{w - 36\ x\ C\ x\ (V_2 - V_1)}\ x\ 100 \qquad (6)$$

where C is the concentration of NaOH (mol / l), V_1 and V_2 are the volumes of NaOH (L), and w (g) is the mass of the sample dried; the value 36 corresponds to the difference between the molecular weight of an AGU and that of a unit of sodium salt, while 162 is the molecular mass of an AGU[57]. The error associated with the degree of oxidation was also calculated, spreading the uncertainty over the volumes on the above parameter. The uncertainty on the volume corresponds to 1/1000 of the flow rate of the burette, which in this case corresponds to 50 ml.

3.8- Thermogravimetric analysis (TGA)

Thermogravimetric analysis was carried out to assess the thermal stability of the samples. TGA analyses were carried out by means of a Perkin Elmer TGA8000 instrument (mass sample: 1–3 mg) at a heating rate of 10 °C min^{-1} in the temperature range 30–550 °C. The measurements were performed at an atmospheric pressure under air atmosphere. The DTG curves were calculated by second derivate on TGA curves using LabSpec 5 software (Jobin Yvon Horiba, Kyoto, Japan).

3.9- Transmission Electron Microscope (TEM)

The JEOL 2200FS field emission microscope operating at 200 kV accelerating voltage, equipped with two High Angle Annular Dark Field detectors (HAADF) and the Energy Dispersive X-ray Spectrometer (EDX) was used to investigate the shape and size of the cellulose particles in the samples. All the investigations were performed in the HAADF Scanning TEM (STEM) mode to detect the Z contrast in the images and to obtain compositional maps of the samples by EDX. The samples for the observations were prepared by dropping a diluted sample (0.01, w/w% in water) onto 300-mesh holey carbon copper grids.

3.10- Solid-State NMR (SSNMR)

SSNMR measurements were carried out on a Bruker Avance Neo spectrometer working at Larmor frequencies of 500.13 and 125.77 MHz for ^{1}H and ^{13}C nuclei, respectively. Depending on the sample amount, either a double-resonance CP/MAS (cross polarization/magic angle spinning) probe-head, accommodating rotors with external diameter of 4 mm, or a triple-resonance H/X/Y CP/MAS probe-head, accommodating rotors with external diameter of 2.5 mm, was used. The ^{13}C experiments were performed at different MAS frequencies (from 5 to 15 kHz) using a ^{1}H-^{13}C CP pulse sequence with a contact time of 1 ms, chosen based on variable contact time experiments and literature data[58], and a recycle delay of 5-7 s. From 400 to 40000 scans were accumulated, depending on the sample and on the probe-head. The ^{13}C chemical shift was referenced to the signal of adamantane at 38.46 ppm, used as external standard. All experiments were performed at room temperature using dry air as spinning gas.

3.11- Biocidal activity

The bacteria *Escherichia coli* (Gram negative) and *Bacillus subtilis* (Gram positive) were used to test the antimicrobial activity of CNC functionalized with silver (CNCs/Ag). The minimum inhibitory concentration (MIC) values were determined by the broth dilution method. Each test condition was replicated four times. The growth of the *E. coli* and *B. subtilis* in TSB medium (Thermo Scientific™ Tryptone Soy Broth) was evaluated as control. The bacteria (100 µl) were inoculated into 96 wells of a microtitration plate in which were inoculated 100 µl of CNC-CL, CNC-WP, CNC-CL/Ag, CNC-WP/Ag and silver nanoparticles suspensions (decreasing concentration up 100ppm to 6.25 ppm) to test their sensitivity. The tests were incubated for 20 h at 37 °C. Then, the absorbance at 600 nm (Abs_{600}) was measured. At the same wavelength the

absorbance relating only to the suspensions tested with the bacteria were recorded to subtract this value at the medium.

3.12- Elemental analysis

To quantify the presence of the elements in the samples, elemental analyses were performed on a Thermo Fischer Scientific FlashSmart CHNS analyzer. The sols were dried and the powders obtained were analyzed.

4- Results and discussion

4.1- pH measurements

For all sols obtained after hydrolysis pH values were measured and their values are reported in table 2. Generally, the use of different acid gives the acidity (pH~3), while the amino groups or NaOH (pH~10) confer the alkalinity. The dialysis process allows to eliminate the excess reagents but also to have pH values around neutrality.

Table 2- pH values on CNC. Standard deviation in parentheses.

Sample	pH
CNC-CL	5.8 (3)
CNC-H	6.7 (2)
CNC-WP	6.1 (2)
CNC-S	6.2 (1)
CNC-NS	6.0 (3)
TOCNC6	6.4 (4)
CNC-ox	5.1 (5)
CNC-APTES	7.6 (3)
CNC-NH	7.7 (3)
CNC-PDMS	7.5 (3)
CNC-Ag	6.2 (2)

4.2- Yield % and concentration determination

Following the formulas (1) and (2) reported in chapter 1, paragraph 3.2, the yield and the concentration for each CNC were calculated. The values obtained are summarized in table 3. The better yield (88%) is obtained for the extraction from cotton linter by H_2SO_4 (64%), probably due to the efficiency of the acid type and the pure substrate used. When a non-pure material is used as starting material, such as wastepaper or agricultural waste, the use of an acid with a lower concentration (40%) is necessary because high concentrations are very aggressive, causing the complete carbonization of the product. On the other hand, the use of a reduced acid concentration causes a lower yield as shown in table 3. For sample CNC-H low yield is observed, probably due to a minor efficiency of the hydrochloric acid with respect to the sulfuric acid.
The concentration is around 1% (w/v) for all CNC samples.

Table 3- Yield and concentration (expressed in percentage) of the product obtained

Sample	Yield (%)	Concentration (%)
CNC-CL	88	1.15
CNC-H	68	0.5
CNC-WP	65	0.98
CNC-S	63	0.95
CNC-NS	67	0.96

4.3- Dynamic light scattering (DLS) and Electrophoretic light scattering (ELS)

Dynamic Light Scattering was used to investigate the CNC hydrodynamic diameter (Table 4). The suspensions have almost uniform size distribution, and their stabilities have been evaluated by ELS measurements. Generally, values of zeta potential outside -30 mV / +30 mV range, indicate good sol stability as reported by Bhattacharjee[59]. The negative ζ Potential indicates formation of stable suspensions in all CNC[59,60], except for CNC-H. During the acid hydrolysis with sulfuric acid the esterification of hydroxyl groups leads to the presence of sulfate groups with negative charge on the surface of the crystals. The negatively charges contribute to the stabilization of the suspensions thanks to electrostatic repulsion[61]. It can be noted that in the case of CNC extracted by waste materials such as samples CNC-S, CNC-NS and CNC-MF, there are lower ζ Potential values than those obtained by CNC from cotton linter. This can be explained by the different concentration of sulfuric acid used during the hydrolysis phase, which therefore brings a smaller number of negative surface charges. The values of the diameter of the nanocrystals are referred to the hydrodynamic radius, considering the sphere of hydration. The high value of hydrodynamic diameter for CNC-NS is probably due to the tangled network. The ζ potential of CNC-S is therefore comparable to that of the CNC-MF. It is also observed that the cellulose suspensions obtained by hydrolysis with hydrochloric acid have a very low zeta potential as expected from a practically absent surface charge: this is the case of sample CNC-H. In the case of oxidated nanocellulose suspensions (TOCNC samples) the contribution of the carbonyl group produces a good electrostatic repulsion between the nanocrystals included in the stability range for colloidal suspensions. For the sol of nanocellulose functionalized with APTES, a lower stability is observed with a tendency to precipitate a few days

after preparation. This can be explained considering the high value of the mean hydrodynamic diameter of the particles. All suspensions containing CMF powder were not analyzed because stable dispersions in water were not obtained due to their large particle size.

Table 4- DLS and ζ potential on CNC

Sample	Hydrodynamic diameter (nm)	ζ Potential (mV)
CNC-CL	187 ± 20	-63 ± 3
CNC-H	970 ± 68	-1 ± 1
CNC-WP	243 ± 25	-33 ± 2
CNC-S	230 ± 22	-33 ± 4
CNC-NS	469 ± 17	-45 ± 3
CNC-MF	229 ± 32	-32 ± 1
CNC-APTES	633 ± 24	-33 ± 1
CNC-ox	762 ± 80	- 48 ± 2
TOCNC 2	179 ± 4	- 46 ± 1
TOCNC 6	179 ± 38	-52 ± 1
TOCNC 7	220 ± 36	-27 ± 2
TOCNC 8	309 ± 18	-63 ± 3
TOCNC 13	285 ± 32	-59 ± 5
TOCNC 16	219 ± 24	-49 ± 4
TOCNC 19	195 ± 12	-53 ± 2

4.4- Raman spectroscopy

Raman spectroscopy is useful for functional groups identification as well as for identification of crystallinity of the samples. In particular in figure 2 the Raman spectra of samples CNC-CL and CNC-WP are reported and compared with sample of pure cellulose. The spectra were normalized to the main peak of cellulose at 1097 cm^{-1}. The peak at 1097 cm^{-1}, assigned to stretching vibration of C-O bond, is related to the cellulose crystallinity[62]. In the region 1500-1300 cm^{-1} the vibrational bands of CH and CH_2 deformation modes with C-O stretching modes[63]: at 1478 cm^{-1} and 1410 cm^{-1} the bending modes of CH_2, are found, with contribution from ν(H_2C-OH), at 1378 cm^{-1} the CH bending and at 1337 cm^{-1} the CH_2 twisting and C6-OH bending. The peaks at 1122 and 1157 cm^{-1} are assigned

to a combination of vasC-O-C with H-C-O out of plane deformation. The peaks at lower wavenumbers are due to the lattice modes of the pyranosic ring.

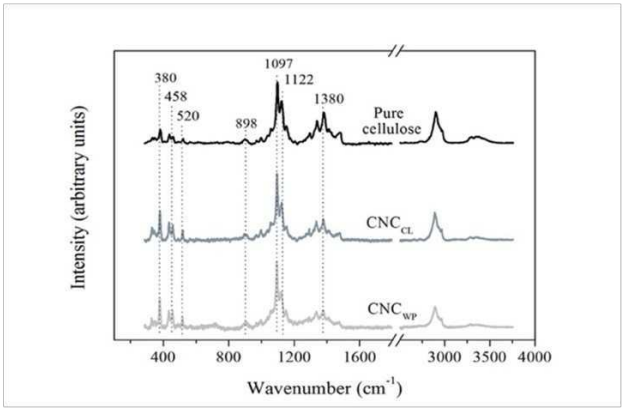

Figure 2- Raman spectra of pure cellulose, CNC-CL and CNC-WP

4.5- Fourier Transform Infrared Spectroscopy (FTIR)

The FTIR spectroscopy allows identifying the functional groups of CNC and monitoring the goodness of reactions. FTIR can be also used to define the empiric crystallinity index. The FTIR spectra of dried samples of CNC-CL and CNC-WP are reported in comparison with pure cellulose in figure 3. The OH stretching vibrations (3341 and 3332 cm^{-1}) in both CNC are shifted to lower wavenumbers respect to pure cellulose sample (3370 cm^{-1}) because the intramolecular hydrogen bonds in the crystalline domine are stronger[64]. The band at 1430 cm^{-1} attributed to CH_2 bending vibration, is described as "crystalline absorption band"[65]. The ratio between this intensity and the vibration at 897 cm^{-1} (assigned to C-O-C β-glycosidic linkages) defines the "empiric crystallinity index" of nanocellulose. Many authors[66–68] report that an increase in intensity of the bands at 372 cm^{-1}, 1312 cm^{-1}, 1159 cm^{-1}, 1105 cm^{-1} and at 981 cm^{-1} corresponds to an increase in the crystallinity of the nanocellulose.

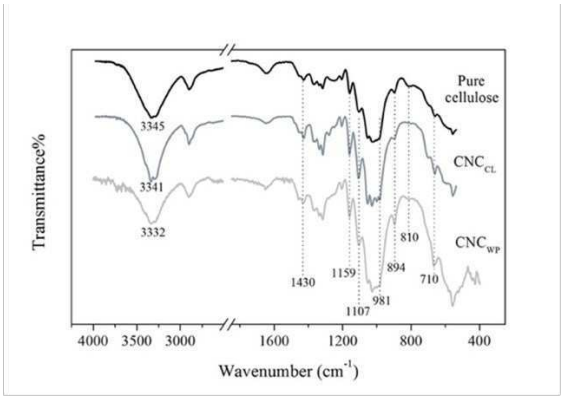

Figure 3- FTIR spectra of pure cellulose, CNC-CL and CNC-WP

Regarding the samples obtained from artichoke waste, following two different experimental methodologies of extraction as reported in the experimental part, FTIR technique allows to characterize the CNC obtained and to discriminate the type of polymorph. In figure 4, the CNC-CL, CNC-S, CNC-NS and CNC-MF spectra were normalized with respect to CH stretching vibrations (2750-2980 cm^{-1} range). For the CNC-S and CNC-NS spectra, the features of lignin components[69], νC-O of acetyl and ester groups at 1730 cm^{-1}, νC=C of aromatic ring at about 1600-1510 cm^{-1} and νC-O of aryl groups at 1240 cm^{-1} are absent[70]. As known from the literature, the alkali treatment leads to the formation of polymorph II. This conversion can be monitored by FTIR. The differences between polymorph Iβ and II are evident in the νOH vibration region. In fact, two new signals appear at 3494 cm^{-1} and 3441 cm^{-1} assigned to νO-H engaged in H-bonds for polymorph II in samples CNC-S, CNC-NS and CNC-MF. Moreover, the band at 1419 cm^{-1} due to δCH_2 and the band at 892 cm^{-1} assigned to νC-O-C of the β-glycosidic linkage[71], found in the spectrum of CNC-CL sample (polymorph Iβ), are shifted at 1430 cm^{-1} and 895 cm^{-1}, respectively[72], in the spectra of CNC-S, CNC-NS and CNC-MF. Finally, the differences between the two polymorphs are evident in the 1500-600 cm^{-1} region, due to the different

intermolecular and intramolecular bonds. Table 5 shows the FTIR bands and their assignment[72,73].

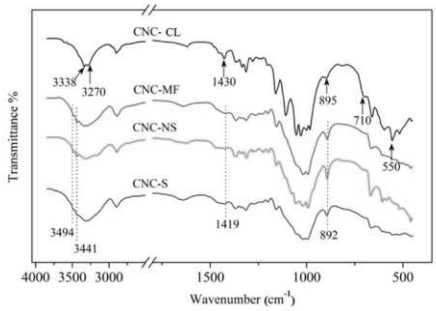

Figure 4- FTIR spectra of CNC extracted from cotton linter (CNC-CL and CNC-MF) and from Cynara scolymus L. (CNC-NS and CNC-S)

Table 5- The assignment of the main FTIR bands of CNC Iβ (CNC-CL) and CNC II (CNC-MF, CNC-S, CNC-NS) according to references, the band shift and absorbance intensity variation from cellulose Iβ and cellulose II. Reproduced with permission from Ref.[50]

Wavenumber (cm^{-1})		$\Delta\nu$ (cm^{-1}) / Absorbance change	Assignment
CNC Iβ	CNC II		
3338	3494	+156/-	νO3H---O5 intramolecular H bonds
3270	3441	+171/-	νO2H---O6 intramolecular H bonds
2900	2887	-13/-	νCH
1482	1470	-12/Δ	δCH_2
1430	1419	-10/ ∇	δCH (C1)
1366	1373	+7/ ∇	δC–H
1336	1336	- /∇	δCOH in plane (C2 or C3)
1236	1226	-10/ Δ	δCOH in plane (C6)
1203	1195	-8/-	δCOH in plane
1160	1153	-7/ ∇	ν_{as}COC (β - glycosidic bond)
1030	1014	-16/ ∇	νC-OH of C6
984	994	+10/Δ	C-O valence vibration of C6
895	892	-3/Δ	COC of the ν-glycosidic bond and/or ether group
660	665	-5/-	δCOH out of plane
550			τOH of C6

Key to symbols: ν: stretching, δ: bending, τ: torsion, Δ: increase, ∇: decrease, -: equal

The FTIR investigation allows also to study the empirical relationship on the ratio of the absorption bands at 3336 cm^{-1} and 1336 cm^{-1}, known as Hydrogen Bond Intensity (HBI), to obtain information on the degree of inter- and intramolecular H-bonding[74]. According to literature there is an inverse relationship between CI and HBI[72,75]. The CNC-CL is characterized by higher CI% and a lower HBI (1.47 ± 3) compared to the mercerized sols (CNC-MF = 2.39 ± 2, CNC-S =1.98 ± 2, CNC-NS = 2.18 ± 4). The use of alkali solution causes the breaking of the intramolecular hydrogen bond that stabilizes the β-glycosidic linkage in crystalline cellulose[72]. The irreversible conversion of the polymorph causes the modification of voids and pores in the fibers and crystal structure. Figure 5 shows the hydrogen bond networks in cellulose Iβ (fig.5a) and II (fig. 5b). The glucopyranose unit has three hydroxyl groups that can be involved in inter and intramolecular hydrogen bonds with adjacent molecules or of the same chain. The intermolecular hydrogen bonds are almost orthogonal to the axis of the cellulose chains, while the intramolecular ones are almost parallel.

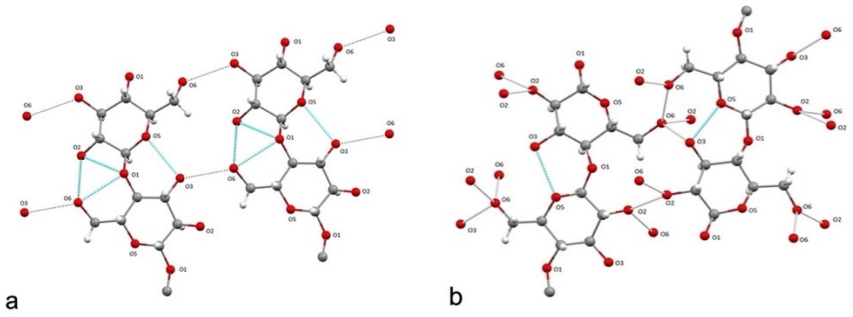

Figure 5- Patterns of inter- and intramolecular bond in cellulose Iβ (a) and II (b). The cyan and light green dotted lines indicate intra- and inter- molecular hydrogen bonds, respectively. Reproduced with permission from Ref.[50]

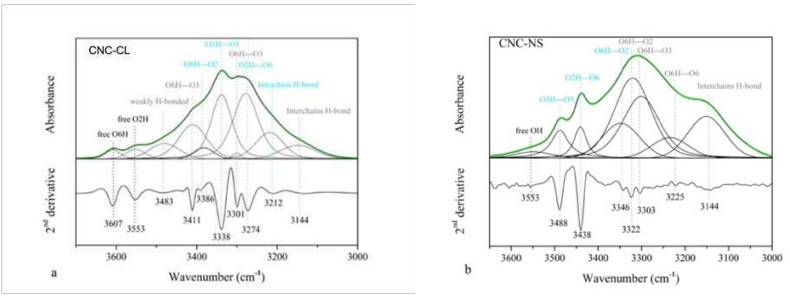

Figure 6- Deconvolution of the FTIR spectra and second derivative of (a) CNC-CL (polymorph Iβ) and (b) CNC-NS (polymorph II) in the 3700-3000 cm^{-1} region. The cyano and light gray colours refer to intra- and intermolecular H-bonds, respectively. Reproduced with permission from Ref.[50]

Figure 6 shows the convolution of multiple sub-bands in the vibration region of the OH stretching. In figure 6a the intermolecular hydrogen bonds (light gray color) involve primary alcohols as proton donors while the intramolecular hydrogen bonds (cyan color) are preferably maintained by secondary alcohols. In figure 6b the OH groups are involved in a complex 3D network of H bonds between the antiparallel and staggered chains[50,76,77].

FTIR spectroscopy allows to monitor the CNC functionalization reactions, thanks to characteristic signals due to new covalent bonds on the surface of the nanocrystals. For the TEMPO-mediated oxidation of CNC, all samples obtained (TOCNC) were investigated with the FTIR spectroscopy. As shows in figure 7, the characteristic vibrational stretching of carbonyl groups appears at 1604 cm^{-1} [78,79] (indicated in figure 7 with a dotted line). No further changes, such as decrease in the crystallinity, depolymerization or variation of polymorph (from Iβ to II) are observed. The FTIR investigation is not quantitative but allows to discriminate the presence of carboxyl or carbonyl groups (1730 and 1600 cm^{-1} respectively as reported in literature[78,79]). The TEMPO-mediated oxidation of cellulose is a selective reaction to the primary OH group and does not involve the other secondary hydroxyl groups, leaving the inter and intramolecular interactions of cellulose polymorph I almost unaltered.

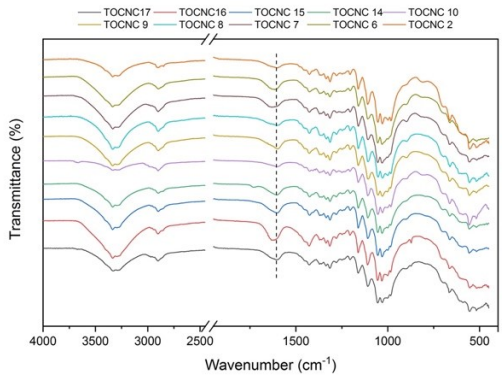

Figure 7- FTIR spectra acquired on TOCNC samples

The FTIR spectra of the products obtained by functionalization with amino groups are reported in figures 8a and 8b. The typical signals of cellulose are evident in all spectra: the band at 3300 cm^{-1} is assigned to OH stretching, at 2900 cm^{-1} is present the CH stretching, ν_{as} COC at 1100 cm^{-1}, the ν C-OH at 1030 cm^{-1} and the COC of the ν-glycosidic bond at 895 cm^{-1}. In addition, it is possible to observe the presence of a peak at 1560 cm^{-1} attributable to the N-H bending of the primary amine present in the organic pendant grafting onto the surface of functionalized nanocellulose samples.

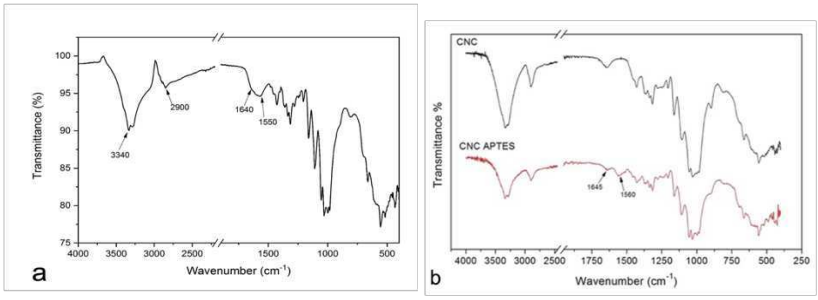

Figure 8- a) FTIR spectrum acquired on CNC-NH sample; b) FTIR spectra comparing CNC-CL and CNC-APTES samples.

To evaluate the goodness of the hydrophobic functionalization, the FTIR investigation was used to highlight the presence of the siloxane group. Figure 9 reports the comparison between spectra of CNC functionalized with PDMS (spectrum in red) and that of pure PDMS (spectrum with black line). The typical signals of the polymer[80] are evident and the attribution of the signals are reported in table 6.

Table 6- FT-IR absorption bands and their assignments to PDMS functional groups

Wavenumber (cm^{-1})	**Assignment**
2962	ν_{as} CH_3
2904	ν CH_3
1258	δ CH_3
862	ρ CH_3
1089	ν_{as} Si-O-Si
1022	ν Si-O-Si
761	ν Si-C

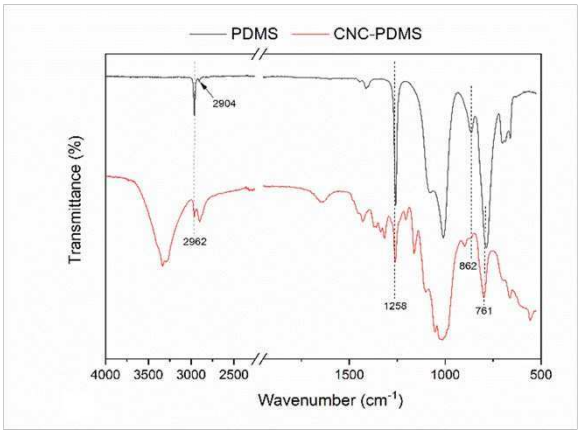

Figure 9- FTIR spectra on CNC-PDMS (red line) and pure PDMS (black line)

4.6- X-Ray Powder Diffraction (XRPD)

The XRPD technique was primarily used to identify the crystalline phases and to evaluate the crystallinity index of the obtained materials following the method of Seagal (see formula (3) in chapter 1, paragraph 3.6). As reported in the literature[65,81] both polymorphs (Iβ and II) crystallize in the same monoclinic symmetry ($P2_1$ space group) but they are characterized by a different spatial distribution of the polymeric cellulose chains, aligned along the c axis but with a different packing mediated by intermolecular hydrogen-bonds (figure 10). The two crystal structures and corresponding atomic positions were obtained from earlier literature[81,82].

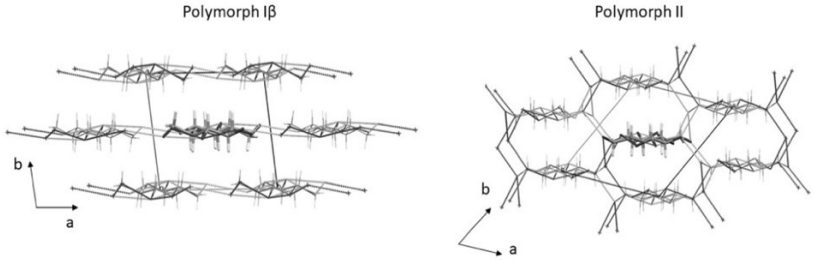

Figure 10- Crystal packing of polymorphs Ib and II of cellulose. Reproduced with permission from Ref.[50]

For polymorph Iβ, the planar sheets of polysaccharide chains are stacked along the *b* axis, whereas polymorph II is constituted of a honeycomb-like distribution of the chains. The detailed structure may be found in literature[81,83].

Samples CNC-CL and CNC-MF have been selected as standard for polymorph Iβ and polymorph II, respectively. Figure 11a shows the Rietveld refinement[81] based on the crystal structure for the Iβ phase and featured by the three intense peaks at 2θ = 22.7° (200 crystallographic plane), peaks at 2θ = 14.7° (1–10 crystal planes), 2θ = 16.4° (110 crystal planes), 2θ = 20.5° (012 + 102) and peak at 2θ = 34.4° (004). As reported by French[84] the intensity of 200 crystallographic plane

is related to the fraction of crystalline cellulose, while the region 2θ ~ 18° between the (200) and (110), have a minimum of intensity and it is associate to the amorphous fraction of the Iβ [85].

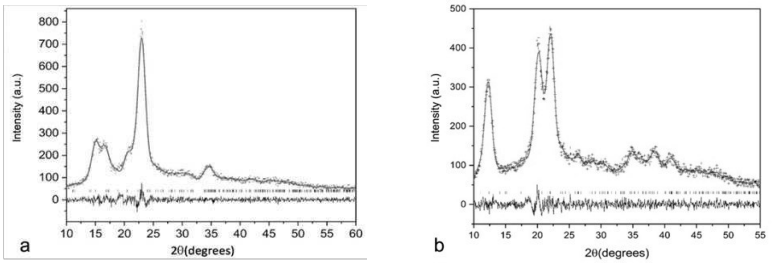

Figure 11- Rietveld analysis for a) polymorph Iβ (acquired on sample CNC-CL) and b) polymorph II (acquired on CNC-MF). The ticks mark the reflections of the monoclinic crystal structure and the black line indicates the calculated fitting.

The Rietveld refinement converges to a value of GP indicating a crystal size of approximately 16 nm. With March-Dollase correction for preferred orientation, an evident improvement of the structural refinement yields final agreement factors Rp=3.5%, Rwp=4.8%. Such effect is expected, considering that the cellulose fiber grows along the *c* axis and the reflections showing appreciable intensity belong to the hk0 class. This profile has been observed for samples of CNC-CL and CNC-WP.

The Rietveld refinement for the polymorph II standard (CNC-MF sample) was performed following the same procedure. It is reported in figure 11b. The crystal size approaches 10 nm indicating a slight decrease of the crystallites dimension if compared to the Iβ counterpart. These profiles have been observed for samples CNC-MF, CNC-S and CNC-NS as indicated in figure 12.

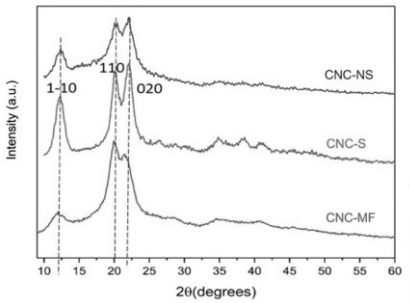

*Figure 12- X-ray diffraction spectra of the mercerized CNC samples (CNC-NS, CNC-S and CNC-MF). Reproduced with permission from Ref.*4,5

Figure 13 shows the diffraction pattern of selected oxidated samples (TOCNC6 and TOCNC18), evidencing the typical profile of polymorph Iβ.

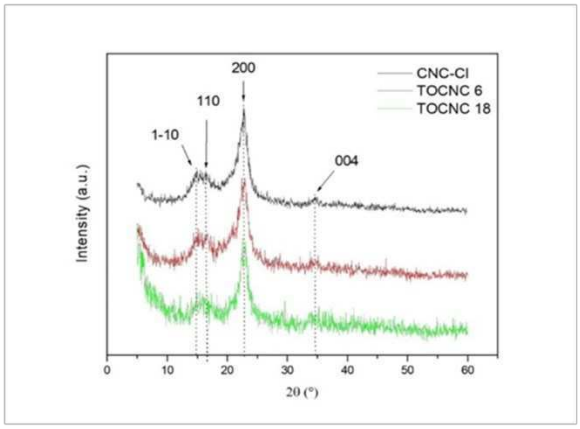

Figure 13- XRD comparison of CNC-CL and TOCNC 6 and TOCNC 18

In figure 14 the pattern of the sample obtained with non-selective oxidation (chapter1, paragraph 2.6.2) is shown. It suggests a profile comparable with that of polymorph I but the extended amourphous region prevented us to do further analyses.

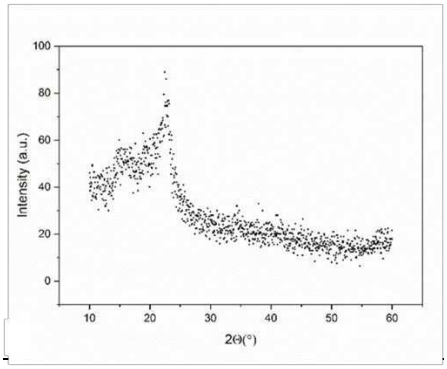

Figure 14- XRPD on oxidate CNC

Following formula (3) it is possible to calculate the crystallinity index (CI%) of all samples analyzed. Table 7 reports the CI% of several samples of CNC and oxidated CNC, obtained following the procedures described in the experimental part. The CI% for CNC-S and CNC-NS is 75% and 63% respectively. The crystallinity index value of CNC-NS is similar to that found for sample CNC-MF. The CI% obtained for CNC-CL (89%) is higher because of the use of a pure cotton raw cellulose material and a fewer number of extraction steps.

Table 7- Crystallinity index (CI%) of CNCs calculated with the Segal method

Sample	***CI%***	**Samples TOCNC**	***CI%***
CNC-NS	63	TOCNC 2	74
CNC-MF	67	TOCNC 6	72
CNC-S	75	TOCNC 7	73
CNC-CL	89	TOCNC 8	76
CNC-WP	80	TOCNC 9	75
CNC-ox	40	TOCNC 15	77
		TOCNC 16	80
		TOCNC 17	79
		TOCNC 18	78
		TOCNC 19	79

For all oxidated samples reported in table 7, a high CI% is observed. For samples TOCNC2-9 probably the use of too much NaCl or too little NaBr affects the crystallinity by creating secondary reaction products or by depolymerizing the CNC. An excellent compromise has been found for the TOCNC15-19 samples. In these oxidized CNCs samples the crystallinity index is slightly lower than that obtained from CNCs extracted from cotton and comparable with CNC-WP. This confirms that the TEMPO-mediated oxidation of cellulose does not affect the overall crystallinity of the starting material.

4.7- Conductimetric titration

To evaluate the Degree Oxidation (*DO%*) and the goodness of oxidation reaction the conductimetric titration was performed. In table 8 the degree oxidation (*DO%*) results obtained following the formula (6) are reported. According to Habibi[57] the data are in the range 3-12% based on the dosage of NaClO used and on the other parameters which characterized the synthesis of each sample. In sample TOCNC7 3mmol/g of NaClO was used: in this experiment the oxidation was unsuccessful. A large increase in the degree of oxidation was observed when NaClO dosage varied from 6 to 12 mmol (sample TOCNC 2 and sample TOCNC6, respectively). Therefore, taking into consideration only the *DO %*, an exponential increase in the efficiency of the reaction is observed by increasing the quantity of NaClO. Samples TOCNC 8, 9 and 15, on the other hand, differ only in the amount of NaBr. An increase in the degree of oxidation can be observed between samples treated with 1 and 5 mmol/g, almost double. However, no significant difference was observed by increasing the dose to 10 mmol/g. Having certified the importance of the dosage of this compound on the efficiency of the reaction, further tests were carried out, aimed at determining how much

co-catalyst was necessary to obtain an appreciable reaction speed but at the same time minimizing the use of both the latter and of primary oxidant, thus aiming for a good compromise between reaction times and yield.

*Table 8- Degree oxidation of all samples. *nd= not determinable due to low degree of oxidation*

Samples TOCNC	DO (%)
TOCNC 2	3.1 (15)
TOCNC 5	4.1 (3)
TOCNC 6	12.0 (4)
TOCNC 7	*nd
TOCNC 8	5.4 (2)
TOCNC 9	9.4 (4)
TOCNC 10	7.1 (3)
TOCNC 11	6.2 (4)
TOCNC 12	5.3 (4)
TOCNC 13	6.3 (3)
TOCNC 14	2.01 (11)
TOCNC 15	9.8 (4)
TOCNC 16	9.1 (4)
TOCNC 17	10.3 (5)
TOCNC 18	7.3 (3)
TOCNC 19	9.9 (5)

Two pairs of samples, TOCNC 16-17 and TOCNC 18-19, were oxidized using respectively 6 mmol of NaClO for the first pair and 5 mmol of NaClO for the second pair. In both cases, the oxidized samples with a greater amount of cocatalyst result more oxidized. Comparing samples TOCNC 16 and 19, it can be observed that in the second case it was possible to obtain an oxidation degree that was not significantly different from the first despite using a smaller quantity of oxidant, thanks to the increase in the cocatalyst dosage.

Samples TOCNC 11, 12 and 13 were instead designed to verify the effects of the basicity of the reaction environment: before adding the primary oxidant, the moles of NaOH were added in ratios of 0 mmol:1g (TOCNC 11), 6 mmol:1g (TOCNC 12) and 12 mmol:1g (TOCNC 13) respect to the CNC. It can be observed that a high pH value achieved through addition of strong base seems not to favor the reaction significantly, a sign that the primary oxidant, once added, makes the already basic pH sufficient to trigger the reaction. Finally, some syntheses were performed to determine the time required for the reaction to complete. To obtain a very high degree of oxidation, 3 hours may be sufficient, as demonstrated by the degree of oxidation of samples TOCNC 15, while TOCNC 14 (2 h of reaction) has a very low *DO%*.

4.8- Thermogravimetric analysis (TGA)

Thermogravimetric analysis has been performed on CNC and on oxidized CNC samples. Figure 15a shows the thermogravimetric curves (TG) and figure 15b the corresponding derived curves (DTG) on CNC obtained from cotton linter (CNC-CL), through Soxhlet (CNC-S) and no-Soxhlet (CNC-NS) extraction methods and by mercerization process (CNC-MF) as described in the experimental part. The initial weight loss (less than 10%) at 60 °C and 150 °C can be attributed to the loss of humidity absorbed by the surface, including chemisorbed water and/or hydrogen-bound water[86]. At temperatures above 150 °C, CNC-CL have two pyrolysis processes, observed in the DTG curve between 180-300 °C (40% weight loss) attributed to the presence of sulfate groups, on the crystals that leads to a decrease in the activation energy due to CNC degradation, making the sample more sensitive to thermal degradation, and 300-500 °C (20% weight loss) the degradation of the cellulosic network[87,88]. Furthermore, the small dimensions of the CNC-CL crystals give a high surface area which could play an important role

in decreasing their thermal stability[87]. For all polymorph II samples (CNC-S, CNC-NS, CNC-MF) the degradation process, with a weight loss of around 60%, is recorded at higher temperatures (270-400 °C), probably due to the more tangled network with greater interaction of the groups -OH, which require more energy to initiate the degradation process. During the mercerization process the hydroxide ions penetrate widely inside the crystals producing a swelling of the CNC and after their removal during dialysis, the cellulose chains recrystallize into cellulose II. The removal of hemicellulose and lignin improves the thermal stability. The latest weight loss above 500 °C is due to the carbon residues depolymerization[89,90].

With the TEMPO-mediated oxidation, some sulfate groups are replaced by carbonyl groups. As reported in figure 15 c-d, the thermogram of TOCNC 6 sample shows better thermal stability than its starting substrate (CNC-CL). Moreover, the presence of carboxyl groups allows to reach higher temperatures thanks to the better cross-linking properties of these groups[91]. On the contrary, when the oxidation is carried out on neutral CNC (CNC-H), without surface sulphate groups, a decrease of thermal stability of the oxidated product (TOCNC 18) can be observed. The absence of negative sulfate groups ensures the best thermal stability: the differences between two substrates are evident in figure 15 e-f in which the CNC-CL has a very low thermal stability respect to CNC-H. As reported in literature[92] there is a correlation between thermal stability and the surface charge of the sample. Furthermore, sulfuric acid catalyzes the depolymerization reactions on the nanocrystals. In details, as can be seen in figure 15 d and 15 h, for all the samples a weight loss is observed (equal to 4.2% for TOCNC 6 and approximately 7.5% for TOCNC 18) below 100 °C, which is attributed to the evaporation of the surface moisture of the sample.

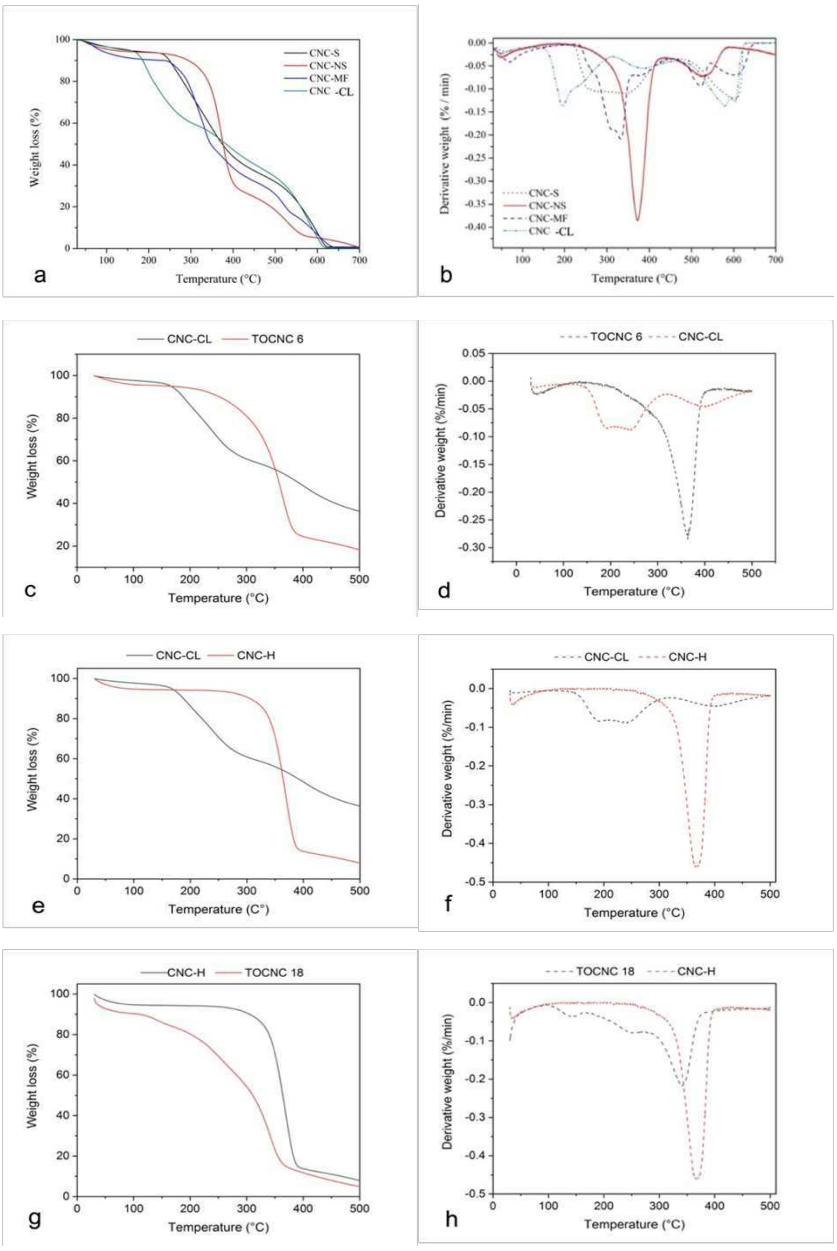

Figure 15- TGA on a) CNC polymorphs I and II, c) CNC-CL and TOCNC6, e) CNC-CL and CNC-H, g) CNC-H and TOCNC 18; DTG on b) CNC polymorphs I and II, d) CNC-CL and TOCNC6, f) CNC-CL and CNC-H, h) CNC-H and TOCNC 18. Fig. a -b reproduced with permission from Ref. [50]

The thermogram of TOCNC 6 sample (figure 15d), shows the loss of about 77% of the initial mass in a single step. On the other hand, the thermogram of TOCNC 18 sample shows a multistep degradation process. A first decomposition is observed with a weight loss of 6.5%, which is attributable to the release of the water bound internally to the cellulose chains. A second decomposition is observed, with a weight loss equal to 24% around 250 °C attributable to the decarboxylation of the material[93]. Finally, as the temperature rises further, the process ends with a third degradation step around 330 °C.

4.9- Transmission Electron Microscope (TEM)

The morphological aspect of cellulose nanocrystals has been evaluated by TEM analysis. A typical STEM HAADF image of particles in CNC-CL and CNC-WP samples are reported in figures 16a and 16b. The nanocrystals appear in rod-like whiskers form[94], with a length of about 200 nm and a width of about 20 nm, well separated for the CNC-CL and more tangled in the case of the CNC-WP. The average aspect ratio (length over width) of the fibers can be estimated in the range of 10–15.

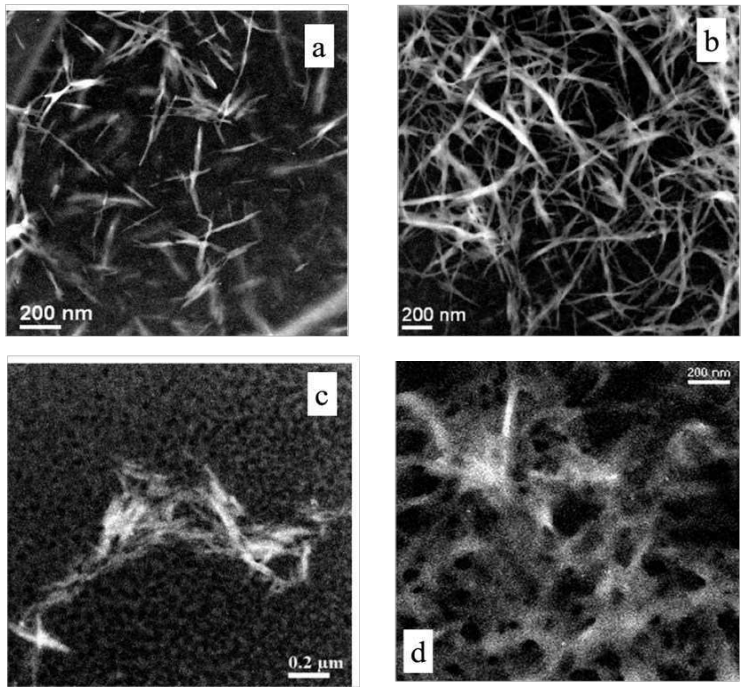

Figure 16- STEM HAADF image of a) CNC-CL, b) CNC-WP, c) CNC-S and d) CNC-NS. Reproduced with permission from Ref.[13,50]

In figure 16c the crystals of CNC-S sample appear in the form of rod-like whiskers, with length about 200 nm and 20 nm or less thick. In figure 16d, particles in CNC-NS sample are in the form of tangled crystals, embedded in amorphous material. This fact prevented us to study the individual crystals. The images of both samples are evidently noisy due to the short acquisition time, necessary to avoid the fast contamination under the beam irradiation.

The EDX technique is particularly useful to evaluate the dispersion of metal nanoparticles on CNC samples. As shown in figure 17c (in which the maps on silver nanoparticles is reported), the Ag nanoparticles are homogenously dispersed onto the nanocrystals (CNC-CL/Ag). The Ag NPs diameter measured is in the range 8−10 nm. On CNC-WP/Ag several AgNPs aggregation is observed.

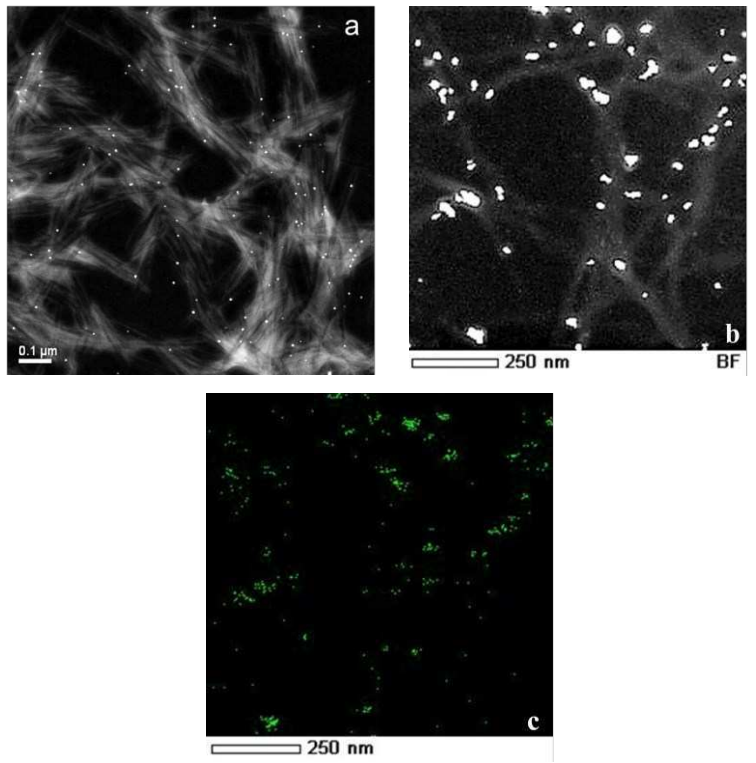

Figure 17- STEM HAADF images of a) CNC-CL/Ag, b) CNC-WP/Ag and c) EDX map of CNC-WP/Ag reported in b). Reproduced with permission from Ref. [13]

4.10- Solid-state NMR (SSNMR)

^{1}H-^{13}C CP MAS spectra were acquired on a sample of commercial cellulose nanocrystals (CNC) and on samples of sulphated CNC (CNC-CL), oxidized CNC (TOCNC6) and amidated CNC (CNC-NH), in order to monitor and verify the modification of the material and also to value the crystallinity degree of the samples.

The carbon atoms are labelled as indicated in the scheme below (figure 18).

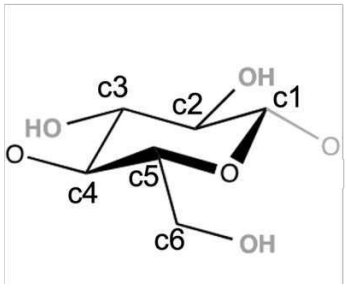

Figure 18- Anidroglucose unit reporting the conventional labelling scheme for the carbon atoms

As shown in figure 19 in all spectra signals of cellulose carbons are observed in characteristic spectral regions: signals of C1 between 104 and 106 ppm, signals of C2, C3, and C5 between 71 and 76 ppm, signals of C4 between 82 and 90 ppm, and signals of C6 between 62 and 66 ppm[95–98]. The spectra of CNC and CNC-NH show broader lines, indicating a lower degree of order for these samples.

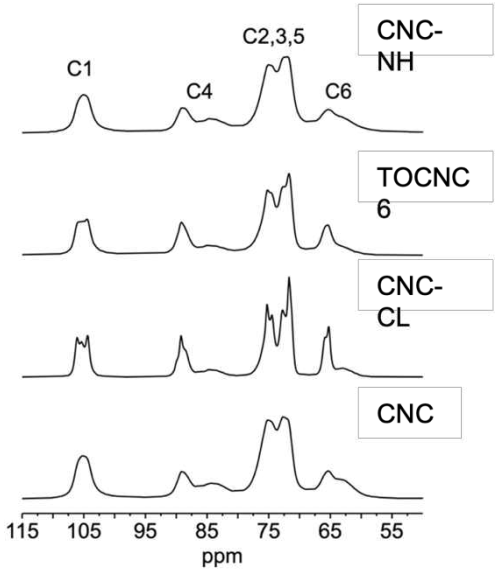

Figure 19- ^{1}H-^{13}C CP MAS spectra of samples CNC, CNC-CL, TOCNC6, and CNC-NH, acquired under the following experimental conditions: spinning frequency 15 kHz, 4000 scans for CNC; spinning frequency 14 kHz, 20000 scans for CNC-CL; spinning frequency 15 kHz, 400 scans for TOCNC6; spinning frequency 9.5 kHz, 11600 scans for CNC-ace; spinning frequency 15 kHz, 3000 scans for CNC-NH.

For the C4 carbon, the sharper structured signal between 88 and 90 ppm can be ascribed to cellulose carbons in the interior of nanocrystals (NCs), while the broader featureless signal centered at about 84 ppm can be assigned to cellulose chains on the surface of NCs. In the literature, a detailed assignment of peaks in the C4 spectral region has been performed, as follows[99–104]: crystalline I_α cellulose at 89.4-90.3 ppm; crystalline I_α+I_β cellulose at 88.7-89.5 ppm; crystalline I_β cellulose at 87.9-88.6 ppm; paracrystalline cellulose (crystalline domains in fibrils with higher mobility, or lower order, than cellulose I_α and I_β) at 88.1-88.6 ppm; accessible cellulose fibril surface at 84.4-84.9 ppm and 83-83.5 ppm; inaccessible cellulose fibril surface at 83.8-84.2 ppm. Higher chemical shift values were reported by Kono[105], most probably because of a different chemical shift referencing. Cellulose on fibril surfaces has also been indicated by some authors as amorphous cellulose.

On the other hand, peaks of C6 centered at about 65 ppm and 62 ppm have been ascribed to *tg* and *gt* conformations of the exocyclic CH_2OH group, in turn associated to crystalline and amorphous cellulose components, respectively[98].

For the remaining cellulose carbons, signals arising from amorphous cellulose underlie those from crystalline cellulose.

Finally, the resolved peaks observed for C1 have been assigned to crystalline I_α and I_β cellulose: carbons in I_α crystals give signals at 104.9-105.6 ppm, while those in I_β crystals resonate at 105.6-106.3 and 103.9-104.5 ppm[99,103,104]; again, higher chemical shifts were reported by Kono[105]. Moreover, broad unresolved peaks were found by lineshape fitting by some authors at 104.5-105.0 and 102.4 ppm and ascribed to C1 carbons in less ordered cellulose components[99].

The relative intensity of the signals from interior (crystalline) and surface (amorphous) cellulose in CNCs can be exploited to estimate the relative amounts of the different components and a crystallinity index (*CI*)[106,107]. Considering the signal overlap, a univocal deconvolution of the different components

contributing to the C4 signal is possible only when all of them give peaks at least partially resolved in the spectrum. On the other hand, the intensity of C6 signals can be used to estimate the ratio between *tg* and *gt* conformations, also related to cellulose crystallinity. Finally, the relative intensities of the signals arising from the C1 carbons and from the crystalline components of the C4 carbons can be employed to evaluate the relative content of crystalline I_α and I_β cellulose.

To determine the contributions from the different crystalline and amorphous cellulose components, a fitting of the spectral lineshapes was performed using the non-linear least squares procedure implemented in the SPORT-NMR software[108]; the results are reported in figures 20-23 and Tables 9-12. In all cases, the fitting was performed following the literature and using the minimum number of peaks to reproduce the spectra in order to avoid overinterpretation. Lorentzian, Gaussian, or mixed Lorentzian/Gaussian functions were used depending on the signal.

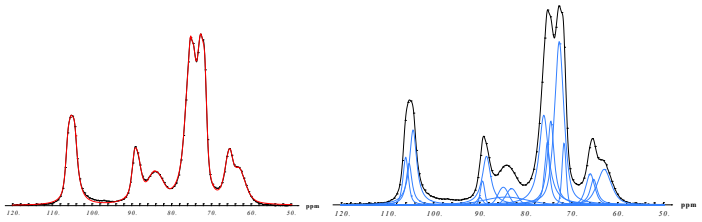

Figure 20- Fitting of the ^{1}H-^{13}C CP MAS spectrum of CNC at a spinning frequency of 15 kHz with peaks reported in Table 9. Left: experimental (black) and calculated (red) spectra; right: experimental spectrum (black) and peaks used in the fitting (blue).

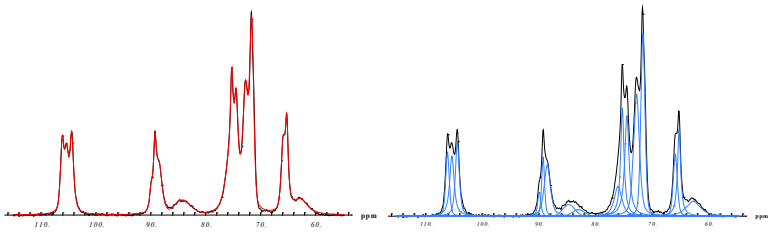

Figure 21- Fitting of the ^{1}H-^{13}C CP MAS spectrum of CNC-CL at a spinning frequency of 14 kHz with peaks reported in Table 10. Left: experimental (black) and calculated (red) spectra; right: experimental spectrum (black) and peaks used in the fitting (blue).

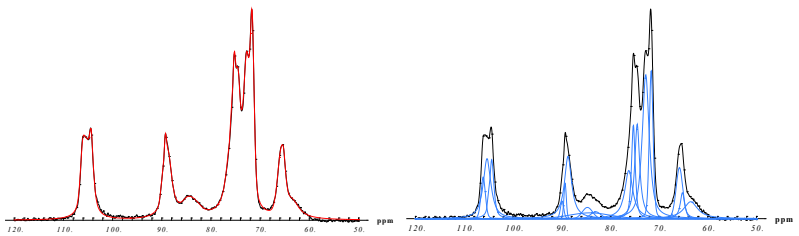

Figure 22- Fitting of the ^{1}H-^{13}C CP MAS spectrum of TOCNC6 at a spinning frequency of 15 kHz with peaks reported in Table 11. Left: experimental (black) and calculated (red) spectra; right: experimental spectrum (black) and peaks used in the fitting (blue).

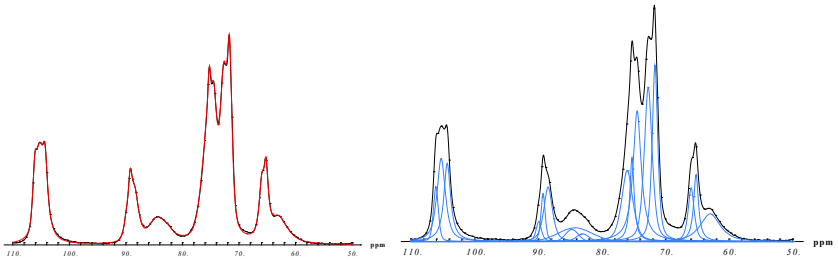

Figure 23- Fitting of the ^{1}H-^{13}C CP MAS spectrum of CNC-NH at a spinning frequency of 5 kHz with peaks reported in Table 12. Left: experimental (black) and calculated (red) spectra; right: experimental spectrum (black) and peaks used in the fitting (blue).

Three peaks were used to reproduce the C1 signal, with chemical shift of 106.0-106.1, 104.3-104.4 ppm, and 105.2-105.3, ascribable to crystalline I_β cellulose the first two and to I_α cellulose the latter. For the C4 carbon, three peaks at 89.9, 89.2-89.3, and 88.4-88.7 ppm were employed for the crystalline components, while three broader peaks were necessary for the superficial cellulose at 84.7-84.8, 84.2, and 83.0 ppm. It must be pointed out that, for the crystalline components, the content of paracrystalline cellulose and I_β cellulose could not be determined independently because of the quite close chemical shift values of their signals, both most probably contributing to the peak at 88.4-88.7 ppm. Moreover, the broad and featureless signal of the superficial components did not allow a univocal discrimination of surface carbons in accessible and inaccessible crystallite surface regions. For C2, C3, and C5 carbons, signals were found at 76.0-76.2, 75.2-75.3, 74.4-74.5, 72.6-72.7, and 71.6 ppm for all samples. For the

C6 carbon, two signals at 65.8-66.0 and 65.2 ppm were found for the crystalline component and a broad signal at 62.7-63.5 ppm for the amorphous one.

Table 9- Best fit values of the chemical shift and relative area of peaks obtained from the analysis of the ^{1}H-^{13}C CP MAS spectrum of CNC shown in fig. 20

Chemical shift (ppm)	**Area (a.u.)**	**Area %**	**Assignment**	
106.00	41.7	3.6	C1	16.6
105.21	45.4	3.9		
104.40	105.1	9.1		
89.90	6.3	0.54	C4cryst	8.6
89.30	14.45	1.2		
88.45	78.9	6.8		
84.80	24.5	2.1	C4am	8.2
84.20	45.3	3.9		
83.00	25.0	2.2		
76.00	162.2	14	C2,3,5	52.8
75.25	54.4	4.7		
74.47	107.1	9.3		
72.64	251.7	22		
71.60	36.1	3.1		
65.90	43.7	3.8	C6cryst	6.7
65.17	34.6	3.0		
62.87	80.8	7.0	C6am	7.0

Table 10- Best fit values of the chemical shift and relative area of peaks obtained from the analysis of the ^{1}H-^{13}C CP MAS spectrum of CNC-CL shown in fig. 21

Chemical shift (ppm)	Area	Area %	Assignment	
106.11	27.0	4.4	C1	16.8
105.33	37.7	6.2		
104.37	37.8	6.2		
89.90	9.20	1.5	C4cryst	11.5
89.23	20.5	3.4		
88.50	40.4	6.6		
84.70	14.6	2.4	C4am	3.8
84.20	0.400	0.06		
83.00	8.30	1.4		
76.00	29.9	4.9	C2,3,5	52.1
75.25	53.2	8.7		
74.44	63.3	10		
72.73	85.8	14		
71.61	86.4	14		
65.90	29.7	4.9	C6cryst	11.3
65.23	39.5	6.5		
62.70	28.2	4.6	C6am	4.6

Table 11- Best fit values of the chemical shift and relative area of peaks obtained from the analysis of the ^{1}H-^{13}C CP MAS spectrum of TOCNC6 shown in fig. 22

Chemical shift (ppm)	Area	Area %	Assignment	
106.09	23.9	2.9	C1	16.9
105.29	76.4	9.3		
104.34	39.0	4.7		
89.90	7.60	0.92	C4cryst	11.5
89.28	10.7	1.3		
88.68	76.5	9.3		
84.70	14.1	1.7	C4am	6.3
84.20	28.8	3.5		
83.00	8.80	1.1		
76.20	67.0	8.1	C2,3,5	52.6
75.27	52.3	6.4		
74.48	79.7	9.7		
72.73	159	19		
71.61	74.8	9.1		
65.81	44.3	5.4	C6cryst	7.7
65.20	19.2	2.3		
63.50	40.4	4.9	C6am	4.9

Table 12- Best fit values of the chemical shift and relative area of peaks obtained from the analysis of the ^{1}H-^{13}C CP MAS spectrum of CNC-NH shown in fig. 23

Chemical shift (ppm)	Area	Area %	Assignment	
106.08	25.10	2.8	C1	18.1
105.25	75.30	8.5		
104.30	60.90	6.9		
89.90	10.70	1.2	C4cryst	8.7
89.23	19.50	2.2		
88.44	47.20	5.3		
84.70	12.80	1.4	C4am	6.7
84.20	38.60	4.3		
83.00	8.200	0.92		
76.00	76.40	8.6	C2,3,5	51.9
75.25	41.80	4.7		
74.44	123.8	14		
72.70	120.3	14		
71.64	99.00	11		
65.95	33.60	3.8	C6cryst	8.0
65.18	37.60	4.2		
62.96	58.20	6.6	C6am	6.6

The areas of the C4 signals arising from the interior and the surface of crystallites (Tables 9-12) were employed to determine *CI* values for all the samples; the results are shown in Table 13. For comparison, *CI* values were also determined by signal integration; to this end, areas were measured in the spectral regions between 80 and 93 ppm ($A_{80\text{-}93}$, from all C4 signals) and between 86.5 and 93 ppm ($A_{86\text{-}93}$, from crystalline C4 signals) and *CI* was calculated as (7):

$$CI = \frac{A_{86-93}}{A_{80-93}} \times 100 \qquad (7)$$

The obtained results are reported in Table 13. As can be observed, similar *CI* values were obtained with the two methods, the larger discrepancy being observed for CNC-CL. The latter sample shows the highest *CI* value (about 71-75 %), while the lowest value was found for CNC (about 50%); for the other samples *CI* is about 60%.

The relative intensities of the C4 signal components can also be employed to estimate the lateral dimensions of cellulose fibrils (*LFD*s)[100,106]. In particular, assuming that cellulose NCs have a square cross-section, *q*, which is determined by the ratio between cellulose on the NC surface and total cellulose in the fibrils, i.e., the complement of CI/100 to 1, is related to the number of cellulose polymer chains perpendicular to the NC cross-section, *n*, by the equation (8):

$$q = \frac{4n-4}{n^2} \qquad (8)$$

Using an average dimension of 0.57 nm per cellulose polymer, a mean value of *LFD* can be calculated as (9):

$$LFD = 0.57 \times n \qquad (9)$$

The values of *LFD* found for our samples are reported in Table 13. As it can be observed, larger *LFD* values are associated to higher *CI* values: CNC-CL shows the largest fibrils (about 8 nm), whereas the average fibril dimension is only 4 nm in CNC; the other samples have *LFD* values on the order of 5-6 nm. Moreover, the ratio between the relative intensities of the C6 peaks centered at about 65 ppm and 62 ppm were employed to estimate the ratio between *tg* and *gt* conformations; the obtained results are reported in Table 13. Being the *tg*/*gt* ratio

related to the ratio between crystalline and amorphous cellulose, this parameter follows a trend analogous to that of *CI*.

Table 13- Crystallinity index (CI), lateral fibril dimension (LFD), and ratio between tg and gt conformations, determined for the indicated samples by spectral analysis and signal integration. Errors are ±1 on the last digit.

Sample	**s.r.**	**probe**	**Method**	***CI***	***LFD***	***tg/gt***
CNC	15 kHz	4 mm	integration	51 %	4.0 nm	
CNC	15 kHz	4 mm	fitting	51 %	4.0 nm	1.0
CNC-CL	14 kHz	2.5 mm	integration	72 %	7.5 nm	
CNC-CL	14 kHz	2.5 mm	fitting	75 %	8.5 nm	2.5
TOCNC6	15 kHz	4 mm	integration	64 %	5.7 nm	
TOCNC6	15 kHz	4 mm	fitting	65 %	5.9 nm	1.6
CNC-NH	5 kHz	4 mm	integration	58 %	4.8 nm	
CNC-NH	5 kHz	4 mm	fitting	56 %	4.5 nm	1.2

Besides the signals of cellulose carbons, signals arising from added functional groups can be observed in the spectra of TOCNC6 (figure 24), and CNC-NH (figure 25). In particular, a peak at 174.9 ppm is observed for the COOH carbon of TOCNC6[109–111] and peaks at about 40 and 175 ppm are observed for the CH_2 and CO carbons of CNC-NH[112,113]. In all cases, the very small signals observed for the functional groups indicate a very low functionalization degree. A reliable quantification of the functionalization from signal areas is not possible because of the much lower intensities of these signals with respect to those of cellulose, as well as because the parameters used for recording the CP spectra do not guarantee that these signals were acquired quantitatively.

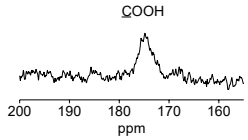

Figure 24- Expansion of the ^{1}H-^{13}C CP MAS spectrum of TOCNC6 in the spectral region showing the COOH signal.

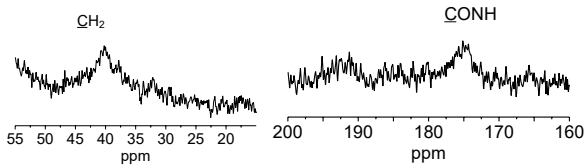

Figure 25- Expansions of the ^{1}H-^{13}C CP MAS spectrum of CNC-NH in the spectral region showing the CH_2 (left) and the CO (right) signals.

4.11- Biocidal activity

From growth experiments reported in figure 26, the CNC exerts a stimulating effect on the growth of Escherichia coli (figure 26a) with a better response of the cells to the CNC-WP. A comparable increase was observed in Bacillus subtilis (figure 26b), with a more evident response to CNC-CL at 50 ppm. To inhibit the growth of bacteria, CNC has been used as a carrier for silver nanoparticles, which, as it is known, show an efficient biocidal activity. As shown in figure 26, the presence of the colloidal silver suspension allows to define the minimum inhibitory concentration (MIC) for both bacteria: MIC on Escherichia coli is 12.5 ppm, while for Bacillus subtilis the MIC reaches 25 ppm. As reported by Bergamonti[13], this may be due to structural differences and the presence of functional groups present in the cell walls of bacteria. Moreover, the effect of silver nanoparticles on different bacteria has been reported in literature[114]. When the CNC acts as a carrier for the silver nanoparticles, a biocidal action efficacy

comparable to that of the sol Ag is observed by Zhang[115]: CNC-CL/Ag 12.5 ppm on E. coli or CNC-WP/Ag 25 ppm on B. subtilis.

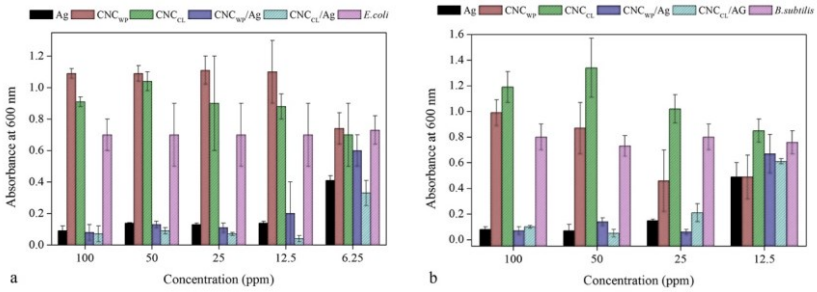

Figure 26- a) Growth of Escherichia coli and b) Bacillus subtilis with CNC, CNC/Ag and Ag nanoparticles at different concentrations

4.12- Elemental analysis

CHNS analysis was performed on some CNC dried samples reported in table 14. The results show that the presence of sulfur is evident only in the sample subjected to the acid hydrolysis with sulfuric acid, while the absence of sulfur for the CNC-H (HCl) and CMF samples is justifiable by the actual lack of surface sulphate groups due to the type of hydrolysis performed.

Table 14- CHNS analysis on CNC, CMF and functionalized CNC

Sample	C (%)	H (%)	N (%)	S (%)
CNC	40,31	6,13	/	1,05
CMF	41,96	6,18	/	/
CNC-H	42	6,20	/	/
CNC-APTES	40,31	6,22	1	0,49
CMF-APTES	41,72	6,38	0,54	/
CNC-NH	40,93	6,22	2,34	0,66

In agreement with what was found in the FTIR spectrum, the presence of nitrogen in the samples with APTES is an indication of an effective functionalization: these values are evident in table 14 and are absent in the starting materials.

5- Conclusions

Extraction of nanocellulose was obtained from pure cotton and from waste materials, such as wastepaper and artichoke waste. For each reaction carried out, the method was optimized to obtain the best yield % and the highest crystallinity of the product. In this chapter, attention has been given to the characterization of the two types of polymorphs that can be obtained: polymorph Iβ and polymorph II. The goodness of all reactions carried out was investigated through spectroscopic and diffractometric techniques. These allowed us to identify the functional groups, the size and the distribution of the nanocrystals, the type of polymorph and the crystallinity index. The surface charge and the thermal resistance of the sols have also been determined. After the CNC extraction, different reactions have been tested on these products to impart some characteristics such as, for example, a biocidal efficacy and hydrophobicity due to the presence of silver nanoparticles and PDMS, respectively. The CNC oxidation method was investigated: the aim in this case was to obtain the best oxidation degree, with the minimum use of reagents. Satisfactory results, in agreement with what is reported in the literature, have been obtained by the evaluations with conductimetric titrations. Further reactions are conducted to introduce functional groups on cellulose nanocrystals, for example, the amination reaction has been investigated: the presence of $-NH_2$ was confirmed by FTIR measurements and by CHNS analysis.

CHAPTER 2

CNC BASED MATERIALS FOR SUSTAINABLE TREATMENTS ON PAPER SAMPLES AND ON CANVAS PAINTINGS

1- Abstract

The second Chapter regards the use of nanocellulose suspensions as new and sustainable material to be used as preservative and consolidant for lignocellulosic substrates. In this study Whatman paper samples and painted canvas have been considered as supports[116,117].

To study the consolidating capacity of CNC-based treatments, samples of Whatman paper were used and mechanical strength tests were carried out[17,118,119]. Biocidal activity, imparted by specific metallic particles, which can be introduced into the treatment were evaluated [120–122].

The second part of the research activity concerned the study of the consolidating capacity of treatments based on CNC on several sets of canvas samples that reproduce the pictorial layers of a painting. The consolidating capacity was compared with that of the well-known commercial consolidant: Aquazol 500. The effect of consolidants after accelerated artificial aging of the samples was also evaluated by means of spectroscopic and colorimetric methods, to verify that the type of treatment does not alter the support over time.

2- Experimental

2.1- Materials

Nanocellulose suspensions obtained by method described in chapter 1, paragraph 2.2 was used at 1% (w/v) on paper and 1 ÷ 2 % (w/v) on canvas painting samples. The Aquazol 500 or Poli (2-etil-2ossazolina) was purchased from AN.T.A.RES srl (BO - Italy). CNC-Ag (chapter 1, paragraph 2.9) was applied only on Whatman paper samples. CNC-PDMS (chapter 1, paragraph 2.8) was used for hydrophobic treatment. The canvas 100% pure linen (weight 170 g/m^2, 9x9 wires/cm), lapin glue, gypsum of Bologna, Sienna natural pigment and linen oil were purchase from Cts srl (MI, Italy).

2.2- Treatment on Whatman paper samples with CNC-Ag

About 0.3ml of CNC-CL, CNC-WP and CNCs/Ag suspensions were applied by brush on Whatman paper samples (30 × 100 mm) in 3 passes with an interval of 20 min from each other. The treatments were applied also by immersion to evaluate the best method of application.

2.3- Treatment on Whatman paper samples with CNC-PDMS

The suspension CNC-PDMS obtained as described in chapter 1, paragraph 2.8, were applied on Whatman paper samples by brush to test the hydrophobicity. The treatment was applied in two passes following the perpendicular directions of the paper samples. The samples size was 3x10 cm.

2.4- Treatment on canvas

To obtain the painting canvas samples, the traditional painting technique was reproduced. The procedure involves the following steps (figure 1):

- The linen canvas was washed in boiling water and left to air dry without wringing it so as not to induce twists in the warp and weft threads. After drying, the canvas was divided into pieces to be tensioned: the new samples were aligned to the edges of the looms following the straight edge and stiffened with Lapin glue diluted in water, applied hot, to lock the warp and weft in a perpendicular position
- Preparation of the stucco: the Lapin glue was dissolved in a water bath and plaster of Bologna was added until a thick mixture was obtained. This mixture was spread on the canvas by brush in two successive layers applied with perpendicular directions to each other. After drying, the filler was leveled with sandpaper until a smooth layer was obtained. The porosity of this layer, preparatory to painting, was saturated with a diluted solution of Lapin glue (1:20 v/v)
- The color was prepared by mixing a natural Siena pigment with linseed oil. The dough was applied by brush over the preparation in two layers

Figure 1- *Sample preparation phases: a) evaluation of yarn orientations; b) tensioning on the frame; c-d) plaster and glue preparation; e - f) drafting of the preparatory layer; g-h) preparation of oil color; i) application of the pictorial layer in oil*

To investigate the interaction of the consolidant (CNC susoensions and Aquazol) with all the constituent layers of an oil painting, it was necessary to separate these layers and create three sets of samples:

- TE: canvas not treated
- GC: canvas with preparation layer (plaster and animal glue)
- CO: canvas with preparation layer and color (drying oil and pigment)

The samples were obtained after removing the pieces of canvas from the loom, cutting out 10x3 cm rectangles and subdividing them according to the

warp and weft directions. Similarly, a canvas previously painted with oil color was used as a reference (RIF).

On each sample set, CNC at 2% (w/v) was applied by brush. To compare the consolidation efficiency, Aquazol 500 was used at 4% (w/v): the powder was dispersed in distilled water at room temperature under vigorous magnetic stirring until complete dissolution.

Before and after the treatments, all samples were conditioned at 30 °C for 24h. To identify the individual samples, abbreviations were chosen which include the set of origin (TE = canvas, GC = plaster and glue, CO = colour, RIF = reference), the type of consolidator applied (NT = no treatment, CNC = nanocellulose crystalline, AQ = Aquazol 500) and yarn direction (MD = machine direction, CD = Cross machine). The treatments were applied on the back of each sample.

3- Characterization

The FTIR spectroscopy was performed according to chapter1 paragraph 3.5.

3.1- Weight percentage gain (WPG)

All the samples were conditioned in an oven at 23 °C, RH = 50 % for 24 h. They were then weighed before and after the treatments to determine the weight gain of the treated samples. The formula (1) was used to calculate the percentage gain:

$$WPG = \left(\frac{W_{tn} - W_0}{W_0}\right) \times 100 \qquad (1)$$

where W_{tn} the weight of the anhydrous sample after n treatment cycles and W_0 the weight of the anhydrous sample before treatment. A Sartorius mod CP 225 D analytical balance (d = 0.01 mg) was used to evaluate the changes in mass.

3.2- Colorimetry

The changes in the surface appearance of the cellulosic samples were determined by colorimetric measurements carried out by a Spectro- Densitometer TECHKON SpectroDens. At least 7 regions of a few mm^2 in area were examined and averaged on each sample, before and after the application of the consolidants, and before, during and after the accelerated artificial aging test, in both directions, to determine the total color difference ΔE* according to UNI EN 15886:2010. The CIELab reference system was considered, using D65 (6500 K) as standard illuminant and CIE 1964 (10 °) as standard observer. The three colorimetric coordinates are: L* the brightness (white-black opposition), a* (red-green opposition) and b* (yellow-blue opposition) chromaticity coordinates. The color difference (ΔE*), and the variation of the colorimetric coordinate b* (Δb*) were calculated according to the following formulas (2) and (3):

$$\Delta E^* = \sqrt{(\Delta L^{*2} + \Delta a^{*2} + \Delta b^{*2})} \qquad (2)$$

$$\Delta b^* = \sqrt{\Delta E^{*2} - \Delta L^{*2} - \Delta a^{*2}} \qquad (3)$$

If ΔE* > 3, the color variation is perceptible to the naked eye, if it is between 2 and 3 it is not perceptible, while if it is ΔE* < 1 it is not significant. However, for practical purposes, in some cases, color differences 3 < ΔE * < 6, although perceptible, are considered acceptable (UNI 8941-3: 1987). The value of Δb* is indicative to highlight any yellowing of the consolidants and samples. Positive values of b* indicate an increase in the yellow component; conversely, negative

values of b* indicate an increase in the blue component. If the value of b* > 1, the chromatic variation could be perceived with the naked eye.

3.3- Accelerate ageing

The samples were housed in the QUV®Accelerated Weathering Testers aging chamber of Q-Lab Corporation and exposed to UV radiation cycles (wavelengths between 365 nm and 295 nm, UVA-340 lamp with radiation of 0.68 W/m^2) and controlled temperature with the surface exposed to the lamps. Two temperature values have been set to be repeated in daily cycles up to a total of 206 h:
I cycle: T = 50 °C; UV = 0,68 W/m^2; t = 4 h
II cycle: T = 70 °C; UV = 0,68 W/m^2; t = 4 h

3.4- Contact angle

For the contact angle measurements, homemade instrumentation was used: calibrated horizontal plane on which the samples were positioned and illuminated in the perpendicular direction by a lamp whose light is filtered by an opaque plate to determine the exact profile of the water drop deposited on the surface of the sample. The measurement of the contact angle of the drop was calculated using the program “Image J”.

3.5- Mechanical test

Tensile strength measurements on paper (figure 2) and canvases were carried out according to ISO 1924-2:2008 standards. The samples (30×100×0.14mm)[123], were measured by a Universal Testing Machine (25 mm/min). Before test, all samples were conditioned at 23 °C, RH = 50 % for 24 h. For each treatment, 5 test pieces were analyzed and the results were averaged (TAPPI T 494, 2001[124]). The Tensile strength is the maximum tensile force (developed in the test

specimen before rupture) per unit width of test specimen (N/m); the stretch is the maximum tensile strain (developed in the test specimen before rupture) expressed as a percentage; the tensile index is the tensile strength (in N/ m) divided by grammage (in g/m^2) and the Tensile Energy Absorption (TEA) is calculated as the ratio between the area under load-elongation curve (in J) and the specimen surface (in m^2). Two perpendicular directions corresponding to MD (machine direction) and CD (cross machine direction), were considered to consider the anisotropy of the paper samples. Tensile strength of the samples treated with CNC and CNCs/Ag compared to the reference paper and all samples for the canvas sets were evaluated.

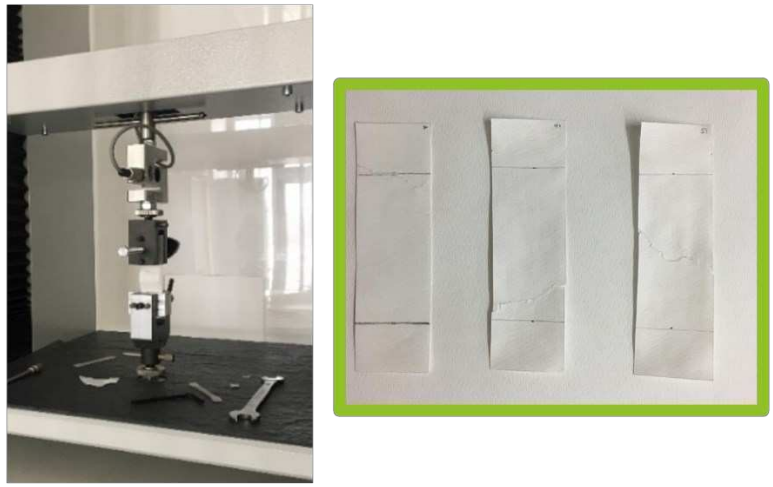

Figure 2- Paper sample during the mechanical test (left) and after the break (right)

The tensile strength of the samples was tested in the two directions of MD and CD and the average values of tensile strenght (σ), percentage elongation (ε%) were obtained by means of equations (4) and (5) respectively:

$$\sigma = \frac{F}{A_0} \qquad (4)$$

where F is the maximum force supported by the sample before breaking and A_0 is the initial section of the sample;

$$\varepsilon\% = \frac{L_1 - L_0}{L_0} * 100 \quad (5)$$

where L_1-L_0 is the increase recorded by the instrument and L_0 is the distance between the terminals.

The energy absorbed by the samples before breaking, which is an index of their toughness, was obtained from the area underlying the stress / strain diagram before breaking according to equation (6):

$$toughness = \int_{\varepsilon_0}^{\varepsilon_{max}} \sigma(\varepsilon) d\varepsilon \quad (6)$$

3.6- Biocidal activity

The effect of CNC based treatments on paper was evaluated by spotting *Aspergillus niger* fungus spores onto 4 different pieces of Whatman paper (1 cm^2), one without any treatment, the others coated with CNC suspension, silver nanoparticles and their mix. The inoculated paper pieces were placed on Czapek Dox agar and incubated for one week at 30 °C. The development of the colony was then observed.

4- Results and discussions

4.1- Weight Percentage Gain (WPG)

To determine which is the method of applying a surface treatment on paper samples, two methods were tested: brush deposition and immersion of the sample. The WPGs relating to both methods were calculated, as shown in table

1. For Whatman paper samples treated with CNC sol by brush and dried in oven at 60 °C for 2 h, the weight percentage gain was on average 1.5 % (± 2). The application of CNC by immersion gives higher WPG values with respect to the application of the same sol by brush, but, in this case, the samples dried resulted deformed. For this reason, all subsequent treatments were applied by brush.

Table 1- *WPG calculated for all paper samples treated with different application method*

Samples	Treatment	WPG
S 1	CNC by brush	2,2
S 2	CNC by brush	1,6
S 3	CNC by brush	1,3
S 4	CNC by brush	1,4
S 5	CNC by brush	1,6
S 6	CNC by immersion	2,5
S 7	CNC by immersion	2,3
S 8	CNC by immersion	2,5
S 9	CNC by immersion	2,1
S 10	CNC by immersion	3,7
S 11	CNC-PDMS by brush	3,4
S 12	CNC-PDMS by brush	3,8
S 13	CNC-PDMS by brush	3,2
S 14	CNC-PDMS by brush	4,5
S 15	CNC-PDMS by brush	3,2
S 16 (MD)	CNC-Ag by brush	1,4
S 17 (CD)	CNC-Ag by brush	1,6

The CNC-Ag sol was tested as consolidant and to evaluate the biocidal activity. The WPG was calculated on Whatman paper samples in both directions on which the treatment was applied and the values, shown in table 1, are comparable with those obtained by application of CNC by brush. In this case, the recorded WPG has values of 1.4 and 1.6 for S16 and S17samples, respectively.

Aquazol (AQ) was chosen as the reference treatment to compare the CNC-based method. The WPG values obtained after the treatments on the canvas are shown in table 2 and compared with those with CNC. For the TE set there is a greater quantity of consolidant thanks to the hydrophilic nature of the textile fibers. The gain is drastically reduced for the GC, CO and RIF sets, where the fibers are isolated by the animal glue and on the surfaces, there are multiple layers of other more or less hydrophilic materials.

Table 2- WPG calculated on each set of canvas. Both directions (MD and CD) are reported. Standard deviation in parentheses.

Sample	Direction	WPG
TE-CNC	MD	4,1 (3)
TE-CNC	CD	3,9 (2)
TE-AQ	MD	8,3 (4)
TE-AQ	CD	8,2 (5)
GC-CNC	MD	0,5 (1)
GC-CNC	CD	0,6 (3)
GC-AQ	MD	0,7 (3)
GC-AQ	CD	0,6 (1)
CO-CNC	MD	0,1 (2)
CO-CNC	CD	0,1 (1)
CO-AQ	MD	0,1 (2)
CO-AQ	CD	0,2 (1)
RIF-CNC	MD	0,2 (1)
RIF-CNC	CD	0,2 (1)
RIF-AQ	MD	0,2 (1)
RIF-AQ	CD	0,3 (1)

4.2- Fourier Transform Infrared Spectroscopy (FTIR)

FTIR spectroscopy gives information about the interactions between the substrate and the consolidant material, and it can also detect modification of the materials after the treatment or after the accelerating ageing.

The FTIR spectrum of Whatman paper samples (figure 3) treated with CNC does not show differences compared to untreated Whatman paper samples which have the same characteristic peaks of cellulose. In the FTIR spectrum of the paper treated with the CNC-PDMS, the signals at 1261 cm^{-1} and 802 cm^{-1} are clearly distinguishable attributable to PDMS, as described in chapter 1, paragraph 4.5.

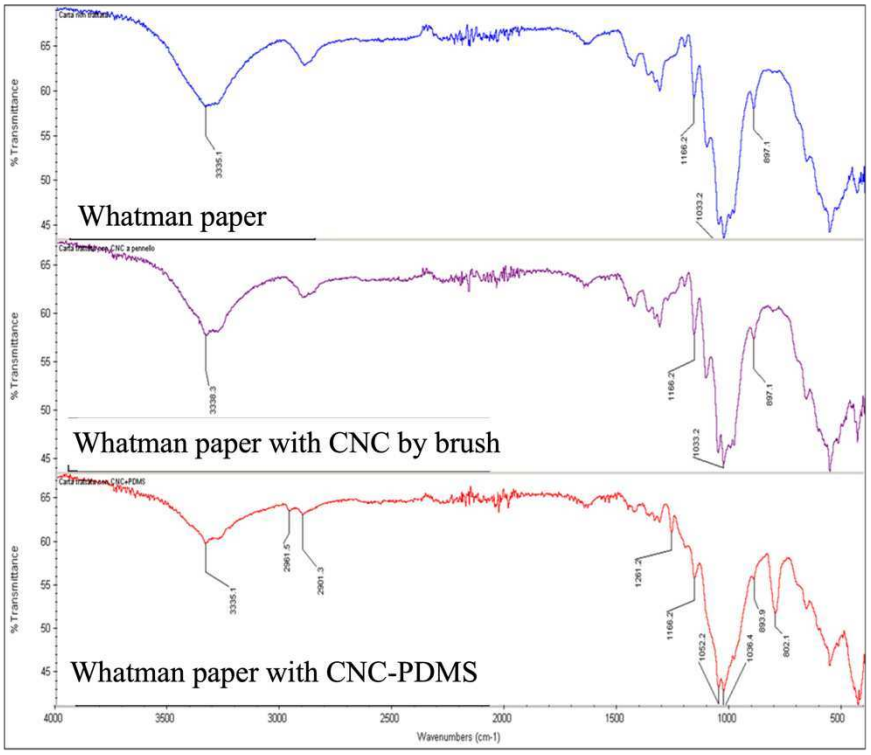

Figure 3- *FTIR spectra acquired on Whatman paper untreated, treated with CNC by brush and CNC-PDMS*

In figure 4a the FTIR spectrum acquired on not treated canvas is reported. The signals characteristic of the cellulosic materials are evident: in the region 3300-

2855 cm^{-1} the stretching vibration of the OH and CH groups are present and in the region at 1160-1100 cm^{-1} there are stretching vibrations of the C-O-C groups. The FTIR spectrum acquired on the Aquazol powder (figure 4b) shows the typical pattern of this consolidant. As reported in literature[125,126] the spectrum is characterized by the typical stretching vibrational bands due to the tertiary amide: the peak at 1630 cm^{-1} and 1470 cm^{-1} are assigned to the νC=O and νC-N, respectively. The peaks at 2970 cm^{-1}, 2940 cm^{-1} and 2880 cm^{-1} are of the stretching vibration of CH_2 and CH_3 groups, while their vibrational bending are evident at 1419 cm^{-1}, 1373 cm^{-1} and 1320 cm^{-1}. The C-C stretching vibrational peak are present in the region between 1240-1060 cm^{-1}. For the siccative oil (figure 4c) the characteristic FTIR peaks and their assignment are reported below:

- at 3416 cm-1 the OH vibrational stretching
- at 3010 cm-1 the band of olefinic CH stretching vibration
- at 2924 cm^{-1} e 2853 cm^{-1} are present the peaks assigned to symmetric and asymmetric vibrational stretching of methylene groups $–CH_2$, respectively
- the strong stretching vibration of C=O of the fatty acid ester is at 1743 cm^{-1}
- in the region 1450 cm^{-1} e 1300 cm^{-1} bands related to the bending vibration of aliphatic $-CH_2$ are evident
- the band at 719 cm^{-1} is assigned to the rocking vibration of the methylene groups
- the stretching vibration of C-O groups is at 1159 cm^{-1}

Lapin glue is of animal origin and consists of a dispersion with a high collagen content. As reported in literature[127–129] the stretching vibration of amidic group N-H is at 3273 cm^{-1}. The two peaks at 2925 cm^{-1} and 2857 cm^{-1} are assigned to asymmetric and symmetric CH_2, respectively. In the region

1630-1446 cm^{-1} are present the stretching vibration of C=O, the bending vibration of N-H and the stretching vibration of C-N (figure 4d).

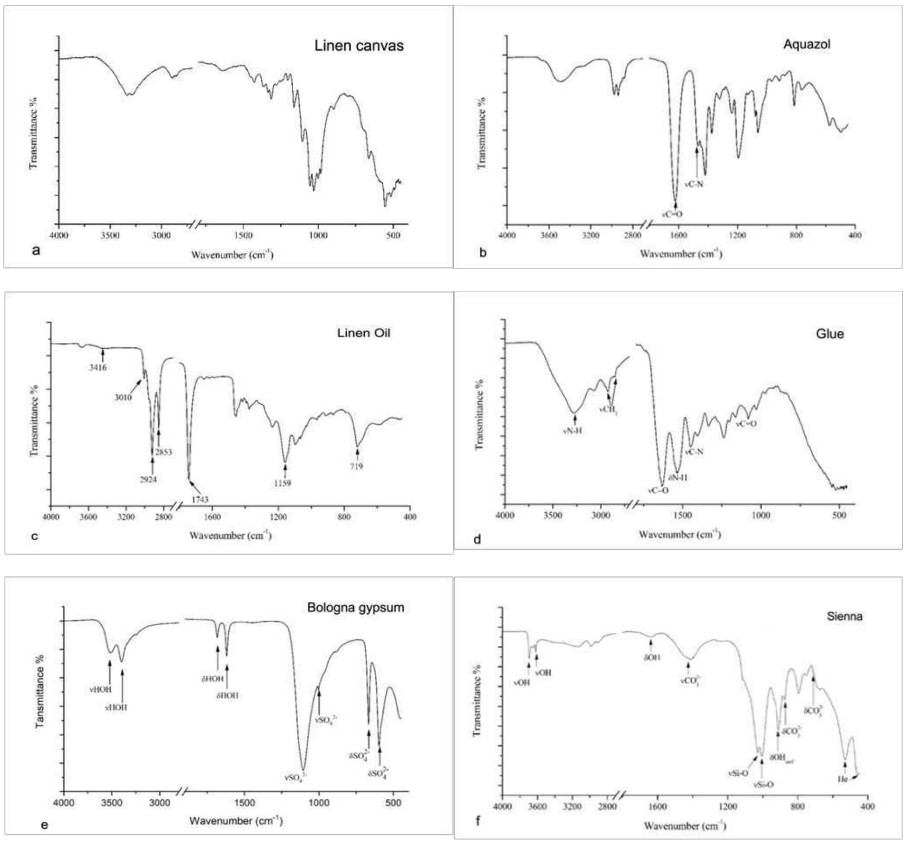

Figure 4- *FTIR spectra on a) canvas linen, b) Aquazol 500, c) siccative oil, d) Lapin glue, e) Bologna gypsum and f) Sienna pigment*

In figure 4e the FTIR spectrum of the gypsum is reported[130,131]: the stretching vibration of asymmetric and symmetric OH (crystallization water) are at 3514 cm^{-1} and 3398 cm^{-1}, respectively. The bending vibration (δH-O-H) of crystallization water are at 1682 cm^{-1} e 1620 cm^{-1}. The sulfate group present the features at 1107 cm^{-1} (asymmetric νSO_4^{2-}) and at 981 cm^{-1} (symmetric νSO_4^{2-}). At 667 cm^{-1} and 598 cm^{-1} the bending vibration of δSO_4^{2-} is observed. Sienna is a pigment of mineral origin containing calcium carbonate, kaolinite, gypsum, quartz and oxides (hematite, goethite) and iron hydroxides[132]. In the spectrum

reported in figure 4f, the peaks at 3695 cm^{-1} and at 3615 $cm^{-1}$are assigned to interlayer water stretching vibration in the crystal lattice of kaolinite. The νSiO of the kaolinite lattice are present at 1030 cm^{-1} and at 1005 cm^{-1}. The features of calcium carbonate are present at 1430 cm^{-1}, 873 cm^{-1} and 710 cm^{-1} as indicated by the arrows. The peaks at 530 cm^{-1} and at 458 cm^{-1} can be attributed to hematite. The comparison of the FTIR spectra between the sets treated with CNC and Aquazol, before and after the accelerated ageing, are reported in figures 5-8. For the set TE, the features of the cellulose are evident as discussed above. In the sample with Aquazol (figure 5a) the two peaks at 1630 cm^{-1} and at 1420 cm^{-1} related to the treatment applied are highlighted with an asterisk. After the accelerated ageing (figure 5b) in the sample not treated peaks (indicates with triangles) due to the depolymerization[133] are present: at 1748 cm^{-1} is present the stretching assigned to the carboxyl group, at 1692 cm^{-1} the presence of diketone vibrational stretching and at 1369 cm^{-1} and 1222 cm^{-1} the stretching vibrations of the C-O groups are found. In figure 6 the FTIR spectra of the set GC are reported. Obviously, the signals of gypsum are predominant respect to those of cellulose and glue. After accelerate ageing (figure 6b) only small variations in the intensity of the bands associated with the Lapin glue are noted, highlighted in the figure with circles. In figure 7a the features of the different materials present in the samples CO indicated with letters T (canvas), G (gypsum), O (siccative oil) and S (Sienna) are evident. After accelerated ageing (figure 7b) in all samples, except in the sample treated with CNC, the stretching vibration of CH_2 decreases in intensity, as well as that relating to bending, probably due to the rupture of the hydrocarbon chains of the oil. From the comparison before and after accelerated artificial aging both treatments make the sample more resistant to oxidative processes triggered by temperature and UV radiation. In figure 8a the stretching vibration of the protein component (indicated with C*) is evident, shifted to lower wavenumbers respect to the modern reference glue. As in the CO set, also in the

case of the reference sample, the treatments seem to slow down the oxidative phenomena that occur in the linseed oil during ageing.

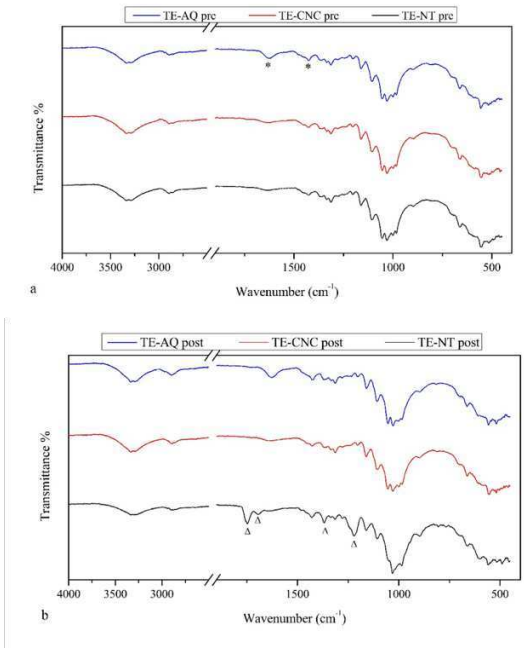

Figure 5- *comparison between the FTIR spectra of the TE sample set: a) before aging: b) after aging. The asterisk indicates the absorption bands of AQ, the triangles the changes in the absorption bands after accelerated ageing*

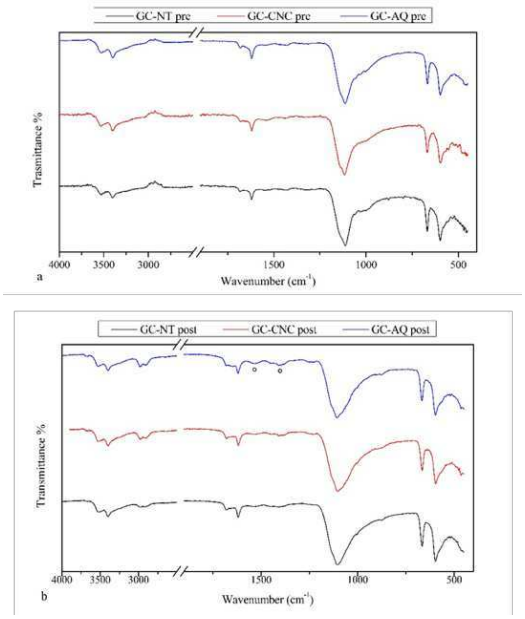

Figure 6- *comparison of the FTIR spectra of the GC sample set: a) before aging: b) after ageing. The circles indicate the characteristic bands of the animal glue*

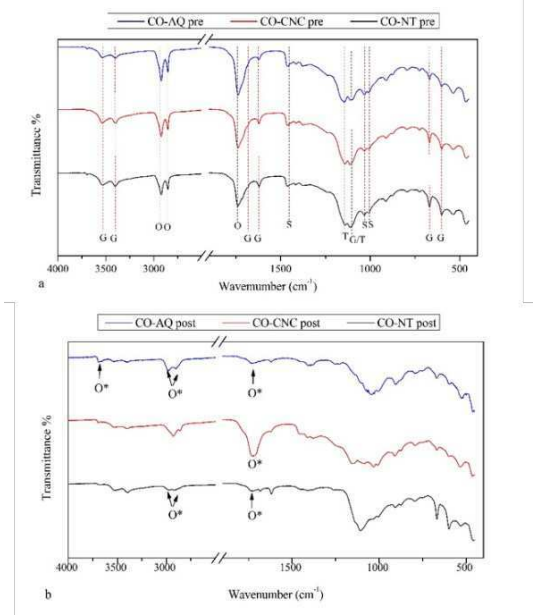

Figure 7- *comparison between the FTIR spectra of the CO sample set: a) before aging: b) after ageing. The alphabetical abbreviations refer to the materials making up the layers of the sample*

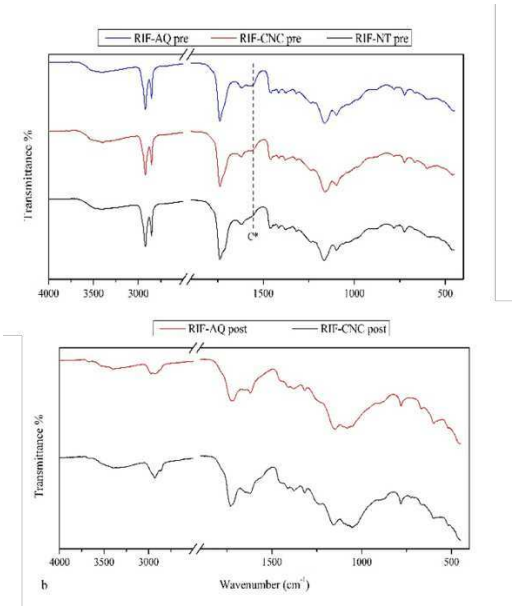

Figure 8- *comparison between the FTIR spectra of the RIF sample set: a) before aging: b) after ageing*

4.3- Colorimetry measurement

4.3.1- Treatment on paper with CNC and CNC/Ag

The colorimetric measurements were carried out on Whatman paper sample before and after the treatments with CNC and CNC/Ag suspensions to verify that the surface of the paper samples was not altered. The total color difference ΔE* for CNC is 0.8 ± 0.1, (S1-5 samples) whereas the addition of Ag nanoparticles slightly increases its value (ΔE* = 1.8 ± 0.4 for S16 and 1.5 ± 0.3 for S17 sample): we may then conclude that the color change before and after treatment is not significant to the human eye.

4.3.2- Treatment on paper with CNC-PDMS

The colorimetric variation of Whatman paper coated with the CNC-PDMS suspension was evaluated. The results reported in table 3 show the good

efficiency of the CNC treatment by brush and by immersion. All samples have ΔE* values less than 3, indicating that the treatments are not perceptible to the human eyes. At the same, for Δb* coordinate, the positive increments of the values versus the yellowing are not relevant. Similarly, the CNC-PDMS treatment does not produce colorimetric variation.

Table 3- *Evaluation of colorimetric variation of CNC-PDMS treatment. In parentheses are reported the standard deviation.*

Sample	**ΔE***	**Δb***
S 1	1,5 (4)	0,2 (0,5)
S 2	0,7 (1)	0,1 (0,5)
S 3	1 (0,5)	0,1 (0,7)
S 4	1,7 (2)	0,05 (1)
S 5	1,2 (2)	0,1 (0,7)
S 6	1,3 (1)	0,2 (0,5)
S 7	0,9 (2)	0,1 (0,4)
S 8	0,8 (2)	0,1 (0,5)
S 9	0,6 (1)	0,05 (2)
S 10	1,1 (0,5)	0,1 (0,5)
S 11	1,3 (0,2)	0,2 (0,5)
S 12	0,9 (0,2)	0,1 (0,2)
S 13	1 (0,5)	0,05 (0,3)
S 14	1,2 (0,1)	0,2 (0,1)
S 15	0,7 (0,2)	0,1 (0,3)

4.3.3- Treatments on canvas with CNC compared to AQUAZOL

Before and after the treatment applications on each set of painting canvas, ΔE* and Δb* were calculated following the formula (2) e (3). In table 4 the values obtained for the two directions are reported. Except for the sets TE-AQ in both

directions, in all other cases ΔE* result under the value 3 that represent the limit of perception. For the Δb* only the sets TE-AQ and RIF-AQ in both directions, have values higher than the limit imposed by the UNI EN 15886:2010.

Table 4- *Colorimetric variation calculated on canvas sets before and after accelerate ageing*

Sample	Direction	ΔE* before ageing	ΔE* after ageing	Δb* before ageing	Δb* after ageing
TE-NT	MD	-	5	-	2
TE-NT	CD	-	5	-	1,6
TE-CNC	MD	1,8	6	0,4	2,2
TE-CNC	CD	1,6	6	0,4	2
TE-AQ	MD	3,6	10	1,6	1,8
TE-AQ	CD	3,2	9	1,7	1,2
GC-NT	MD	-	0,8	-	0,4
GC-NT	CD	-	0,9	-	0,5
GC-CNC	MD	1,1	2	0,2	0,6
GC-CNC	CD	1,3	3	0,4	1
GC-AQ	MD	0,6	1,6	0,2	0,6
GC-AQ	CD	0,8	1,8	0,4	0,7
CO-NT	MD	-	5	-	6
CO-NT	CD	-	9	-	8
CO-CNC	MD	1,9	6	1,1	5
CO-CNC	CD	2,1	7	0,9	6
CO-AQ	MD	0,8	6	0,6	8
CO-AQ	CD	1,1	9	0,9	9
RIF-CNC	MD	1,8	6	1,3	5
RIF-CNC	CD	1,2	9	0,9	8
RIF-AQ	MD	2,9	10	1,9	6
RIF-AQ	CD	1,9	13	1,5	10

After artificial ageing the increments of ΔE* and Δb* are evident for all samples set. Generally, the major increment, in terms of ΔE*, is registered for the treatments with Aquazol, while the use of CNC is under the limit imposed by

UNI 8941-3: 1987. Probably the Bologna plaster mixed with animal glue applied in this preparation layer is not affected by photooxidative ageing, at least under the applied conditions. The color variation of the CO sets is due to the photooxidative aging of the linseed oil. It is observed that the samples oriented with CD give higher values of ΔE* in all sets (except GC in which however the color variation is negligible). Probably the orientation of the samples affects the penetration of the consolidant. In fact, the warp is thinner and more twisted, and, in the tensioning of a canvas, it is the one that has more stretching. The samples obtained with the long side parallel to the warp have a greater density of voids which allow greater penetration even for a large molecule such as that of Aquazol 500, which, in most cases, proves to cause greater color variations. For the Δb*, only the tests on the set GC are under the perception limit. For all the other samples, the increase of this component is recorded as a tendency towards yellowing. The yellowing is consistent with the photooxidative degradation of the siccative oil.

4.4- Contact angle measurement

This investigation was performed to evaluate the hydrophobicity of the treatment with PDMS applied on the Whatman paper samples. This parameter is fundamental because it considers the possibility of protecting a paper artwork from humidity or preserving its integrity. The measurement of the contact angle allows us to numerically evaluate whether a surface can be defined as hydrophobic or not. In figure 9 reports the image of a water drop deposited on a not treated Whatman paper sample (figure 9a) and on a sample treated with CNC-PDMS (figure 9b). The absence of any treatment allows the water drop to be completely absorbed by the hydrophilic surface. Figure 9b shows the presence of water drop: the hydrophobicity was estimated by contact angle measured that

correspond to 113°. This value, even if not high enough to allow super hydrophobicity, is higher than 90°, therefore it allows us to state that the treatment is adequate and satisfies the required requirements.

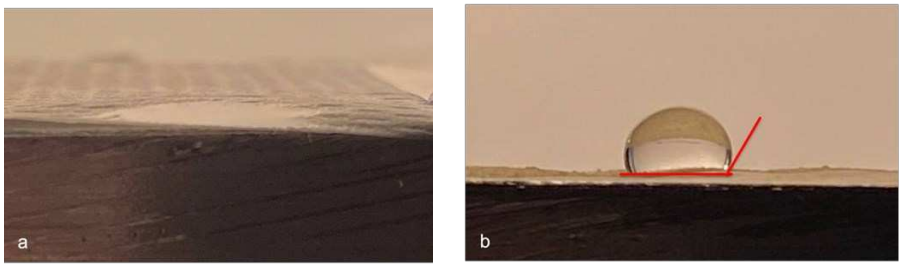

Figure 9- Contact angle measured on a) Whatman paper not treated and b) Whatman paper treated with CNC-PDMS

4.5- Mechanical properties

4.5.1- Tensile tests on Whatman paper samples

The goodness of the treatment in terms of consolidation of the paper support on which it was applied was evaluated using tensile tests. Figure 10 reports the tensile force per unit of width with respect to the percentage tensile deformation. It is important to note that paper samples are intrinsically anisotropic. The two directions of the sheet of Whatman paper must be defined: the longitudinal direction (MD) and the perpendicular direction (CD). CNC-CL, CNC-WP and CNCs-Ag sols have been chosen for Whatman paper samples treatments. For both directions, the tensile strength does not change with the CNC-CL, CNC-WP and CNCs-Ag treatments while the stretch increases up to 50 %. These results suggest that the treatment, with and without silver nanoparticles, improves the plastic properties of the paper which proves to be more extensible before breaking. It can be hypothesized that the high affinity between the chemical

structures of the CNC and the paper fibers is due to the hydrogen bonding interactions that are established[13]. As reported in table 5 the tensile energy absorption (TEA) represents the absorbing energy which considers tensile strength in relation to elongation and measures the toughness of the paper. The last parameter is increased by the CNC treatment, probably due to the transfer of stress between the inter- fiber in the material to the load of the CNC which in this way preserves the fiber-fiber bonds at higher tensile stresses[134]. For the not treated samples, the energy absorbed in MD is lower than in the CD. With the CNC treatments, the increase in TEA is recorded (60 %) for the longitudinal direction with respect to the tougher perpendicular direction.

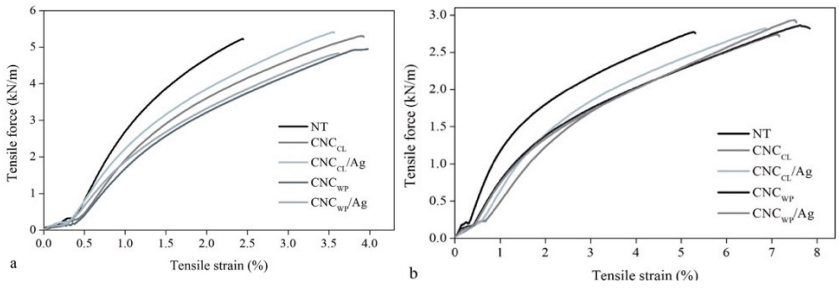

Figure 10- *Mechanical properties on perpendicular directions of the Whatman paper: a) MD; b) CD. Reproduced with permission from Ref.* [13]

The mechanical properties of Whatman paper samples treated with CNC-PDMS were compared with those of not treated paper (table 6). The two Whatman paper directions were evaluated. As evident from the data reported in table 6, the CNC-PDMS coating decreases the percentage elongation of fibers before the break, making samples stiffer in both directions.

Table 5- *Evaluation of mechanical properties on paper samples treated with CNCs. Standard deviation in parenthesis. Reproduced with permission from Ref.*[13]

Sample	Tensile strength (kN/m)	Tensile index (Nm/g)	Stretch (%)	Tensile energy adsorption (J/m^2)
NT (MD)	5.0 (2)	71.9	2.5 (2)	74 (4)
NT (CD)	2.8 (1)	40.8	5.4 (1)	109 (11)
CNC-CL (MD)	5.2 (3)	74.2	3.5 (4)	120 (6)
CNC-CL (CD)	2.8 (1)	40.3	7.6 (3)	136 (12)
CNC-WP (MD)	4.9 (1)	69.6	3.6 (5)	101 (14)
CNC-WP (CD)	2.8 (2)	40.7	7.8 (2)	140 (13)
CNC-CL/Ag (MD)	5.3 (3)	76.0	3.6 (3)	118 (22)
CNC-CL/Ag (CD)	2.8 (1)	39.8	7.1 (2)	130 (4)
CNC-WP/Ag (MD)	4.7 (1)	67.9	3.8 (2)	106 (10)
CNC-WP/Ag (CD)	2.9 (1)	40.8	8.1 (2)	145 (7)

Table 6- *Mechanical properties of Whatman paper samples treated and not treated. Standard deviation in parenthesis.*

Sample	Tensile strength (kN/m)	Stretch (%)	Tensile energy adsorption (J/m^2)
NT (CD)	3,9 (1,4)	3,1 (1,1)	77 (16)
NT (MD)	5,5 (0,3)	2,9 (0,7)	60 (20)
CNC-PDMS (CD)	3,8 (0,8)	2,3 (2,1)	58 (33)
CNC-PDMS (MD)	5,4 (0,5)	1,3 (0,4)	63 (15)

4.5.2- Tensile tests on canvas samples

The data on tensile strength (σ in MPa), stretch (ε in %) and TEA (MJ/m^3), for all samples before and after accelerated ageing are reported in table 7. Samples of TE set, treated with CNC, show values of σ, for both directions, higher respect to the samples treated with Aquazol, before accelerated ageing. Similarly, all samples in set GC-CNC have higher values (both σ and ε%) respect to samples in GC-NT and samples in GC-AQ, in both directions. In the set CO the samples treated with CNC show values comparable with not treated samples, but the tensile strength and TEA (only in MD) are better than the samples in GC-AQ. Respect to the untreated and treated with Aquazol, in the reference set, the tensile strength and ε% are higher for the CNC treatment, in CD. After accelerated ageing the differences between the two directions are the same: samples in CD show higher tensile strength values, while in the MD orientation a higher percentage elongation is observed. In the set TE, for not treated samples, the TEA values decrease for both directions. For the GC set the accelerate ageing doesn't influence the mechanical properties. As evident in table 7, all parameters investigated for the CO set, show good results for the CNC treatment. For the RIF set the TEA decrease in all samples. On the other hand, the CNC treatment gives higher tensile strength respect to the RIF-AQ (in MD) and the ε% is high in both directions.

Table 7- Comparison on mechanical properties on all canvas sets before and after the accelerated ageing. Standard deviation in parenthesis

Sample	Direction	σ(MPa) Before ageing	σ (MPa) After ageing	ε (%) Before ageing	ε (%) After ageing	TEA (MJ/m^3) Before ageing	TEA (MJ/m^3) After ageing
TE-NT	MD	29 (4)	16(2)	14 (1)	14(1)	1,6 (0,2)	0,5(0,1)
TE-NT	CD	30 (4)	22(3)	8 (1)	8(1)	1,0 (0,2)	0,5(0,1)
TE-CNC	MD	24(5)	16(2)	16(1)	14(1)	1,3(0,3)	0,6(0,1)
TE-CNC	CD	25(4)	22(3)	9(1)	10(1)	0,9(0,2)	0,6(0,1)
TE-AQ	MD	16(1)	12(1)	19(1)	15(1)	1,1(0,1)	0,4(0,1)
TE-AQ	CD	18(4)	16(2)	9(1)	8(1)	0,6(0,1)	0,4(0,1)
GC-NT	MD	17(4)	23(5)	7(1)	11(1)	0,7(0,2)	1,2(0,3)
GC-NT	CD	24(3)	32(5)	7(1)	6(1)	1,1(0,2)	1,1(0,3)
GC-CNC	MD	20(1)	21(2)	12(1)	11(2)	1,4(0,2)	1,1(0,2)
GC-CNC	CD	27(5)	27(4)	7(1)	6(1)	1,0(0,2)	0,9(0,2)
GC-AQ	MD	18(3)	22(1)	9(1)	9(1)	1,0(0,1)	1,1(0,1)
GC-AQ	CD	28(4)	40(6)	8(1)	7(1)	1,2(0,2)	1,4(0,2)
CO-NT	MD	20(2)	21(2)	10(2)	8(3)	1,1(0,2)	1,0(0,3)
CO-NT	CD	22(4)	29(6)	6(1)	6(1)	0,9(0,2)	0,9(0,1)
CO-CNC	MD	20(2)	25(3)	9(1)	9(2)	1,0(0,1)	1,2(0,3)
CO-CNC	CD	22(4)	32(5)	6(1)	6(1)	0,9(0,2)	1,0(0,3)
CO-AQ	MD	18(2)	21(4)	9(2)	10(3)	1,0(0,2)	1,1(0,3)
CO-AQ	CD	21(5)	32(9)	7(1)	6(1)	0,9(0,3)	1,1(0,3)
RIF-NT	MD	16(5)	-	13(3)	-	1,3(0,6)	-
RIF-NT	CD	23(1)	-	7(1)	-	1,0(0,1)	-
RIF-CNC	MD	15(5)	14(3)	12(3)	20(3)	1,2(0,5)	1,0(0,1)
RIF-CNC	CD	19(5)	17(2)	9(1)	10(3)	0,9(0,2)	0,7
RIF-AQ	MD	16(4)	14(2)	15(3)	14(1)	1,4(0,5)	1,1(0,2)
RIF-AQ	CD	18(3)	22(2)	6(2)	8(1)	0,7(0,2)	0,7(0,2)

4.6- Biocidal activity

Another important property to be evaluated in the event of a fungal attack is the ability of the applied treatment to develop a biocidal activity[122,135]. Here is reported the biocidal activity on *Aspergillus niger* that was verified on samples of Whatman paper treated with the CNCs, Ag nanoparticles and CNCs/Ag coatings. As reported in figure 11, the presence of the Ag nanoparticles prevents the growth of the fungus, on the contrary in the untreated and the CNC coated samples the growth of the fungus has not been prevented.

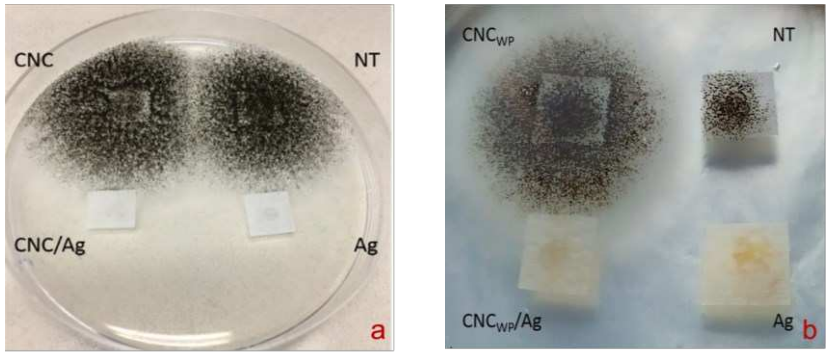

Figure 11- *a) Biocidal test on Whatman paper samples treated with silver nanoparticles, CNC-CL and CNC-CL/Ag; b) Whatman paper coated with Ag, CNC-WP/Ag and CNC-WP. In both experiments not treated samples (NT) are used such as control. Reproduced with permission from Ref.*[13]

5- Conclusions

CNC based treatments have been considered both on paper and on canvas samples, and their effectiveness has been compared with that of the well-known commercial consolidant Aquazol.

The FTIR spectra provided information on the interaction of consolidants with samples before and after artificial accelerated ageing. It is interesting to note that aged samples treated with CNC suspensions do not evidence peaks attributable to cellulose oxidation.

In the case of Whatman paper samples the CNC based treatment led to an improvement of the stretch and toughness of the cellulosic support. In the case of painting canvas mechanical tests have been performed before and after artificial ageing, showing promising results, compared with those obtained on non-treated canvas and on canvas treated with Aquazol. After accelerating ageing treatment, improvement on stretch have been observed on all CNC based treatment samples. CNC based coatings do not chromatically modify the surface, showing values lower than the perception of the human eye. Finally, the evaluation of the biocidal activity against *Aspergillus niger*, explored through the inhibition test, allows the CNC-Ag sol to be cataloged as a valid product against the fungal attack.

CHAPTER 3

CNC BASED HYDROGEL SCAFFOLDS

1- Abstract

In this chapter, two different matrices based on nanocellulose are proposed, one for medical applications and the other for environmental applications.

The first kind of matrix is a 3D printed hydrogel scaffold made of nanocellulose and alginate, mixed with silver nanoparticles to promote antimicrobial action [28,46,136,137]. The second is a three-dimensional hydrogel scaffold, made of carboxymethylcellulose mixed with nanocellulose, obtained by freeze-thaw method, for the removal of heavy metals in water [30,32].

The hydrogel scaffolds with a well-defined 3D structure have been builded following a method developed by Elviri et al [35]. The scaffolds were characterized by physico-chemical methods and by SEM-EDS to verify the morphology and the distribution of silver nanoparticles [13,33,34]. The mechanical properties were evaluated by measuring the elastic modulus. In addition, anti-microbial tests were carried out on *Staphylococcus aureus* and *Pseudomonas aeruginosa.*

Regarding the environmental field, carboxymethyl cellulose hydrogel scaffolds mixed with variously functionalized nanocellulose, have been prepared through the freeze-thaw method and are here proposed as non-toxic and biocompatible adsorbent materials for metal cations in water[138]. Carboxymethyl cellulose

(CMC) is a water-soluble anionic biopolymer derived from cellulose by partial substitution of hydroxyl groups with carboxymethyl groups. When dispersed in water, in the presence of metal ions it tends to form cross-linked gels. The addition of cellulose nanocrystals in the formulation contributes to the mechanical properties of the hydrogel. Different types of nanocellulose were added in the hydrogel scaffold formulation, to test the adsorption efficiency towards metal cations[139]. Hydrogel scaffolds have been characterized by physico-chemical methods and by SEM-EDS analysis. The removal efficiency of the hydrogel scaffolds towards Cu^{2+}, Co^{2+}, Ni^{2+} has been verified in aqueous solution by UV-Vis spectrophotometry[38,140,141].

2- Experimental

2.1- Materials

Sodium alginate (molecular weight 180–300 kDa), calcium chloride Copper acetate, Cobalt acetate and Nickel acetate were from Carlo Erba (Milan, Italy). Cellulose nanocrystals polymorphs I and II, oxidate CNC and silver nanoparticles were prepared as described in chapter 1. Sodium carboxymethylcellulose (CMC, molecular weight 10000 Da) was purchase by Nouryon Chemicals (Finland).

2.2- 3D printed Hydrogel Scaffolds

Formulations for 3D printing were prepared as described by Bergonzi[28]. Briefly: alginate (ALG) powders were dissolved at room temperature in ultrapure water to obtain a concentration of 5% w/v. A second dispersion was obtained using ALG (5% w/v) and CNC (3% w/v) in ultrapure water or in an aqueous suspension of silver nanoparticles. The Ag suspension was synthetized following the method reported in chapter 1, paragraph 2.9 at concentration of 100 ppm. The

formulations obtained were stored at 4 °C. For the scaffolds production with the 3D printer, the method reported by Bergonzi et al was followed[28]. Morphology consists of an orthogonal grid made of crossed filaments of about 100 µm, that compose square section channels of about 200 µm per side. The scaffolds are formed by 20 layers and have dimensions of 5 X 15 X 1 cm. An image of the hydrogel scaffold is reported in figure 1.

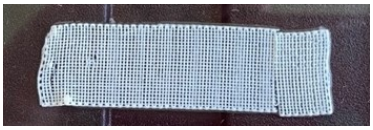

Figure 1- Image of a scaffold

2.3- Freeze-thawed Hydrogel scaffolds

To realize the hydrogel scaffold through freeze-thaw method, carboxymethyl cellulose (CMC) was used as starting material to form the hydrogel. The powder was dissolved in distilled water at room temperature to obtain a suspension with final concentration of 1% w/v. CNC, CNC II (polymorph II) or oxidated CNC (TOCNC) was added in 1:1, (w/w) ratio. Successively, 2ml of H_2SO_4 (1 M) were dropped into the mixture and it was kept stirred for 1h. The suspensions were cast in round plastic mold of 3 cm diameter. The material was subjected to 3 freeze-thaw (FT) cycles: it was frozen in a refrigerator at -17 °C for 8 h and successively thawed at room temperature for 3 h[44]. The hydrogel obtained was repeatedly washed in distilled water to remove the acid excess until neutral pH. All hydrogel scaffold formulations are reported in table 1.

Table 1- Description of hydrogel scaffold formulations

Sample	***Carboxymethyl cellulose (mg)***	***Cellulose (100 mg)***
C 1	100	Cellulose nanocrystals
C 2	100	Cellulose nanocrystals polymorph II
C 3	100	Oxidated Cellulose nanocrystals
C 4	100	-

2.3.1- Removal of water pollutant by adsorption process

2.3.1.1- UV-Vis Spectroscopy

The hydrogel scaffold adsorption capacity towards metal cations (Cu (II), Co (II) and Ni (II)) in solution at different concentrations (0,05, 0,025, 0,01 and 0,005 M for copper; 0,15, 0,1 and 0,05 M for cobalt and nickel) was evaluated by UV-vis spectroscopy[140,141]. The samples will be classified with a number relating to the type of scaffold (C1, C2, C3 and C4, as reported in table 1), followed by a letter relating to the concentration used for each experiment, as reported in table 2. The UV-Vis absorption measurement was carried out using the Perkin Elmer Lambda Bio 20 spectrophotometer. The Origin 8 program was used for processing spectra. To perform the test, 3 mL of metal solution were taken at pre-established time intervals, up to a maximum of 360 minutes.

Table 2- Classification of metal concentration used in the experiments

Copper concentration (M)	Reference letter
0,05	A
0,025	B
0,01	C
0,005	D
Cobalt and Nickel concentration (M)	**Reference letter**
0,15	A
0,1	B
0,05	C

Each aliquot was subjected to centrifugation and subsequently filtered with a syringe filter with a nylon membrane having a pore size of 0.45 μm. The metal ions concentration was estimated by absorbance measurements, according to the

Lambert Beer law[142], at the maximum absorption wavelength λ_{max} (765 nm for Cu (II), 513 nm for Co (II) and 394 nm for Ni (II)).

2.3.1.2 Adsorption and kinetics study

Adsorption is a mass transfer process involving the deposition of substances at the interface between two phases, such as solid - liquid interface[143]. The adsorbed substance is called "adsorbate" while the adsorbing material is called "adsorbent". The interaction between adsorbate and adsorbent can depend on various factors such as the presence or absence of surface charges, the porosity of the adsorbent and the pH of the solution[38]. The adsorption process, in a solid-liquid system, involves the removal of the solutes from the solution and their adsorption onto the solid surface. The adsorption (or removal) percentage (Ads (%)) can be determined by the following formula (1):

$$Ads\ \% = \frac{C_0 - C_e}{C_0}\ 100 \qquad (1)$$

where C_0 represents the initial concentration and C_e the concentration at equilibrium.

At equilibrium, the adsorption capacity, i.e. the amount of adsorbate that can be absorbed on the adsorbent surface, express as q_e in mg/g can be determined by the equation (2):

$$q_e = \frac{C_0 - C_e}{w}\ V \qquad (2)$$

where w (g) is the adsorbent weight and V (mL) is the adsorbate solution volume[144].

The adsorption kinetics were studied by fitting the experimental data to pseudo-first order (PFO) and pseudo-second order (PSO) kinetic models, described by the differential equations (3) and (4), respectively[145–148]:

$$\frac{dq_t}{dt} = k_1(q_e - q_t) \qquad (3)$$

$$\frac{dq_t}{dt} = k_2(q_e - q_t)^2 \qquad (4)$$

where q_t and q_e (mg g^{-1}) were the adsorption amounts adsorbate on the adsorbents at time t (min) and at equilibrium, respectively, and k_1 (min^{-1}) and k_2 (g/(mg min)) are the adsorption rate constants for PFO and PSO, respectively.

In the PFO, integrating equation (3) at the initial condition, t =0, $q_t = 0$ (5):

$$ln\frac{q_e}{q_e - q_t} = k_1 t \qquad (5)$$

where k_1 is the slope of the linear fit of $ln(q_e/(q_e - q))$ vs. t and indicates the speed with which equilibrium is reached[149].

For PSO[150,151], whit the initial condition t = 0, $q_t = 0$ integrating equation (4) and rearranging, the linearized form can be obtained:

$$\frac{t}{q_t} = \frac{1}{k_2 q_e^2} + \frac{t}{q_e} \qquad (6)$$

The rate constant can be estimated by a linear fit to t/q_t vs. t [152–154].

3- Characterization

3.1- Scanning electron microscopy (SEM)

The SEM-EDS investigation was performed to study the samples morphology and the distribution of heavy metals.

Jeol JSM 6400 Scanning Electron Microscope equipped with an Oxford In-instruments Link Analytical Si (Li) Energy Dispersive System detector (SEM-EDS) was to highlight the silver nanoparticles presence and the morphology of the 3D scaffolds before and after the adsorption experiments. The data analysis was performed using the "Inca" software. All samples were dried following the procedure described below. The samples were subjected to repeated washing in

ethanol to remove water. Critical Point Drying (Balserz Union, FL, USA) was used in conditions of 70 atm and 37 °C, to eliminate the ethanol. After being dried, sample pieces were cut out of the scaffolds to be able to analyze both surface area and cross section.

To investigate the morphology on the surface and in section of the hydrogels, the measurements were performed with Scanning Electron Microscopes FEI Nova NanoSEM^{TM}, with In-lens SE detector (TLD-SE) (High Vacuum e Low Vacuum). The microanalysis was obtained using X-EDS Bruker QUANTAX-200 detector Xflash 6, 10mm^2, 126eV. To eliminate the water content in the hydrogel, the samples were dried with an infrared lamp.

3.2 - Mechanical test

The tensile strength and the elongation were determined by mechanical test performed according to chapter 2 paragraph 3.5.

3.3- Biocidal activity

The antimicrobial activity of the 3D scaffold was tested against strains of *Staphylococcus aureus* (ATCC 25923) (Manassas, VA, USA) and *Pseudomonas aeruginosa* (ATCC 27853) (Manassas, VA, USA). The 3D scaffolds were prepared as disk of 6mm diameter, subsequently sterilized in EtOH (70% v/v), washed with water and stored at 4°C.

The diffusion disk method (or Kirby-Bauer technique) has been adopted and modified ad hoc to analyze 3D printed hydrogel scaffolds[155]. The scaffolds (15×15x1 mm^2), ALG and ALG/CNC AgNP-free scaffolds, as control, were cut as disk form with 6mm diameter, then sterilized in 70% v/v ethanol, washed and

stored at 4 °C. Scaffolds containing AgNPs at different concentration (from 1 to 100 ppm) were tested to define the MIC.

Bacterial strains were inoculated in Mueller Hinton broth at 37 °C for 1–2 hours. Subsequently, the scaffolds were placed inside petri dishes incubated at 37 °C for 18-24 hours. A positive control (a Petri dishes seeded with bacteria) and negative control (only scaffold) were also settled.

The antimicrobial activity is evaluated by the measurement of the diameter of the inhibition ring.

4- Results and discussion

4.1- 3D printed Hydrogel Scaffolds

4.1.1- Scanning electron microscopy (SEM)

The morphology of 3D printed hydrogel scaffolds is characterized by a well-defined geometry: the filament of about 100-150 µm form a uniform lattice with sides of about 200 µm (figure 2A and 2C). The silver nanoparticles, when introduced in the formulation, are homogeneously distributed into the scaffold matrix, and no agglomeration of nanoparticles is visible (figure 2E and 2F).

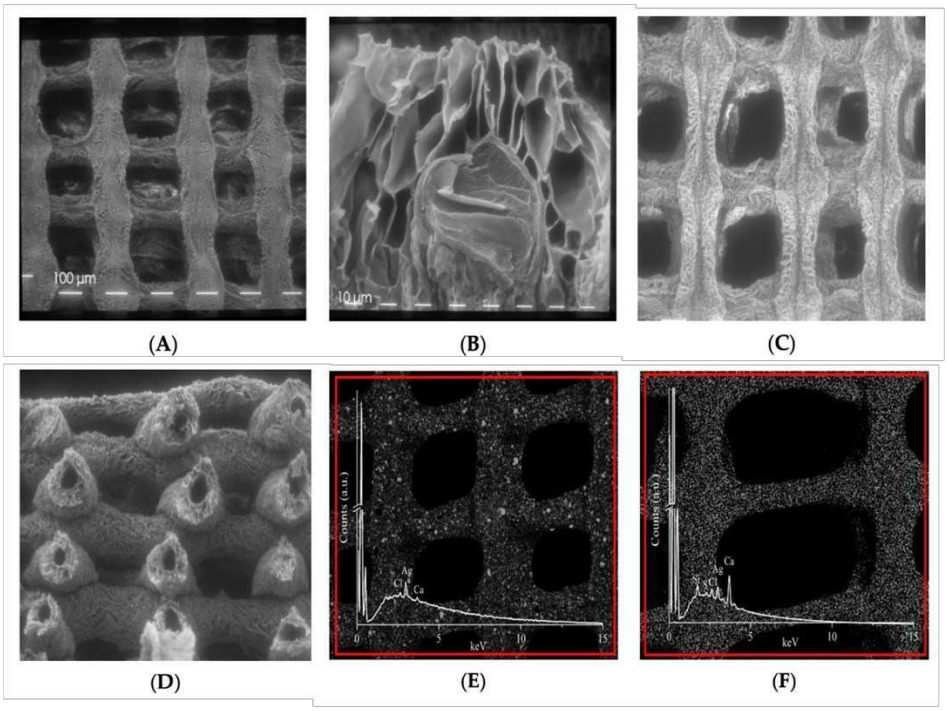

Figure 2- SEM images acquired on A) scaffold alginate at magnification 80X; B) scaffold alginate at magnification 360X; C) scaffold alginate-CNC based at 80X; D) cross-section of alginate-CNC scaffold (80X); E) EDS map and EDS spectrum of silver nanoparticles in alginate scaffold (80X); F) EDS map and EDS spectrum of silver nanoparticles in alginate-CNC scaffold (80X). Reproduced with permission from Ref.[28]

The SEM image of a cross section of the alginate scaffold (figure 2B) shows a regular structure of the interconnected and stratified pores (diameter in the range 11÷ 45 μm). The scaffold made of alginate-CNC mix (figure 2D) shows hollow tubular fibers with diameter in the range between 11÷ 126 μm.

4.1.2- Mechanical test

The mechanical properties of the scaffolds without the addition of silver nanoparticles were evaluated by means of tensile tests. In the alginate-based scaffold sample, the tensile strength is 5.4 N, while in the case of ALG/CNC based-scaffold it is slightly lower, around 3.6 N (fig. 3a). The same trend can be observed for the elasticity: in samples with CNC a value of 0.3 MPa is recorded which is slightly lower, compared to 0.4 MPa referred to samples with alginate only (fig 3b). Nevertheless, the scaffolds show sufficient mechanical properties that allow their utilization.

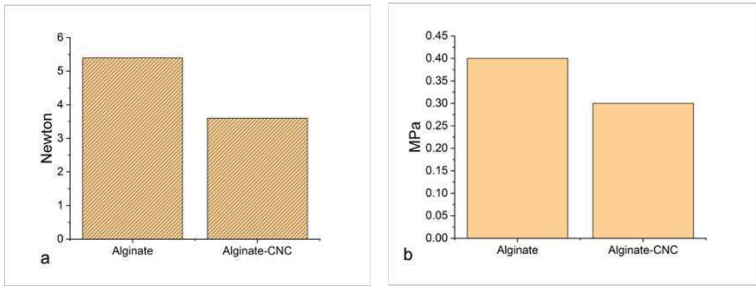

Figure 3- a) Tensile strength (N) on alginate and alginate-CNC scaffolds; b) Elasticity (MPa) on alginate and alginate-CNC scaffolds

4.1.3- Biocidal activity

The antimicrobial activity against *P. aeruginosa* and *S. aureus* (fig. 4a-b) was evaluated following the procedure described in the experimental part. Scaffolds based on alginate, alginate-CNC and alginate-CNC-Ag were tested. In the last formulation, different concentrations of the colloidal solution of silver nanoparticles (1, 5, 10, 100 ppm) were tested to determine the minimum

concentration necessary to inhibit the growth of the bacterial strains tested. Satisfactory results were obtained for the formulations containing 100 ppm and 10 ppm of silver, with an inhibition ring diameter of 6 mm for all experiments. No inhibition was recorded below this concentration. The MIC at 10 ppm is then defined for both bacterial cultures. As specified in the experimental part, the antimicrobial activity was also tested on scaffolds without silver nanoparticles (alginate and alginate-CNC). In this case, no inhibition activity is recorded.

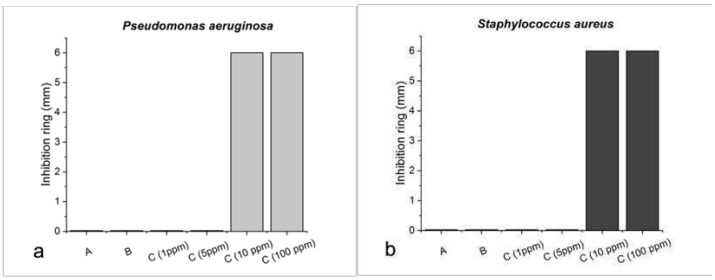

Figure 4- Antimicrobial test on a) P. aeruginosa and b) on S. aureus. A: Alginate; B: Alginate-CNC; C: Alginate-CNC-Ag scaffolds (in parentheses the Ag concentration)

4.2- Freeze-thawed Hydrogel scaffolds

4.2.1- Scanning electron microscopy (SEM)

The freeze-thawed hydrogel scaffold samples were analyzed with SEM. The hydrogels used for the adsorption experiments towards cobalt are not investigated because the sample preparation was not possible. In figure 5 a-c the SEM images of the powders used for the hydrogel formation are reported: cellulose nanocrystals, carboxymethylcellulose and their mix in 1:1 w/w ratio. The grains of CNC powder have a spherical shape with diameter dimensions within the range 1 ÷ 25 μm, this signifies that nanocrystals tend to agglomerate and form rounded grains when dried or in form of powder. The CMC powder shows elongated rods shape of different lengths ranging from a few tens of microns to 200 μm. In figure 5c are clearly visible the presence of two powders.

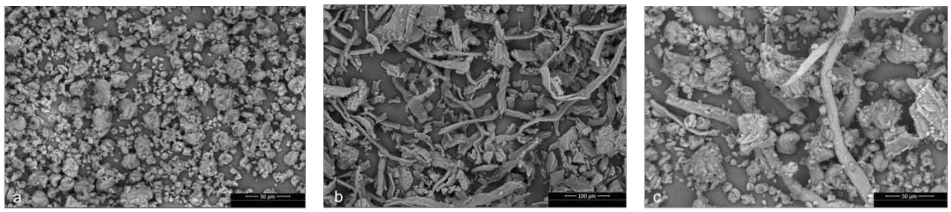

Figure 5- SEM images of a) cellulose nanocrystals powder, b) carboxymethylcellulose powder and c) CNC:CMC powder (ratio 1:1 w/w)

The SEM image of C1 sample (figure 6 a) shows a 3D structure with layers and pores with different diameter dimensions (100-300mm). In figure 6b is reported the EDS elemental map acquired on the area in the yellow box in figure 6a. The presence of sulfur is due to the sulphate group present on the cellulose nanocrystals, due to the acid hydrolysis. The presence of Au is due to the metallization process of the sample.

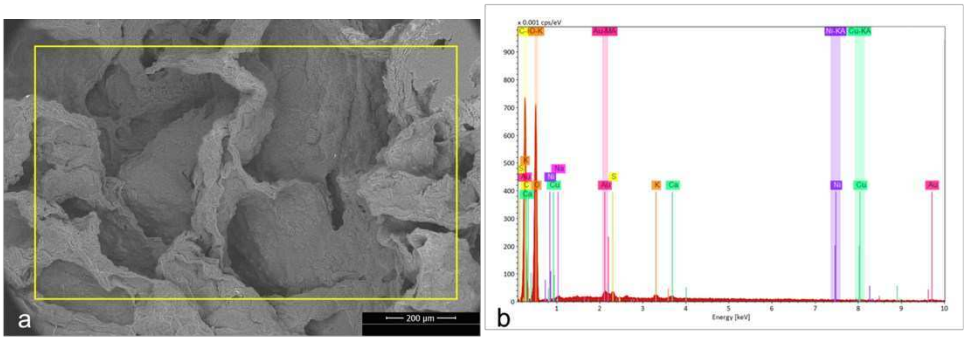

Figure 6- a) SEM image on C1 sample; b) EDS map on the yellow box in a)

Figure 7a and 7b show the morphological aspect of hydrogel sample C1 after immersion in the highest and lowest copper concentrations (sample C1A and C1D) respectively, analyzed to verify if the metal concentration influences the structure. The 3D structure of the scaffold after copper adsorption seems to be more compact than before the adsorption. The scaffold containing oxidated CNC is characterized by large cavities. The scaffold made of nanocellulose polymorph II shows more compact regions, probably due to the tangled structure of CNC

polymorph II. Figure 8a-d shows the EDS spectra acquired on the total area of figure 7a-d. The signal of Cu is evident in all spectra with comparable intensity.

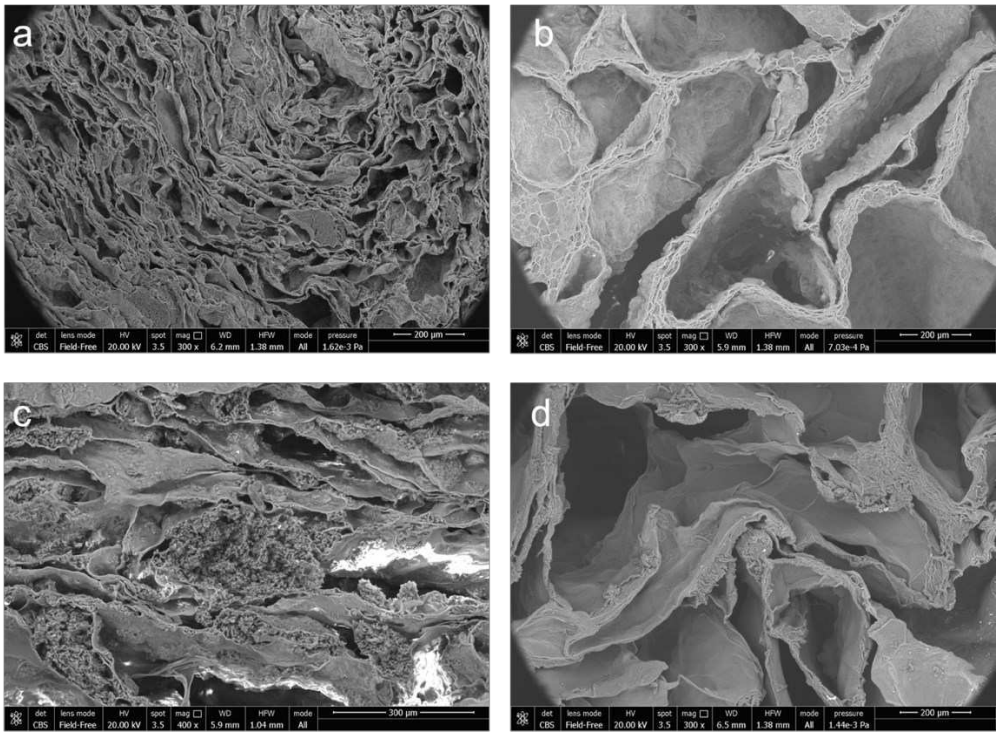

Figure 7- SEM images on a) C1A, b) C1D; c) C2D and d) C3D tested with copper

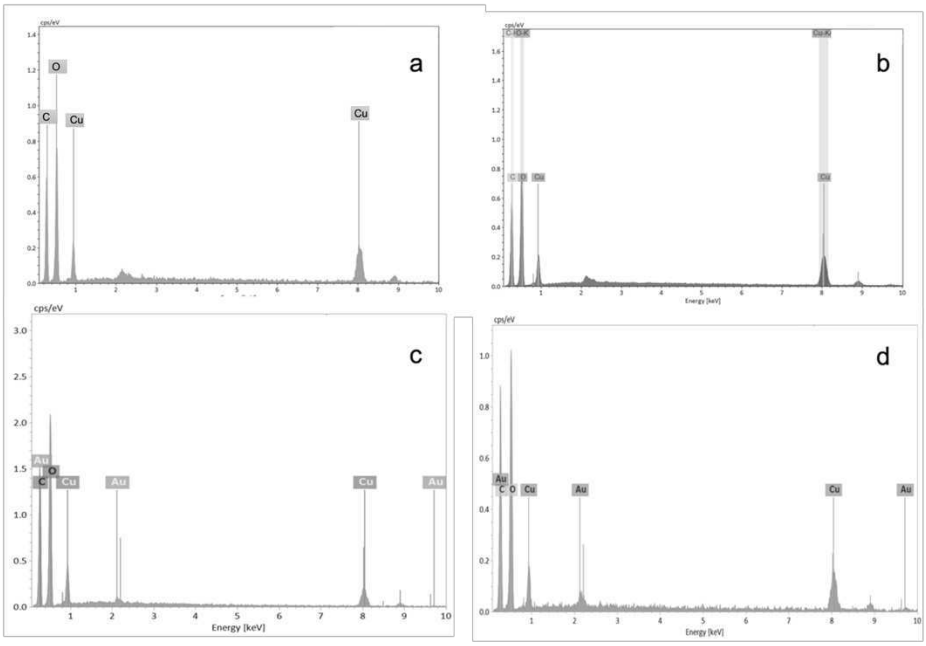

Figure 8- EDS spectra acquired on images in figures 7a) C1A sample, 7b) C1D sample; 7c) C2D sample and 7d) C3D sample tested with copper

Figure 9a-c shows SEM images acquired on samples after adsorption of Nickel ions. The morphology of the samples is characterized by wide cavities. The EDS map and spectrum, acquired on the area in the yellow box in figure 9a, highlight the presence of the nickel and its homogeneous distribution.

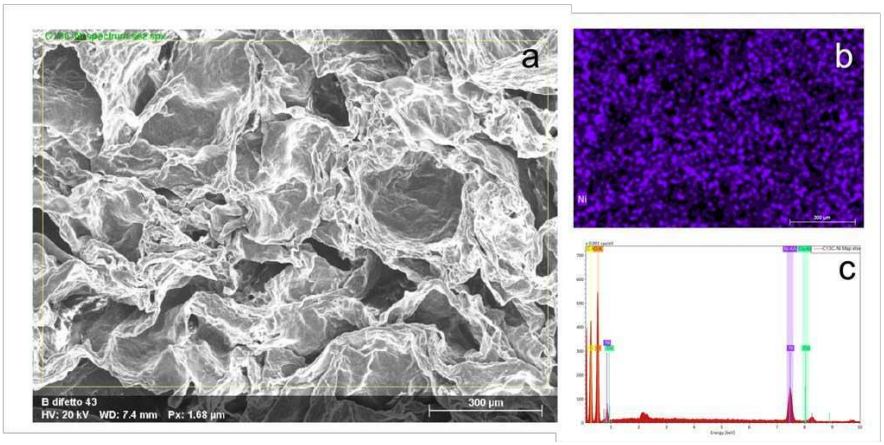

Figure 9- a) SEM image on C1C section tested with nickel; b) EDS map acquired on the yellow box in figure 9a and c) EDS spectrum

4.2.2- Metal ions adsorption studies

To define the adsorption percentage and the uptake for all hydrogel scaffolds tested versus metal solutions, were applied the formulas (1) and (2) reported in this chapter, paragraph 2.3.1.2. In tables 3-5 are summarized the results obtained after 360 min of adsorption experiments. In figure 10 are reported the hydrogel scaffold before (figure 10a) and after (figure 10b-d) metal ions removal. For a predetermined amount of adsorbent, at low initial concentrations of metal ions, there are many active sites on the surface: adsorption is rapid and equilibrium is rapidly reached. On the contrary, at high initial concentrations of metal ions, the adsorbent surface is progressively occupied. This causes a decrease of available active sites and slows down the rate of absorption [153,156].

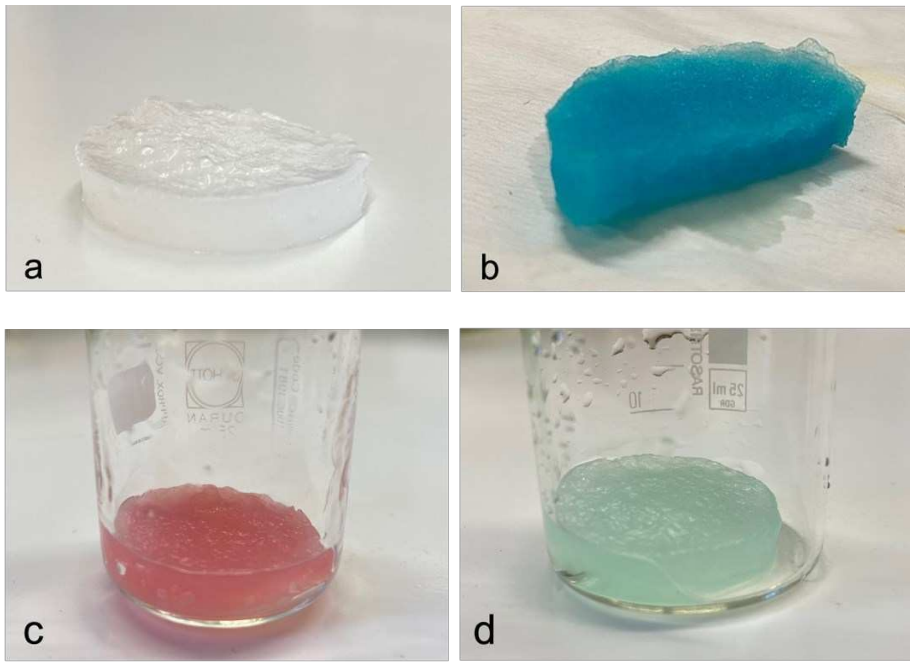

Figure 10- a) hydrogel scaffold before metal adsorption; b) Copper adsorption on C1A sample; c) Cobalt adsorption on C1A sample; d) Nickel adsorption on C1A sample

The *Ads %* values reported in table 3 show the same trend for all scaffolds set tested. In detail only the C2 set shows a relatively low adsorbent capacity (*Ads %*). For the C1 material, a maximum adsorption of 77% is recorded for sample C1D. For C4, in which the samples consist only of CMC, lower adsorption percentages are obtained. This demonstrates that the non-functionalized CNC, embedded in the carboxymethylcellulose matrix, improves the adsorption capacity of the scaffold. Interestingly, the C3 material has an adsorption rate higher than 80%. Probably the negative surface charges present on the oxidized cellulose nanocrystals have a better interaction with the metal[149]. The behavior of the hydrogel scaffolds studied shows satisfactory adsorption capacities especially at low copper concentrations.

Table 3- Adsorption capacity and adsorption percentage for hydrogel scaffold tested (1, 2, 3 and 4) with copper at different concentration (A, B, C and D). Standard deviation in parentheses. K2 are calculated experimentally [152]

Sample	Concentration	q_e (mg/g)	*Ads %*	r^2	K_2
C1A	0,05	0,57 (3)	24,5 (2)	0,981	0,03
C1B	0,025	0,33 (4)	30,6 (3)	0,991	0,2
C1C	0,01	0,17 (2)	50,6 (5)	0,985	0,24
C1D	0,005	0,1 (1)	**77,3 (4)**	0,981	0,48
C2A	0,05	0,47 (4)	19,9 (3)	0,989	0,06
C2B	0,025	0,34 (2)	31,06 (8)	0,989	0,12
C2C	0,01	0,12 (5)	36,3 (5)	0,981	0,34
C2D	0,005	0,06 (2)	**46,1 (9)**	0,997	1,25
C3A	0,05	0,57 (3)	24,5 (5)	0,993	0,1
C3B	0,025	0,47 (3)	43,7 (4)	0,997	0,1
C3C	0,01	0,26 (4)	71,9 (2)	0,987	0,1
C3D	0,005	0,14 (2)	**82,3 (4)**	0,997	0,85
C4A	0,05	1,03 (2)	21,9 (3)	0,997	0,07
C4B	0,025	0,63 (5)	29,1 (4)	0,996	0,08
C4C	0,01	0,35 (4)	47,5 (2)	0,996	0,14
C4D	0,005	0,23 (3)	**65,6 (3)**	0,982	0,19

Treatment of the adsorption kinetics data were carried out by fitting the experimental data to both pseudo-first order (PFO) and pseudo-second order (PSO) models, as described in the experimental section. The adsorption kinetics of all metal ions adsorbed on the scaffolds fit well with the pseudo-second order model with respect of the calculated active sites on the adsorbent ($r^2 \geq 0.98$). Figures 11 a-d compare the different hydrogels scaffolds exposed to contact with the metal solution at the same concentration (a 0.05 M, b 0.025 M, c 0.01 and d 0.005 M). The plots are obtained by fitting the experimental data through equation (6) t/q_t vs. t for the pseudo-second order. As reported in literature[29,38], the adsorption rate in PSO model is proportional to the initial concentration of the adsorbed species and to the square of the number of empty sites.

Further experiments aimed at investigating the mechanism of adsorption were not carried out since they did not fit into the immediate scope of this work. It will be however interesting to investigate in the future the origin of this order of reaction, and if different mechanisms take place at different metal concentration or after a partial loading of the material.

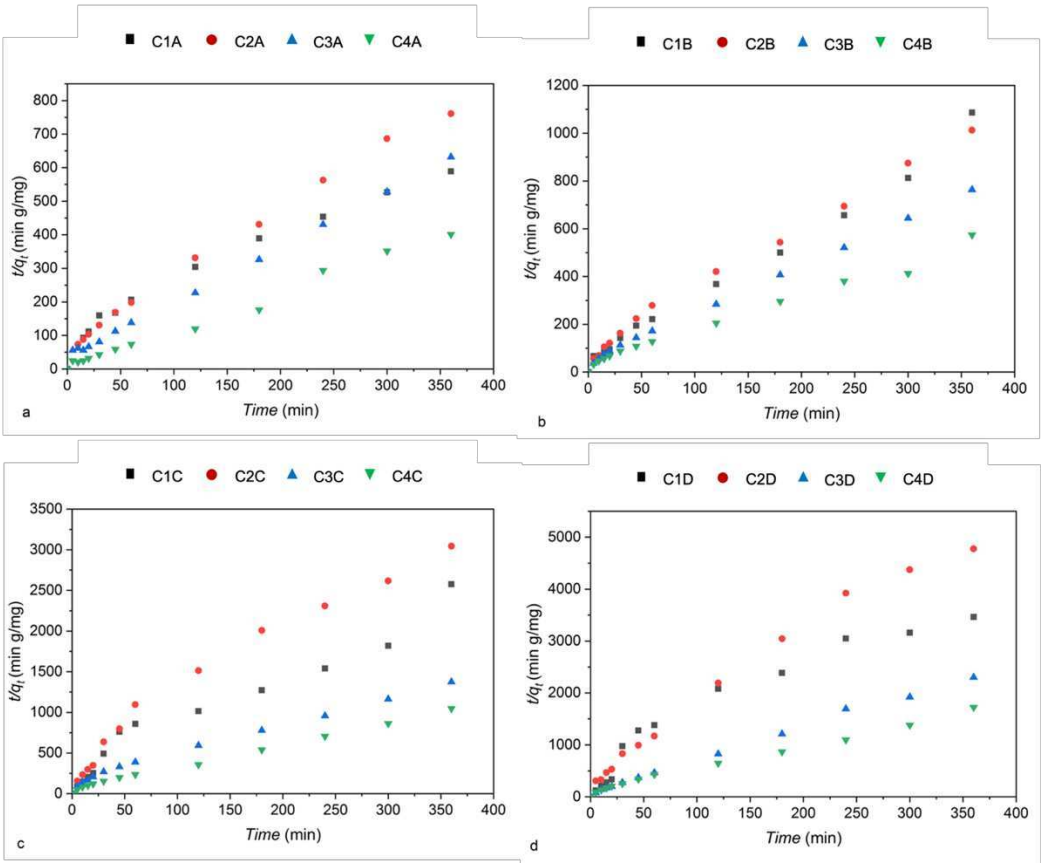

Figure 11- PSO fitted on t/q_t vs. t. Comparison of all hydrogel scaffolds with different copper concentrations: a) 0,05 M, b) 0,025 M, c) 0,01 M and d) 0,005 M. Labels of the hydrogel samples are explicated in table 3.

As reported in tables 4 and 5, for the other two metals tested, the *Ads%* are lower respect to the adsorption capacity recorded for copper. The highest percentage of adsorption for cobalt is 20% at the initial concentration of 0.15 M (C2 and C3 scaffolds). In the case of nickel, it is noted that when the concentration of the metal decreases, the adsorption percentage increases from 13 % to 26%. Using functionalized CNC, a higher efficiency than CMC alone or mixed CMC with non-functionalized CNC was observed. For the studies carried out with cobalt, low q_e values are recorded, compared to those obtained in the experimentation with nickel.

The Ads% values are higher for Cu(II), followed by those of Ni(II) which are close to those of Co(II) (in general the lowest for the latter ion). This trend seems to follow, perhaps expectedly, the Irving-Williams series of the divalent cations[157,158]. The Irving-Williams series is an empirical relationship between the formation constants of the complexes of the cations of the first row of the transition d-block in their +2 oxidation states. Given a specific ligand, the Irving-Williams series predicts that the order of stability of the complexes with the same stoichiometry is Mn(II) < Fe(II) < Co(II) < Ni(II) < Cu(II) > Zn(II). In terms of the series, Cu(II) is indeed predicted to form the most stable complexes, which likely is at the origin of the much higher Ads% compared with those of the other two cations. As for Ni(II) and Co(II), the Ads% seems to cope with the Irving-Williams series, however with peculiar trends within the data collected for the same materials. We put forward the hypothesis that the different preference of the cations for the donor atoms in the material (Ni(II) softer than Co(II)) and the preference for different coordination numbers may be at the origin of the observed trends of the values reported in the tables.

As for the kinetics of uptake (figure 12) for all scaffolds tested, fit well with PSO, as in the copper case study.

Table 4- Adsorption capacity and adsorption percentage for different hydrogel tested (1,2,3 and 4) with cobalt at different concentration (A, B and C). Standard deviation in parentheses. K2 are calculated experimentally[152].

Sample	Cobalt Concentration	q_e (mg/g)	*Ads %*	r^2	K_2
C1A	0,15	0,08 (2)	**20,3 (3)**	0,997	1,03
C1B	0,1	0,03 (1)	9,6 (2)	0,995	1,6
C1C	0,05	0,06 (2)	12,1 (2)	0,993	3,3
C2A	0,15	0,09 (3)	**23 (2)**	0,997	0,64
C2B	0,1	0,019 (2)	7,8 (3)	0,996	2,9
C2C	0,05	0,007 (4)	6,5 (5)	0,992	4,02
C3A	0,15	0,09 (3)	**22,5 (3)**	0,997	0,76
C3B	0,1	0,03 (2)	10 (2)	0,998	9,25
C3C	0,05	0,013 (3)	11 (3)	0,998	10,78
C4A	0,15	0,18 (3)	22,7 (1)	0,998	0,5
C4B	0,1	0,03 (2)	5,6 (4)	0,992	1,85
C4C	0,05	0,06 (3)	**26,3 (3)**	0,993	25,6

Table 5- Adsorption capacity and adsorption percentage for different hydrogel tested (1, 2, 3 and 4) with nickel at different concentration (A, B and C). Standard deviation in parentheses. K2 are calculated experimentally.

Sample	Nickel Concentration	q_e (mg/g)	*Ads%*	r^2	K_2
C1A	0,15	1,52 (4)	13 (2)	0,997	0,04
C1B	0,1	0,63 (2)	13,6 (3)	0,99	3,5
C1C	0,05	0,58 (3)	**17,2 (3)**	0,998	1,23
C2A	0,15	1,77 (4)	15,5 (3)	0,996	0,07
C2B	0,1	0,88 (5)	14,3 (4)	0,991	0,08
C2C	0,05	0,61 (3)	**18,3 (6)**	0,995	0,2
C3A	0,15	1,24 (4)	13,1 (5)	0,996	0,09
C3B	0,1	0,61 (6)	16,3 (3)	0,988	0,016
C3C	0,05	0,48 (4)	**26,1 (5)**	0,998	0,26
C4A	0,15	3,98 (2)	8,3 (2)	0,995	0,03
C4B	0,1	1,03 (2)	16,5 (4)	0,998	0,2
C4C	0,05	1,0 (2)	**20,9 (3)**	0,996	0,06

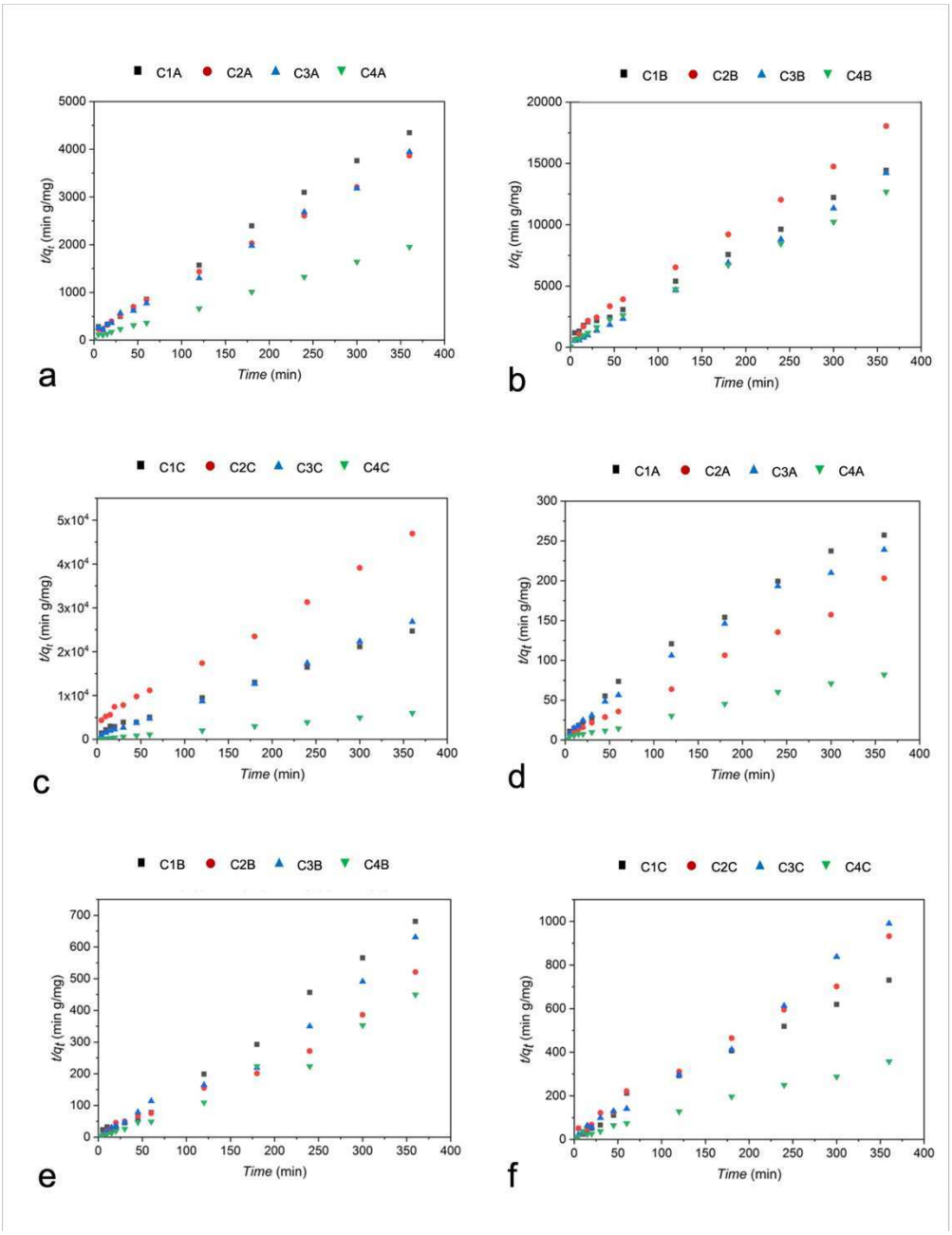

Figure 12- PSO fitted on t/q_t vs. t. Comparison of all scaffolds with different cobalt (a-c) and nickel (d-f) concentrations. Labels of the hydrogel samples are explicated in table 4 and table 5.

5- Conclusions

In this chapter three-dimensional hydrogel scaffolds have been prepared using nanocellulose as starting and active material. A 3D printing technology and freeze-thaw method was used depending on the mixture of biopolymer used. The surface morphology of the scaffolds was studied with SEM investigation which allowed to note the homogeneity of distribution of the elements, the absence of aggregates and pores on the surface. The activity of the silver nanoparticles, inserted in the formulation by 3D printing technology towards *Pseudomonas aeruginosa* and Staphylococcus aureus was evaluated.

A traditional freeze-thaw method of obtaining three dimensional hydrogels scaffolds of carboxymethyl cellulose was investigated. In this case the aim was to evaluate the best efficacy of different kinds of nanocellulose, in terms of removal of the metallic pollutant present in the aqueous solution. Thanks to the experiments that were set up in this study, it was possible to define the amount of metal removed (*Ads%*), the adsorption capacity (q_e) and the type of kinetics. The best results were obtained for copper tests: at low metal concentration was recorded high adsorption capacity. The tests with nickel show the same trend, observed at lower percentages of metal. The experiment carried out with cobalt showed better adsorption percentage of the scaffolds at high metal concentration. Finally, the adsorption kinetics studies were carried out through the linear fit of the experimental data to pseudo-second order kinetic model.

Overall our results seems to demonstrate that the materials are good adsorbents for Cu(II). As for Ni(II) and Co(II), interesting data were obtained in terms of adsorption capacities and features when evaluated at different metal concentrations. However, no real high uptake properties or selectivity were observed for either metal, highlighting that further optimization of the cellulose materials are advisable to achieve these performances, if desirable.

PART II

GEOPOLYMER FORMULATIONS FOR SUSTAINABLE BUILDINGS

The second part concerns the development of Geopolymer materials for sustainable building. This research is included in the PON project "Ricerca e Sviluppo di nuovi materiali avanzati per costruzioni eco-sostenibili, con caratteristiche di elevata efficienza energetica e sicurezza anti sismica, da ottenersi con sistemi avanzati di produzione ad alte prestazioni, efficienti ed ecocompatibili" Programma Operativo Nazionale «Imprese e Competitività» 2014- 2020 FESR numero F/090017/00/X36, CUP B18l17000450008.

The work is divided into three parts:

- Development of the geopolymer binder with solid alkali activators.
- Development of geopolymer-based mortar and plaster.
- Final formulations and characterization of the products.

Introduction

The fight against pollution reduction and climate change is a topic of particular importance at global level. The building sector represents one of the most significant sources of pollution: approximately 7% of global CO_2 emissions are

attributable to the production and manufacturing of Portland cement. The need therefore arises to develop materials that represent an eco-sustainable alternative. In recent years alkaline activated materials, such as geopolymers, have been extensively investigated as a possible substitute to conventional cement[159–164]. Geopolymers are a class of “artificial” inorganic three-dimensional polymers obtained by polycondensation reaction of aluminosilicate at low calcium content with alkalis. The aluminosilicate starting sources can be of natural origin such as clays, feldspars, volcanic ashes, pozzolans or of industrial origin such as blast furnace slags, fly ash etc[165–167]. The alkali activators are hydroxides and silicates of alkali metals The term "geopolymer" was coined for the first time by Davidovits[168] in 1978: "geo" indicates that these materials mimic materials of a geological nature (i.e. phyllosilicates); "polymer" indicates that these materials are obtained from the polymerization of repeating units of oligomers $-\{(Si\text{-}O)_m\text{-}Al\text{-}O\text{-}\}_n$ just like the polymers. After the addition of alkali activators, following the raw materials dissolution, new chemical bonds are formed during the geopolymerization process which lead to obtain an amorphous or semicrystalline material with properties comparable to those of inorganic materials, such as hardness, chemical stability, high thermal stability (> 1200 °C) and mechanical properties that make these materials suitable for various applications: matrices for refractory and flame retardant composites, structural and porous building materials, matrices for the inerting of toxic and radioactive wastes, mortars for restoration and more[169–172].

In the geopolymerization process the alkaline solution plays a fundamental role allowing the dissolution of the aluminosilicates of the starting material, the hydrolysis of the Al^{3+} and Si^{4+} compounds and the polycondensation of the hydroxy-aluminate and hydroxy-silicate species[173–175]. The geopolymerization process can be divided into three stages (figure 1): (i) dissolution/hydrolysis, (ii) polycondensation, (iii) solidification/crystallization. (i) The alkaline activating

solution, through the consumption of water and thanks to the action of the hydroxyl groups, promotes the dissolution of the alumino-silicate network leading to the formation of aluminate and silicate monomers[175].

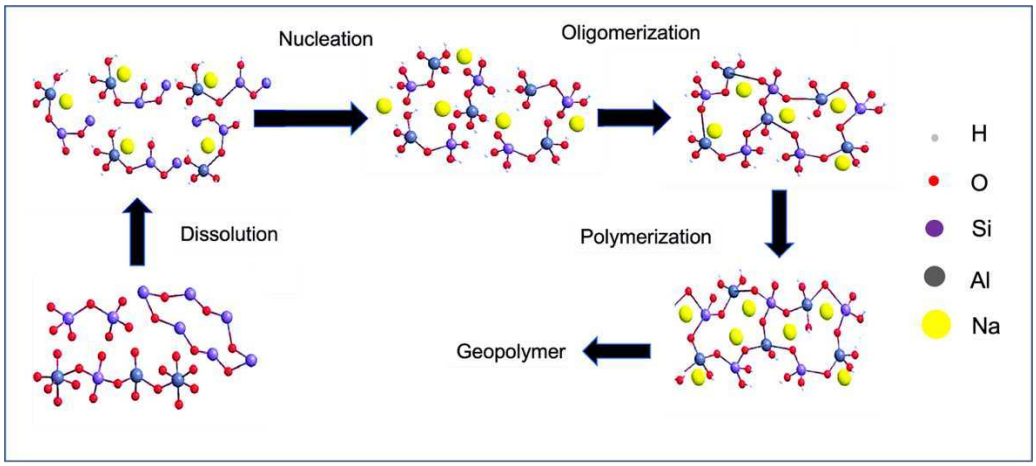

Figure 1- Possible reaction scheme of geopolymerization

The monomers form a complex mixture of aluminates, silicates and aluminosilicates in equilibrium which condenses leading to the appearance of the first oligomers with the formation of a disordered gel. The gel appears as a two-phase mixture: aluminosilicates and water, which fills the space between the particles without reacting. (iii) Finally, there is a rearrangement of the polymer gel which evolves into a three-dimensional network by increasing the connections between the chains. The resulting polymerization leads to the hardening of the whole system.

1- Abstract

The research activity was focused on the study of innovative eco-compatible geopolymer mortars and plasters. Geopolymeric binders belong to the class of alkaline activated materials and are obtained by policondensation reaction of

natural aluminosilicates (such as metakaolinite) or industrial wastes (such as silica fumed and slag) with an alkaline solution. The present research mainly focuses on the possibility of replacing the liquid alkaline activator[176,177] with a solid alkaline activator. The obtained “one-part” premix can be easily used in real situations[161,178,179]. In “one-part” component, the dissolution of the alkali activator starts after water addition, therefore a complete reaction with a solid source of aluminosilicate may takes longer than using alkali activator in solution15–17,in the so called "two-part” reaction. For the development of binders, mortars and plasters, parameters such as workability (consistency, plasticity and cohesion) must be considered[180,181]. One-part binders were investigated: the powder precursors were varied to evaluate the product with best performance. After choosing the binder, mortars and plasters were developed. Then, for both materials, several formulations were proposed. Particular attention has also been paid to the use of various natural additives, such as starch and cellulose, due to their adhesive properties and rheological modifiers, respectively, which influence the properties of the fresh and hardened mortar: as the type and quantity of additives vary, workability, adhesion to the substrate and mechanical resistance were evaluated. Finally, mortars and plasters were applied on autoclaved aerated concrete blocks: the correction time and the adherence were evaluated.

All products were fully characterized, to assess the chemical, physical and mechanical properties.

2- Experimental

2.1- Materials

Metakaolinite (BASF), hydrated sodium silicate (Britesil C205 pH 11.5 - Crossfield), potassium silicate 205K (Tillmans S.P.A.), calcium hydroxide

(Unicalce), blast furnace slag (Neuvendis), white cement 52.5 (CB, Italcementi). Additives: maize starch was purchased in the local market, methyl cellulose (Culminal 15000 high viscosity HV, Culminal 8367 medium viscosity MV, and Culminal 6000 low viscosity LV), and silopon 8010 (air entraining agent) were purchased by Ashland, Dehscofix (plasticizer, water reducing agent) was provided by Neuvendis, Starvis S35F (water reservoir) and Dynamon SR4 (superplsticizer) was puechased by BASF, expanded glass (PV) was purchased by PORAVER, basalt fibers, silica sand 505 e 510 were provided by Bacchi s.p.a.

2.2- Binder formulations for the development of mortar

To evaluate the performance of the new "one-pot" geopolymers with respect of the two-part classical geopolymer, a formulation with alkali activator solution was prepared. Briefly: metakaolinite (MK) and alkali activator solution (AAS) in a 3/1 ratio are mixed for 5 minutes in a mechanical mixer, with a water/binder ratio (w/b) = 0.6. The activating solution consists of sodium hydroxide (6M) and sodium silicate in the ratio 4/1 (w/w). The sample was called **L1**.

The "one-pot" binders, called from ***L2*** to ***L5*** were obtained by mixing metakaolin and alkali activator in powder form (AAP) in the ratio of 2.5/1 (w/w). The alkaline activator and w/b are different in the various formulations:

L2 – sodium silicate/calcium hydroxide=1/7; w/b = 0.86

L3 – sodium silicate /calcium oxide = 1/5; w/b = 0.91

L4 – potassium silicate/ calcium hydroxide =1/6; w/b = 0.93

L5 – potassium silicate / calcium oxide = 1/5; w/b = 0.93

2.3- Binder formulation for the development of plaster

Different formulations have been investigated to obtain a suitable binder for the development of plaster. In these formulations, metakaolin was substituted with blast furnace slag (BFS) wastes. The different formulations are listed below. The percentage of BFS and alkali activator in powder form (AAP) indicated in the description, refers to the total solid mass of binder. The formulations are named from ***LP1*** to ***LP7***:

LP1 - BFS 80.4 %; AAP (Na_2SiO_3, KOH, $CaCO_3$) 19.6 %; w/b = 0.43

LP2 -BFS 92 %; AAP (Na_2SiO_3, $Ca(OH)_2$, $CaCO_3$)8%; w/b = 0.53

LP3 - BFS 91.9 %; AAP (Na_2CO_3, $Ca(OH)_2$) 8.1%; w/b = 0.51

LP4 - BFS 91.9 %; AAP (Na_2SiO_3, $Ca(OH)_2$) 8.1%; w/b = 0.44

LP5 - BFS 80.4 %; AAP (Na_2SiO_3, KOH, $CaCO_3$) 19.6%; w/b = 0.43

LP6 - BFS 80%; AAP (Na_2SiO_3, $Ca(OH)_2$, $CaCO_3$) 20%; w/b = 0.30

LP7 - BFS 86.3 %; AAP (Na_2SiO_3, $Ca(OH)_2$, $NaHCO_3$) 13.7 %. w/b = 0.69

2.4- Formulations for the development of mortar

Following the results obtained on the different binder formulations (from ***L1*** to ***L4***), which will be reported in the results and discussion, paragraph 3.1, the ***L4*** binder (calcium hydroxide and potassium silicate) was chosen for the development of the mortar. The mortars were prepared by adding sand, in a binder/sand ratio of 1/3 or 1/2 (w/w), and different natural additives to the binder. Table 1 summarized the mortars formulations prepared.

The final mortars were named ***M1*** to ***M8***.

Table 1- Description of mortar formulations. The additives percentage (%) is referred to the total solid mass of the mortar. The w/b ratio is calculated on the mass of binder.

Sample	w/b ratio	Additives (%)
M1	0.91, 0.93, 1.1	-
M2	1	Alginate (0.25%)
M3	0.97	Rice Starch (3%)
M4	1.1	Maize Starch (0.5%)
M5	1.1	Maize Starch (0.5%), Culminal 8367 MV (0.3%)
M6	1.1	Maize Starch (0.5%), Culminal 8367 HV (0.3%), Dynamon SR4 (0.05%)
M7	1.1	Maize Starch (0.5%), microfibrillated cellulose CMF (0.3%), Dynamon SR4 (0.05%)
M8	1.1	Maize Starch (0.5%), nanocrystalline cellulose CNC (0.3%), Dynamon SR4 (0.05%)

2.5- Formulations for the development of plaster

Following the results obtained on the different formulations of binder (from ***LP1*** to ***LP7***), which will be reported in the results and discussion, paragraph 4.2, the ***LP2*** binder (AAP: Na_2SiO_3, $Ca(OH)_2$, $CaCO_3$) was chosen for the development of plaster. For the formulation of the plaster, the binder was mixed with the aggregates (silica sand (S_{510}), expanded glass (PV 0.5-1 mm)) and different additives (methyl cellulose $Culminal_{8637}$ and $Culminal_{15000}$, $Silopon_{8010}$, Starvis, Dynamon SR4 and basalt fiber). In Table 2 are summarized the plaster formulations developed. In the case of the plaster, a medium-low viscosity cellulose was used, to obtain, at the same time, a good capacity to retain water

for the time necessary to trigger the geopolymerization reactions, without however affecting the good fluidity of the mixture.

Table 2- Description of plaster formulations. The binder, aggregate and additives percentage indicate are referred to the total mass of plaster. S_n = sand; PV_n = expanded glass; n = aggregate size in mm.

Sample	Binder (%)	Aggregate (%)	w/b	Additive (%)
P 1	57.3	42.0 (S_{510}, $PV_{0.5\text{-}1}$, $PV_{1\text{-}2}$)	0.57	0.7 ($Culminal_{8367}$; $Silopon_{8018}$; Dynamon SR4)
P 2	57.3	42.0 (S_{510}, $PV_{0.5\text{-}1}$, $PV_{1\text{-}2}$)	0.53	0.7 ($Culminal_{15000}$; $Silopon_{8010}$; Dynamon SR4)
P 3	52.0	47.4 (S_{510}, $PV_{0.5\text{-}1}$, $PV_{1\text{-}2}$)	0.48	0.6 ($Culminal_{8367}$; Dynamon SR4)
P 4	57.0	42.2 (S_{510}, $PV_{0.5\text{-}1}$, $PV_{1\text{-}2}$)	0.48	0.8 ($Culminal_{15000}$; Dynamon SR4)
P 5	57.0	42.3 (S_{510}, $PV_{0.5\text{-}1}$, $PV_{1\text{-}2}$)	0.74	0.7($Culminal_{15000}$; $Silopon_{8010}$; Dynamon SR4; Starvis S35F)
P 6	45.0	54.3 (S_{510}, $PV_{0.5\text{-}1}$, $PV_{1\text{-}2}$)	0.74	0.7 ($Culminal_{15000}$; $Silopon_{8010}$; Dynamon SR4; Starvis S35F)
P 7	43.0	56.8 (S_{510}, $PV_{0.5\text{-}1}$)	0.47	0.2 ($Culminal_{15000}$; $Silopon_{8010}$; Basalt fiber; Starvis S35F)
P 8	43.0	56.5 (S_{510}, $PV_{0.5\text{-}1}$, Filler)	0.53	0.5 ($Culminal_{15000}$; $Silopon_{8010}$; Dynamon SR4; Basalt fiber; Starvis S35F)
P 9	43.0	56.5 (S_{510}, S_{505}; $PV_{0.5\text{-}1}$)	0.53	0.5 ($Culminal_{15000}$; $Silopon_{8010}$; Dynamon SR4; Starvis S35F; Basalt fiber; Deschofix)

2.6- Samples moulding

The preparation of the binder, mortar and plaster formulations was made in accordance with the UNI EN 998-2:2016[182] normal. The mixtures were obtained by adding the predetermined quantity of water to the powdered reagents using MATEST mixer for 5 min. The mixing times were longer than for traditional cements, to favor the dissolution of the aluminosilicate reagents by the alkaline activator. The mixtures were poured into 40x40x160 mm^3 moulds. The molds comply with the UNI EN 1015-11[183]. For each formulation and for each curing time, 3 samples were cast. The geopolymer binders, mortars and plasters have been completely characterized in their chemical-physical and mechanical properties.

3- Characterization

Fourier Transform Infrared Spectroscopy (FTIR), X-ray powder diffraction (XRPD) and the Scanning Electron Microscope (SEM) were performed to characterize the functional groups, the crystalline phases and the morphology, respectively, of the product obtained in the experiments. The instruments have been described in chapter 1, paragraphs 3.5 and 3.6 and chapter 3, paragraph 3.1.

3.1 Mechanical tests

The flexural and compressive tests were performed on all binder (***L1*** to ***L5***, ***LP2*** to ***LP5***), mortar (***M1*** to ***M8***) and plaster (***P1*** to ***P8***) formulations after 7 and 28 days from casting, according to EN 1015-11, 2019[183].

Flexural tests were carried out on prismatic samples under a three- point bending scheme, by using a MTS 2/M Universal testing machine. After failure, the two remaining halves were tested in compression, by using an INSTRON 5882

Universal machine working under loading control. Steel platens, with dimension 40 mm x 40 mm, were interposed between sample surfaces and the testing machine.

Adhesion to the support was determined on the mortars (***M4, M5*** and ***M6***) and plaster (***P8***), by pull-off test according to EN 1015- 12[184] with a MATEST pull-off tester. A 5-mm thick mortar layer was applied to an autoclavated aerated concrete (AAC) block and conditioned for 28 days at laboratory conditions (20±2° C, 65±5% RH). Adhesive strength was determined using a circular plate, of 50 mm in diameter, glued by means of epoxy resin to the surface of the mortar. The tensile load is applied through the pull-off tester, a constant speed tensile load was applied to the plate, so that failure took place between 20 and 60 s. Adhesive strength is obtained by the maximum breaking load divided by the test area.

4- Result and discussion

4.1- Binder formulations for the development of mortar

4.1.1- FTIR spectroscopy characterization

Inorganic aluminosilicate polymers are composed of "Si-O" tetrahedra and "Al-O" octahedra connected to each other by oxygen bridges. By convention the bonds of silicon are identified by the number n of oxygen bridges and are denominated with Qn (n = 0, 1, 2, 3, 4). Amorphous silica is assumed to consist only of Q4 species, which form a continuous "network" of tetrahedrons arranged in a disorderly way[185]. During the geopolymerization reaction this network is dissolved with formation of a lattice of silicon tetrahedra and aluminum tetrahedra (Al modify its original octahedral configuration).

In figure 2 are reported the FTIR spectra of all binders (***L1-5)*** and of the metakaolinite (MK) starting reagent for comparison. In the FTIR spectrum of ***L1***

(the binder formulated with alkali activator in solution) the bands marked with asterisk are related to the stretching and bending vibrations of the OH groups of the absorbed water [186], at 3260 cm^{-1} and 1650 cm^{-1}. The bands at 1107 cm^{-1}, 970 cm^{-1} and 846 cm^{-1} are assigned to the stretching vibrations of νSi-O of Q4 units, νSi-O-Al (the formation of AlO_4 units) [187]. The band centered at 1384 cm^{-1} is attributed to the vibration of the carbonate ion formed during curing. In the ***L2-5*** samples the band centered at 1476 cm^{-1} and the peaks at 874 cm^{-1} and 712 cm^{-1} are due to the vibrations of the carbonate ion (νCO_3^{2-}) formed by reaction of $Ca(OH)_2$ with atmospheric CO_2. The peaks at 1416 cm^{-1} and 846 cm^{-1} are assigned to calcium monocarboaluminate. The decrease of Q^4 units following silicate dissolution and the increase of Q^3 units during geopolymer lattice formation is evident in the red shift (1107 cm^{-1} - 1074 cm^{-1}) associated with the Si-O stretching vibration of Q^4 units.

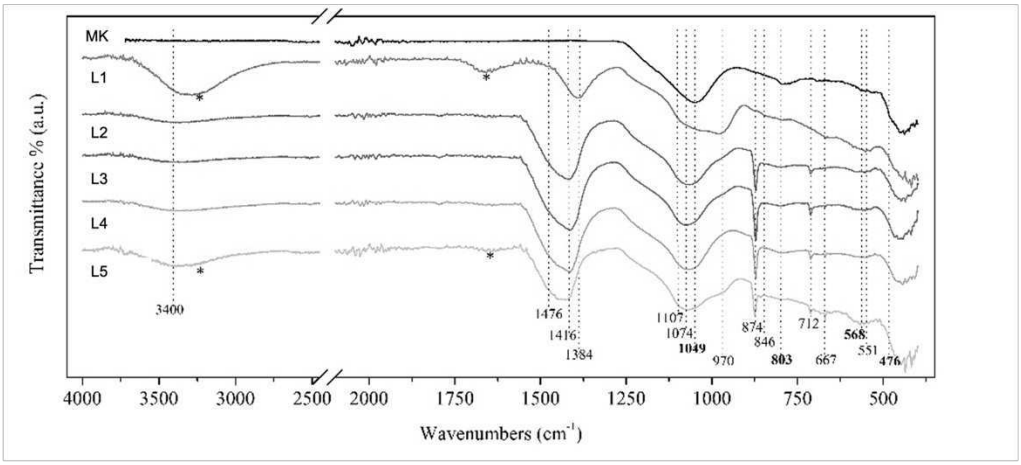

Figure 2- FTIR spectra: MK and binder L1-5 comparison

4.1.2- X-ray powder diffraction (XRPD)

The XRPD diffractograms were recorded on all geopolymer binders (fig. 3). In all the diffraction patterns are evident a large background centered between 20-35 ° 2θ, due to the amorphous component by geopolymerization process[188]. The peaks at 2θ = 20.8° and 26.6° are due to the reflection planes 100 and 011

identifying the quartz, which does not participate in the geopolymerization reaction due to its low dissolution kinetics[189,190]. The peaks at 2θ = 23.0° 25.47°, 42.5° and 57.4° are attributable to hydrated aluminum silicates (sodium, potassium or calcium) formed following geopolymerization[191]. In samples ***L2*** to ***L5*** the peaks of calcium carbonate marked by the symbol "°" relating respectively to the reflection planes 104, 110, 113, 202, 018, 116, 122 are clearly recognizable.

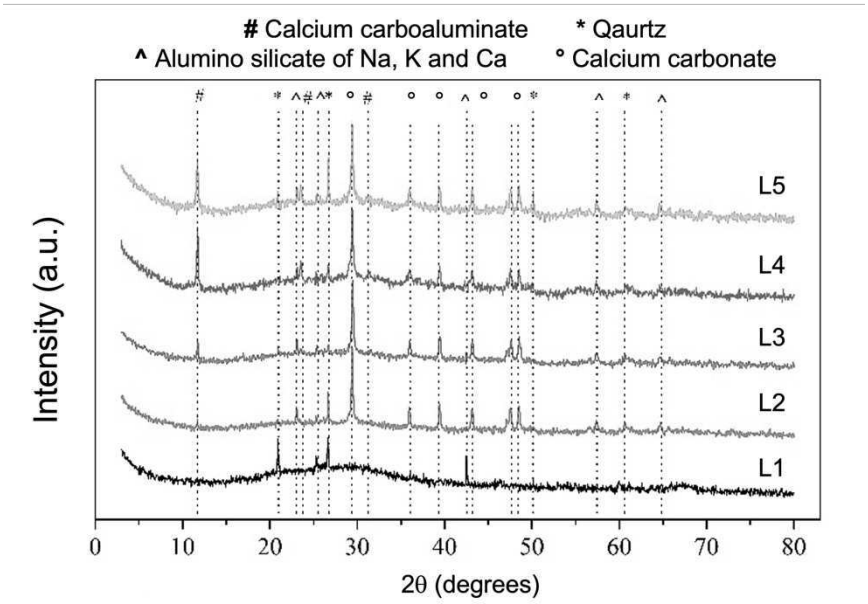

Figure 3- XRD comparison of L1-L5. The symbols indicate the attributions

4.1.3- Mechanical test

The flexural and compressive strength tests (fig.4 a-b respectively) were carried out at 7 and 28 days of maturation on geopolymer binder ***L1*** to ***L5***. All the formulations obtained with the alkali activator in powder form (***L2*** to ***L5***) show better mechanical properties than ***L1*** formulation.

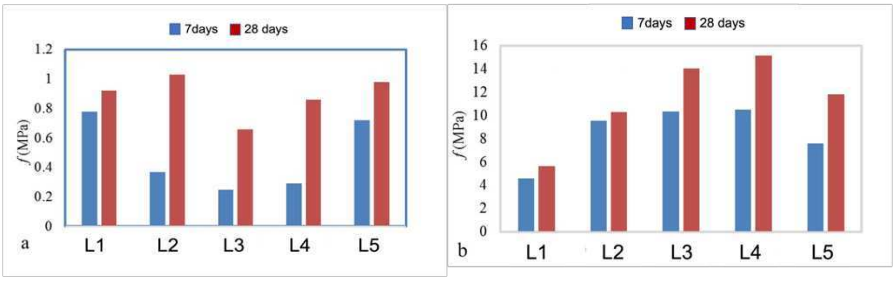

Figure 4- a) Flexural and b) compressive strength test of L1-L5 binders

To realize the mortar, the ***L4*** binder based on $Ca(OH)_2$ and K-silicate, which showed high compressive strength already after 7 days and good flexural strength, was chosen. The advantages of using this formulation based on calcium hydroxide and potassium silicate concern the safety of their use as the reaction is not exothermic and the potassium silicate avoids the formation of saline efflorescence or the formation of gypsum.

4.2- Binder formulations for the development of plaster

4.2.1- FTIR spectroscopy

The FTIR spectra acquired on the ***LP1*** to ***LP7*** geopolymer binders are shown in figure 5. The bands at 3300 cm^{-1} and 1640 cm^{-1} are due to the stretching and bending vibrations of the adsorbed water. The stretching vibrations of the carbonate ion are evident at 1407 cm^{-1}, 874 cm^{-1} and 710 cm^{-1}. The presence of carbonates was also highlighted for the "***L***" binders based on metakaolinite and used for the development of the mortar. This is due to the reaction between the alkaline activator and atmospheric CO_2 [192], during the curing process. The peak at 1050 cm^{-1} is associated with the Si-O stretching vibration of the Q^4 units, while the band at 957 cm^{-1} is indicative of the presence of Q^3 units, probably deriving from the dissolution of the starting silicates in alkaline environment. The small

band at 698 cm^{-1} is due to Si-O-Al bending. The asterisks indicate bands associated with the starting slag.

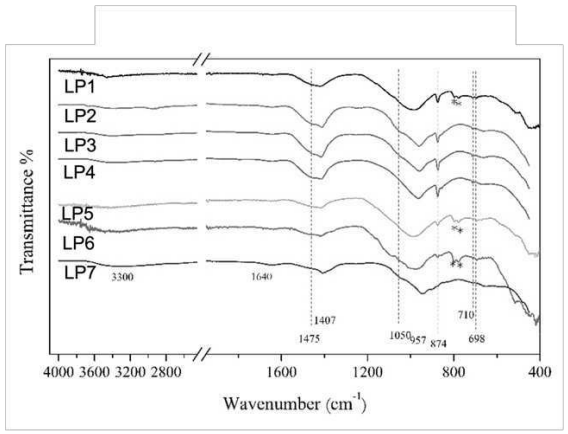

Figure 5- FTIR spectra of LP geopolymers. The asterisks indicate vibrations due to the starting material

4.2.2- Mechanical test

Figures 6a and 6b, show the flexural and compressive tests on the ***LP2*** to ***LP5*** formulations. The ***LP3*** and ***LP4*** samples show very high flexural strength, while ***LP2*** and ***LP5*** have higher compressive strength.

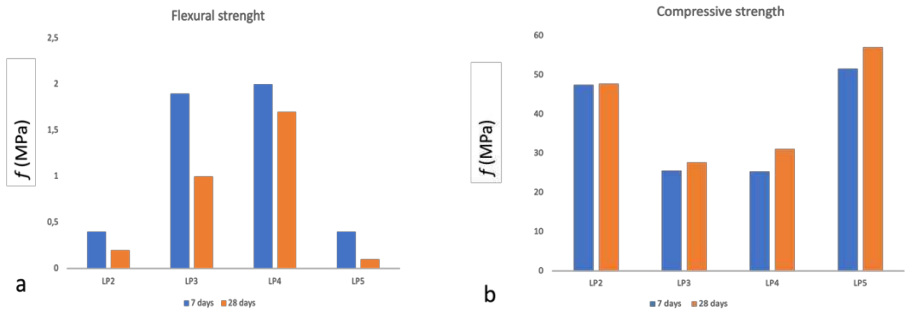

Figure 6- a) Flexural strength and b) compressive strength on LP2-LP5 at 7 and 28 days of curing

Based on the results of the preliminary experimentation, the ***LP2*** formulation was chosen as a binder for the plaster, which has excellent mechanical performance.

The ***LP3*** and ***LP4*** despite the excellent mechanical performance, were not used for the formulation of the plaster because they are not workable during mixing. The binder ***LP5***, containing KOH in the alkaline activator formulation, was not selected because it develops too much reaction heat during mixing.

4.3- Formulations for the development of mortar

To obtain a mortar with good chemical-physical characteristics and high mechanical performance, various mixes were made (summarized in Table 1). In the formulations the additives, water/binder ratio, aggregate/binder ratio were varied. The significant results obtained on the various mortars made with the selected geopolymer binder ***L4*** after the initial experimentation phase, are shown below. Attention is paid to the use of mortars prepared with the addition of polysaccharide additives to verify the influence they have on the mechanical properties. The tested mortars were formulated with the same percentage ratios of corn starch and plasticizer (Dehscofix) but with cellulose of a different nature and in different ratios: high and medium viscosity cellulose, microfibrillated cellulose (CMF) and nanocrystalline cellulose (CNC). Thanks to its high surface area, micro and nanocrystalline celluloses influence the mechanical properties of the material even in very low quantities. Medium and high viscosity celluloses, while exerting a considerable influence on the material, allow to maintain adequate mechanical properties. Moreover, the use of fluidifying additives which improve the workability of the mortar, has a great importance. After evaluating the influence of additives and cellulose on the workability and mechanical performance of the mortar, the adhesion properties and correction time on autoclaved aerated blocks were evaluated. Finally, the mortar with the best properties was selected and completely characterized.

4.3.1- FTIR spectroscopy

As discussed for the ***L4*** binder, also the FTIR spectrum of the mortar ***M1*** without additives (figure 7) provides the same vibrational bands relating to the stretching vibrations of the OH groups, stretching and bending of the carbonate ion, with the presence of peaks assigned to calcium monocarboaluminate. The doublet at 688 and 670 cm^{-1} is attributable to K_2CO_3, formed as a secondary reaction between potassium silicate and calcium hydroxide. The band at 1074 cm^{-1} is assigned to Si-O-Si stretching vibration, while the band at 1065 cm^{-1} is attributed to the stretching vibration of the Si-O-T groups. The peaks at 988 cm^{-1} and 526 cm^{-1} correspond to the stretching and bending vibrations, respectively. These two last peaks are due to the new Si-O-T groups of the Q^4 units, formed following the geopolymerization process.

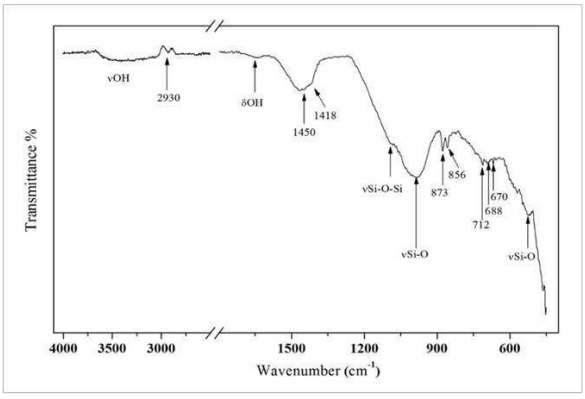

Figure 7- FTIR spectrum on mortar M1. The arrows highlight the functional groups and wavenumbers of the peaks.

4.3.2- X-ray powder diffraction (XRPD)

Figure 8 shows the diffraction pattern of the mortar ***M1*** without additives. As a comparison, that of the binder was also reported. In both XRPD patterns we note the presence of the amorphous background at 2θ between 20° and 35°, which can

be associated with the disordered structure of the geopolymers[188]. The different peaks relating to the crystalline phases quartz, calcium monocarboaluminate and calcium carbonate, are highlighted in figure 8 with the symbols described in the legend. Other peaks were attributed to K, Ca silicate and aluminum silicate, which are due to rearrangement of the Al-O and Si-O network from metakaolinite after reaction with alkali activator solution. Peaks attributable to the K-zeolite-like and pyroxene phases were also identified in the diffractogram of the mortar.

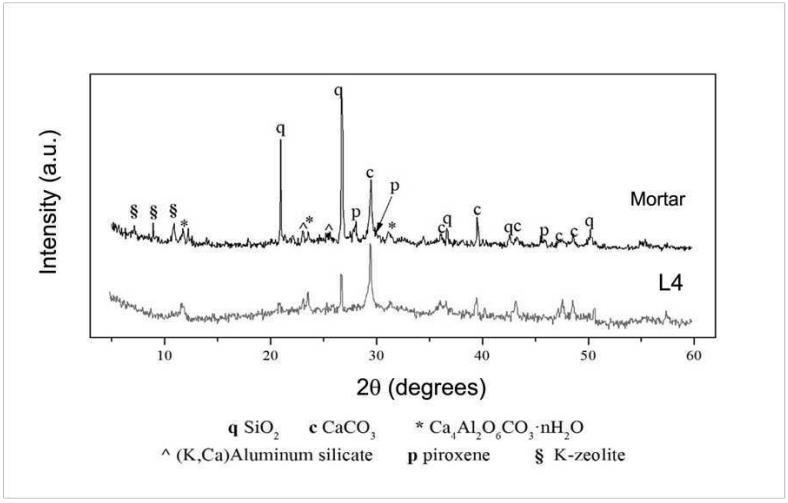

Figure 8- XRD pattern on binder L4 and the mortar M1.

4.3.3- Differential Scanning Calorimetry (DSC)

The thermogram and the differential analysis of the binder ***L4*** and mortar ***M1*** up to 900 °C are shown in figure 9. Four different weight losses are noted in the thermogram (marked with I, II, III to IV). The thermogram of the ***M1*** mortar shows three inflections due to the loss of the absorbed water (I), the removal of the chemically bound water (II) and finally, the dehydroxylation of the siloxane OH groups (III). The release of CO_2 in the decomposition of the carbonates is present in (IV). In the thermogram of binder ***L4*** the same weight variations are noted with two additional peaks: at 280 °C there is the dehydroxylation of the

siloxane OH groups and consequent polycondensation in Si-O-Si bonds and a peak at 464 °C due to the dehydroxylation of $Ca(OH)_2$, which did not react with the matakaolinite.

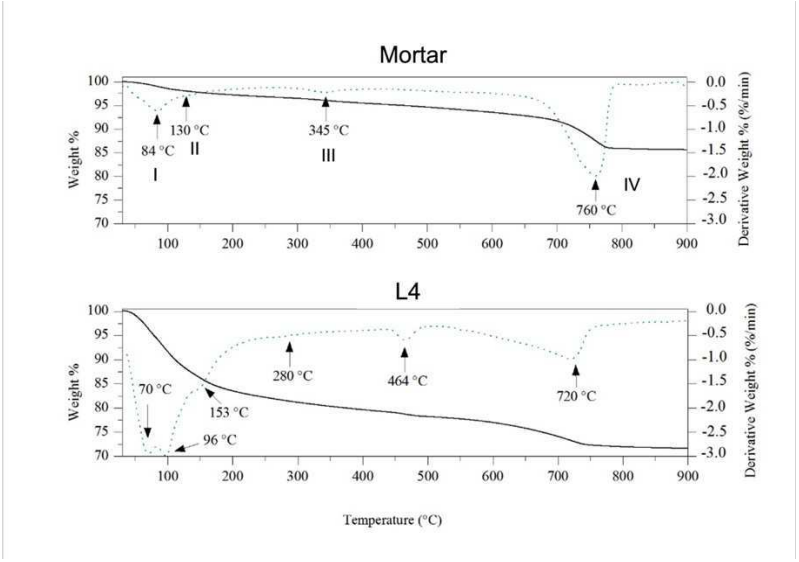

*Figure 9- Thermogravimetric analysis on binder **L4** and mortar **M1**.*

4.3.4- Scanning Electron Microscope (SEM)

Morphological investigation and elemental analysis were performed on the ***M1*** mortar by SEM-EDS. The EDS microanalysis was acquired on the area highlighted in red in the backscattered electron image (figure 10a). The table (figure 10c) shows the semi-quantitative analysis relating to the EDS spectrum. The presence of Au is determined by the metallization process to which the sample has been subjected.

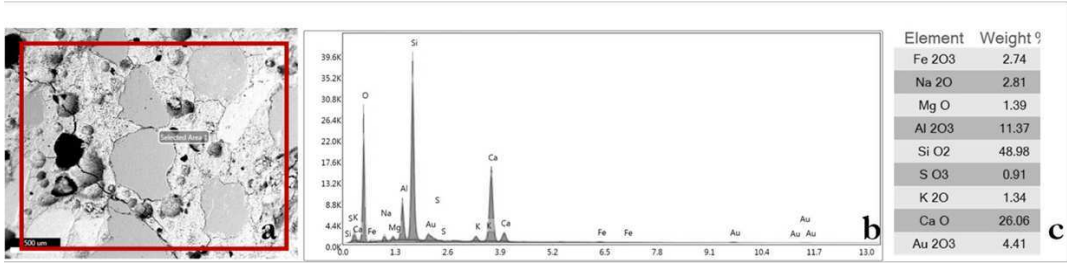

Figure 10- a) Image acquired in backscattered electrons on M1 mortar; b) EDS microanalysis. Semi-quantitative table related to the EDS spectrum (c).

Grains with 50 μm in size, embedded in the matrix are clearly visible in figure 10a. Irregular submillimeter clasts and high Si content were due to the quartz sand added into the mortar. The main elements detected by EDS microanalysis were Ca, Al and Si, with lower K content.

4.3.5- Additives influences

4.3.5.1- Adhesive type

To evaluate the influence of the polysaccharide additives were tested three different mortar formulation, already reported in table 1: ***M2*** with alginate, ***M3*** with rice starch and ***M4*** with maize starch. Table 3 and figure 11 show the results of the consistency and mechanical resistance tests. These parameters are fundamental to evaluate if the polysaccharides used improve the adhesion between mortar and aerate autoclaved block.

Table 3- Influence of adhesive additives on mortar consistency

Sample	w/b ratio	Consistency (mm)
M2	1	146
M3	0.97	153
M4	1.1	148

The selected dosages of the three adhesives provided similar consistency values for the mortar, while in terms of mechanical performances, the addition of alginate was not satisfactory since the achieved compressive strength was lower than 5 MPa. On the contrary, the two mortars with rice starch (***M4***) and maize starch (***M5***) provided very similar compressive and flexural tensile strengths, with values around 8 MPa and 1.3 MPa, respectively. The mortar with the addition of maize starch had two main advantages: a lower required adhesive dosage, and the possibility of adding it to the admixture at room temperature. Instead, rice starch should be preliminary dissolved in warm water, at a temperature over 70° C, which seemed not feasible for possible on-site applications. In conclusion, the most promising candidate for geopolymeric mortar is ***M5***.

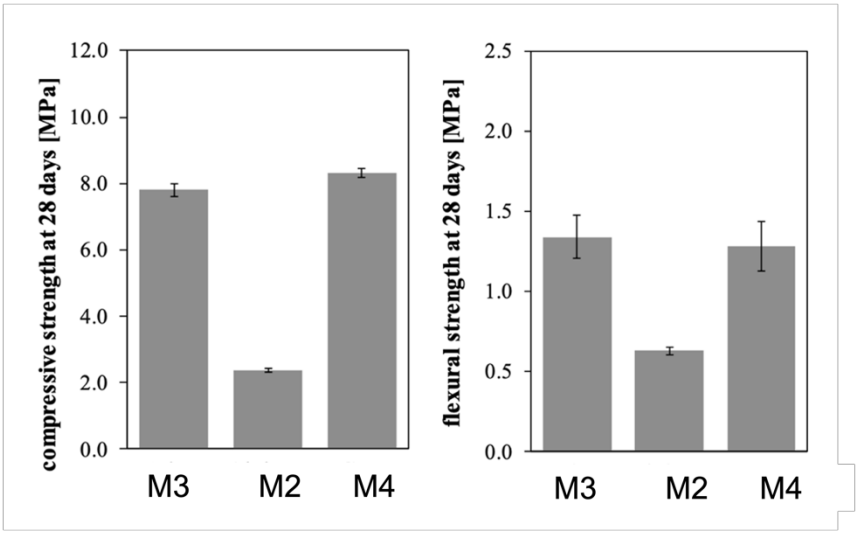

Figure 11- Influence of adhesive additives on mortar mechanical strength

4.3.5.2- Cellulose and superplasticizer

Cellulose is usually added in mortars for its water retention properties and thickening effect, that improves the construction performance and workability of

the final product. In this study, the addition of medium viscosity cellulose in ***M1*** mortar (as reported in table 1) determined however a significant reduction of mechanical properties, as shown in figure 12. The mechanical properties of the following mortars were compared: ***M4*** with starch, ***M5*** with starch and cellulose and ***M6*** with starch, cellulose and superplasticizer. As evident in figure 12a, the mortar containing both cellulose and superplasticizer achieved an acceptable compressive strength, resulting as the best candidate. The influence of cellulose type on mortar properties (figure 12b) was also studied, by substituting the medium viscosity cellulose with microfibrillated (CMF) (***M7***) or nanocrystalline cellulose (CNC) (***M8***). The type and amount of superplasticizer were kept the same for all the mortars. The corresponding results are summarized in Table 4.

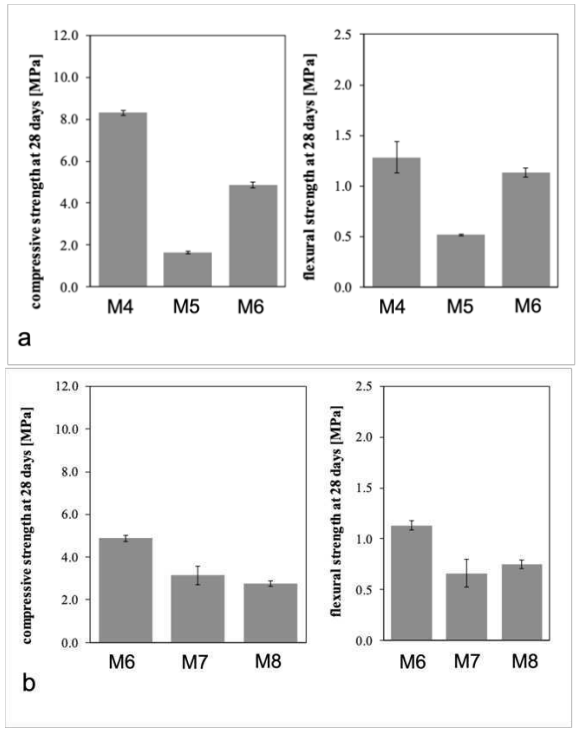

Figure 12- a) Influence of cellulose and superplasticizer addition on mortar mechanical strengths; b) Influence of cellulose type on mortars mechanical strengths.

For mortars ***M5*** and ***M6*** lower consistency respect to the other two mortars reported in table 4 were observed. The influence of microfibrillated and nanocrystalline cellulose was remarkable even at low dosages, due to their high surface area. This effect was positive about consistency measurements but led to an excessive reduction of mechanical strengths (figure 12b), not compatible with the usage in bearing masonry structures.

Table 4- Influence of different types of cellulose on mortar consistency

Sample	w/b ratio	Consistency (mm)
M5	1.1	146
M6	1.1	153
M7	1.1	173
M8	1.1	167

4.3.5.3- Correction time and adhesion to the support

For three of the tested mortars (that is the reference mortar ***M1***, and the two mortars with cellulose ***M5***, or with cellulose and superplasticizer ***M6***), correction time and adhesion to the support were also determined. The values of the measured correction time are reported in Table 5. The reference mortar and the mortar with the addition of medium viscosity cellulose did not adhere to the support. With the addition of the superplasticizer, a good correction time of mortar ***M6*** equal to 4 min was achieved.

Table 5- Correction time on M1, M5 and M6

Sample	Correction tine (min)
M1	No adhesion
M5	No adhesion
M6	4

The results of adhesion tests are summarized in Table 6. For the reference mortar, an adhesive fracture was observed, with failure at the interface between the mortar and the substrate. For ***M5*** and ***M6*** mortars, a cohesive fracture took place, with failure within the mortar layer. All the results reported above indicate that the best compromise is for ***M6*** mortar.

Table 6- Adhesive strength for three selected mortars

Sample	Adhesive strength (MPa)	Failure mode
M4	0.03	A
M5	0.23	B
M6	0.29	B

To increase correction time, the possible addition of other commercial additives commonly used in mortars was also explored, although with not satisfying results. Starting from ***M6*** mortar, tartaric acid was added as retarder, while polymeric gel was used to enhance the resistance to moisture and water seepage. The mortar formulations (***M9*** to ***M11***) are summarized in table7. In these attempts, high viscosity cellulose was mixed with a small percentage (0.03%) of a different type of cellulose, to improve water retention. The influence exerted by these further additives for the consistency, correction time and mechanical strengths at 28 days of curing, is shown in Table 7. Correction time was not improved, but mechanical strengths were reduced. A correction time greater than 10 min was only obtained for ***M11***. However, the corresponding decrease in compressive strength was unacceptable.

Table 7- Admixtures with commercial additives to improve correction time

Sample	**M9**	**M10**	**M11**
w/b ratio	1.3	1.3	1.7
Additives	Maize starch (0.5%), cellulose (0.33%), tartaric acid (0.025%), superplasticizer (0.03%)	Maize starch (0.5%), cellulose (0.33%), tartaric acid (0.025%), superplasticizer (0.03%), polymer gel (0.05%)	Maize starch (0.5%), cellulose (0.66%), tartaric acid (0.013%), superplasticizer (0.025%), polymer gel (0.05%)
Consistency (mm)	143	149	139
Mean compressive strength (MPa)	3.8	3.4	0.5
Mean flexural strength (MPa)	0.82	0.78	0.17
Correction time (min)	≈ 4	No adherence	≥10

As evident from the results reported in table 7, the addition of retardant and of the polymeric gel, decreases the mechanical properties. Therefore, they are not suitable for the application. Only mortar ***M9*** represents the most acceptable compromise, in which the correction time is 4 min and the compressive and flexural strength are comparable with those of ***M6*** mortar. These two mortars represent the products with the best performance.

4.4- Formulations for the development of plaster

As reported in the experimental part, various mixtures of plaster (reported in Table 2) were studied. Some parameters were varied, such as: additives, water/binder ratio, inert/binder ratio. Table 8 summarizes the results obtained for flexural and compressive strength and the adherence on supports. In parentheses the days of maturation are specified. For some samples (***P4*** and ***P5***) it was not possible to develop tests. Good flexural and compressive strength values were recorded for all samples. On the other hand, the adherence on support is not satisfactory in all plasters. The only exception is for ***P8*** plaster.

Table 8- Mechanical properties on P1 to P8 plasters

Sample	Flexural strength (MPa)	Compressive strength (MPa)	Adherence on support
P 1	1.1(7 days) 0.5 (28 days)	6.3 (7 days) 6.5 (28 days)	No
P 2	1.3 (7days) 0.6 (28 days)	6.0 (7 days) 7.9 (28 days)	No
P 3	1.41 (43 days)	16.1 (43 days)	No
P 4	-	-	No
P 5	-	5.2 (28 days)	No
P 6	1.27 (21days)	6.03 (21days)	No
P 7	1.75 (28 days)	13.2 (28 days)	No
P 8	1.07 (28 days)	7.4 (28 days)	Yes

From the experimental results shown in table 8, it is possible to select ***P8*** sample as the best geopolymer plaster, characterized by good mechanical properties. To define the failure mode for the adhesion test, 5 samples of **P8** plaster were

prepared (Table 9). The strength of adhesion to the support was evaluated by pull-off test[184] as described in paragraph 3.1.

*Table 9- Adherence test on **P8** samples.*

Sample	F_u (N)	Area mm^2	Adherence strength f_u (MPa)	Failure mode
1	0.173	1.96	0.09	A/C
2	0.228	1.96	0.12	A
3	0.105	1.96	0.05	A/C
4	0.113	1.96	0.06	C
5	0.347	1.96	0.18	C

Two types of failure occurred: type A, adhesion fracture and type C, cohesion fracture. Type A fracture is a fracture at the interface between plaster and substrate. Type C fracture, on the other hand, causes the fracture of the support.

4.4.1- FTIR spectroscopy

Figure 13 shows the FTIR spectra of the binder ***LP2*** (AAP, sodium silicate, calcium hydroxide and calcium carbonate) and of the alkaline activated plaster ***P8***. The vibration band at 967 cm^{-1} and the shoulder at 1156 cm^{-1} (visible in the plaster spectrum) are attributed to stretching vibrations of the Si-O-Al groups and Si- O-Si of Q^4 units, respectively[187,193]. The band at 1005 cm^{-1} is associated with the decrease of Q^4 units following the dissolution of the silicates. The band at 670 cm^{-1}, attributed to the symmetrical stretching vibration of the Si–O–Al groups, allows us to confirm that some Q^4 units within the Si–O–Si lattice have been replaced by AlO_4 units to form the gel polymeric[162]. The band at 1410 cm^{-1} and at 1474 cm^{-1}and the peaks at 874 cm^{-1}, 860 and 712 cm^{-1} are due to the vibrations of the carbonate ion (νCO_3^{2-}) of the calcium carbonate formed by reaction with atmospheric CO_2. The formation of carbonates is a frequent phenomenon.

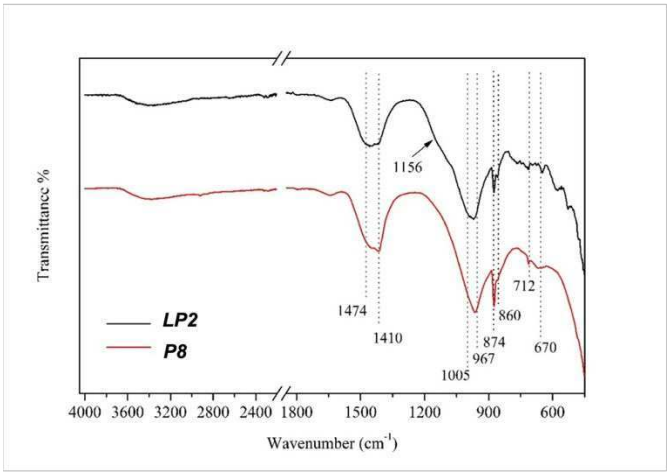

*Figure 13- FTIR spectrum of the binder **LP2** and the plaster **P8***

4.4.2- X-ray powder diffraction (XRPD)

The diffraction pattern of plaster ***P8,*** reported in figure 14, shows various crystalline phases: quartz from the starting slag, calcium carbonate (calcite) formed following the carbonation reaction of the $Ca(OH)_2$ present in the alkaline activator, and magnesite, probably present in the starting slag. The background centered between 2θ at 20° and 37° is due to the amorphous fraction typical of the geopolymeric matrix[176].

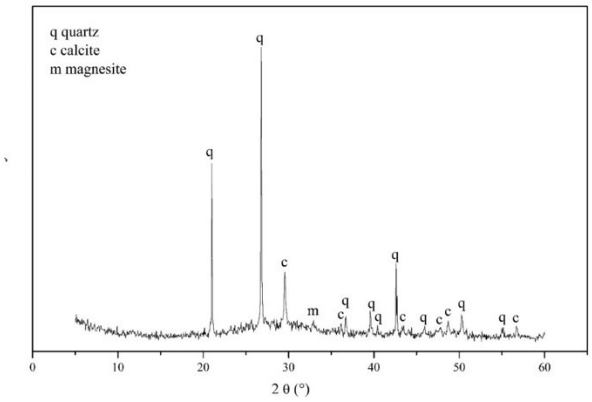

*Figure 14- Diffraction pattern of the plaster **P8** after 28 days of curing.*

4.4.3- Differential Scanning Calorimetry (DSC)

Figure 15 shows the DSC curve of the plaster ***P8***. The curve shows some endothermic peaks associated with the loss of water, in the region between 100 °C and 250 °C. The first two endothermic peaks are related to the loss of the bound adsorbed water and to the loss of the interlayer water of the hydration products. The third peak, at 200 °C, may be related to the loss of structural water from the geopolymeric lattice and hydrated calcium aluminosilicates. Moreover, there are no exothermic peaks associated with new crystallizations favored by the temperature. Evidently in the curing phase the crystalline phases associated with the formation of the polymeric network have already been completed.

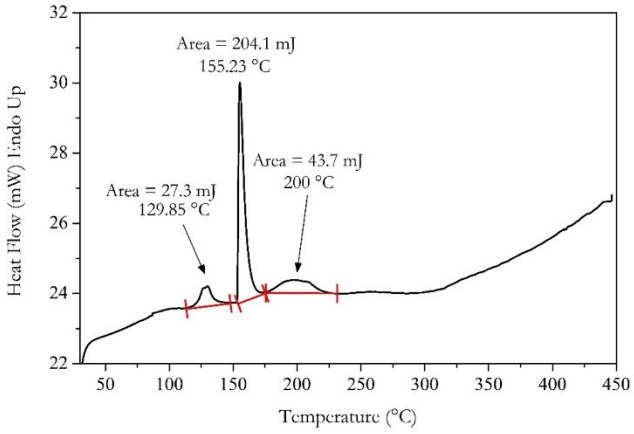

*Figure 15- DSC curve of plaster **P8** at 28 days*

4.4.4- Scanning Electron Microscope (SEM)

In figure 16 are reported the morphological investigation (figure 16 a) and of the EDS microanalysis (figure 16b) results obtained for ***P8*** plaster. The EDS microanalysis was acquired on the area highlighted in red in the backscattered electron image. The presence of Au is due to the metallization process. The plaster ***P8*** has a very porous structure with submillimetric pores distributed in the

binder matrix. The clasts, due to the inert material, are well cemented. No fractures are visible in the matrix. The main elements detected by EDS microanalysis were Ca, Al, Si and Na, already present in the ***LP2*** binder.

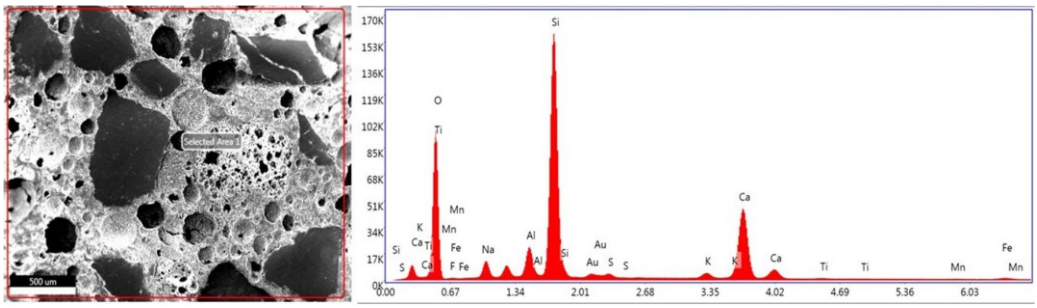

Figure 16- a) Image acquired in backscattered electrons (x68 magnification); (b) EDS microanalysis of sample ***P8***

All results suggest that the best geopolymer plaster formulation is ***P8***, as already discussed. In this formulation the presence of natural additives and filler, allowed to obtain the satisfactory performances for flexural and compressive strength and for the adherence on autoclaved aerated block.

5- Conclusions

This research activity was focused on the development of new eco-sustainable materials for building. The geopolymeric mortars and plasters here proposed, were obtained in a "one-part" reaction, in which alkali activators were used in powder. Attention was paid to the natural additive influences: their action is essential to improve the properties of the blend, such as elasticity, adhesion and correction time. As the use of additives in the formulations decreases the flexural and compressive strengths, it has been necessary to find the right compromise between the best mechanical properties obtainable and the quantity of additives used.

In this chapter the geopolymer-based binder for mortar and plaster has been studied. After choosing the type of suitable binder (called ***L4*** and ***LP2***), mortars and plasters were developed. Successively, for both materials, several formulations were proposed: best results were obtained for ***M6*** mortar and ***P8*** plaster, respectively. The influence of additives was evaluated. Based on the experimental results, the following conclusions can be highlighted on mortar formulations:

- maize starch is promising as adhesive additive in alkali-activated mortars, since its addition does not produce an excessive decrease of mortar mechanical performances. On the contrary, the use of alginate or rice starch is less feasible.
- cellulose type has a limited effect on mortar workability, while it strongly influences the mechanical performances.
- superplasticizer addition improves both the correction time and the adhesion of the mortar to the autoclaved aerate block. The addition of other commercial additives, such as tartaric acid and polymer gel, has a negligible influence on those properties.

On the other hand, for plaster formulation the presence of the air entraining agent, the water reservoir, the superplasticizer, the expanded glass, the filler and the methyl cellulose, allow to obtain the satisfactory performances for flexural and compressive strength and for the adherence on autoclaved aerated block. Satisfactory results have been obtained for ***P8*** plaster. For example, as evidenced by FTIR and XRD investigations, even with the use of powder products, complete geopolymerization can be observed. The morphological investigation by SEM shows the presence of clasts well incorporated inside. The results obtained are promising, but further studies are required in order to develop the highest performing product to be used in the building sector.

References

1. Pylkkänen R, Mohammadi P, Arola S, et al. In Vitro Synthesis and Self-Assembly of Cellulose II Nanofibrils Catalyzed by the Reverse Reaction of Clostridium thermocellum Cellodextrin Phosphorylase. *Biomacromolecules*. 2020;21(10):4355-4364. doi:10.1021/acs.biomac.0c01162
2. Klemm D, Heublein B, Fink HP, Bohn A. Cellulose: Fascinating biopolymer and sustainable raw material. *Angewandte Chemie - International Edition*. 2005;44(22):3358-3393. doi:10.1002/anie.200460587
3. Habibi Y, Lucia LA, Rojas OJ. Cellulose nanocrystals: Chemistry, self-assembly, and applications. *Chem Rev*. 2010;110(6):3479-3500. doi:10.1021/cr900339w
4. Habibi Y. Key advances in the chemical modification of nanocelluloses. *Chem Soc Rev*. 2014;43(5):1519-1542. doi:10.1039/c3cs60204d
5. Kroon-Batenburg LMJ, Kroon J. *The Crystal and Molecular Structures of Cellulose I and II*. Vol 14.; 1997.
6. Lefebvre J, Gray DG. AFM of adsorbed polyelectrolytes on cellulose I surfaces spin-coated on silicon wafers. *Cellulose*. 2005;12(2):127-134. doi:10.1007/s10570-004-1574-0
7. Lu P, Hsieh Y lo. Preparation and properties of cellulose nanocrystals: Rods, spheres, and network. *Carbohydr Polym*. 2010;82(2):329-336. doi:10.1016/j.carbpol.2010.04.073
8. Araki J, Wada M, Kuga S, Okano T. *Flow Properties of Microcrystalline Cellulose Suspension Prepared by Acid Treatment of Native Cellulose*. Vol 142.; 1998.

9. Sunasee R, Hemraz UD. Synthetic strategies for the fabrication of cationic surface-modified cellulose nanocrystals. *Fibers*. 2018;6(1). doi:10.3390/FIB6010015
10. Khanjanzadeh H, Behrooz R, Bahramifar N, et al. Surface chemical functionalization of cellulose nanocrystals by 3-aminopropyltriethoxysilane. *Int J Biol Macromol*. 2018;106:1288-1296. doi:10.1016/j.ijbiomac.2017.08.136
11. Rafieian F, Jonoobi M, Yu Q. A novel nanocomposite membrane containing modified cellulose nanocrystals for copper ion removal and dye adsorption from water. *Cellulose*. 2019;26(5):3359-3373. doi:10.1007/s10570-019-02320-4
12. Habibi Y, Chanzy H, Vignon MR. TEMPO-mediated surface oxidation of cellulose whiskers. *Cellulose*. 2006;13(6):679-687. doi:10.1007/s10570-006-9075-y
13. Bergamonti L, Potenza M, Haghighi Poshtiri A, et al. Ag-functionalized nanocrystalline cellulose for paper preservation and strengthening. *Carbohydr Polym*. 2020;231. doi:10.1016/j.carbpol.2019.115773
14. Böhme N, Anders M, Reichelt T, Schuhmann K, Bridarolli A, Chevalier A. New treatments for canvas consolidation and conservation. *Herit Sci*. 2020;8(1). doi:10.1186/s40494-020-0362-y
15. Basile R, Bergamonti L, Fernandez F, et al. Bio-inspired consolidants derived from crystalline nanocellulose for decayed wood. *Carbohydr Polym*. 2018;202:164-171. doi:10.1016/j.carbpol.2018.08.132
16. Weddigen E. L attenzione alle superfici pittoriche: materiali e metodi per il consolidamento e metodi scientifici per valutarne l efficacia. In: ; 2006:7-10.

17. Giorgi R, Dei L, Ceccato M, Schettino C, Baglioni P. Nanotechnologies for conservation of cultural heritage: Paper and canvas deacidification. *Langmuir*. 2002;18(21):8198-8203. doi:10.1021/la025964d
18. Penava Ž, Penava DŠ, Tkalec M. Experimental analysis of the tensile properties of painting canvas. *Autex Research Journal*. 2016;16(4):182-195. doi:10.1515/aut-2015-0023
19. Mttkknburg -Laura MF, Lopr^ F. *Failure Mechanisms in Canvas Supported Pain-Tings: Approaches for Developing Consolidation Protocols*.; 2006.
20. Sandu ICA, Schäfer S, Magrini D, Bracci S, Roque CA. Cross-section and staining-based techniques for investigating organic materials in painted and polychrome works of art: A review. In: *Microscopy and Microanalysis*. Vol 18. ; 2012:860-875. doi:10.1017/S1431927612000554
21. Zanetti M, Calvini P. Dalla tutela al restauro del patrimonio librario e archivistico Storia, esperienze, interdisciplinarietà a cura di La chimica e il restauro dei manoscritti Qualche luce, molte ombre. Published online 2018. doi:10.14277/6969-215-4/SABP-4-20
22. Bridarolli A, Odlyha M, Nechyporchuk O, et al. Evaluation of the Adhesion and Performance of Natural Consolidants for Cotton Canvas Conservation. *ACS Appl Mater Interfaces*. 2018;10(39):33652-33661. doi:10.1021/acsami.8b10727
23. Cataldi A, Berglund L, Deflorian F, Pegoretti A. A comparison between micro- and nanocellulose-filled composite adhesives for oil paintings restoration. *Nanocomposites*. 2015;1(4):195-203. doi:10.1080/20550324.2015.1117239
24. Nechyporchuk O, Kolman K, Oriola M, Persson M, Holmberg K, Bordes R. Accelerated ageing of cotton canvas as a model for further

consolidation practices. *J Cult Herit*. 2017;28:183-187. doi:10.1016/j.culher.2017.05.010

25. Grande CJ, Torres FG, Gomez CM, Carmen Bañó M. Nanocomposites of bacterial cellulose/hydroxyapatite for biomedical applications. *Acta Biomater*. 2009;5(5):1605-1615. doi:10.1016/j.actbio.2009.01.022
26. Eichhorn SJ, Dufresne A, Aranguren M, et al. Review: Current international research into cellulose nanofibres and nanocomposites. *J Mater Sci*. 2010;45(1):1-33. doi:10.1007/s10853-009-3874-0
27. Kim J, Yun S, Ounaies Z. Discovery of cellulose as a smart material. *Macromolecules*. 2006;39(12):4202-4206. doi:10.1021/ma060261e
28. Bergonzi C, Remaggi G, Graiff C, et al. Three-dimensional (3d) printed silver nanoparticles/alginate/nanocrystalline cellulose hydrogels: Study of the antimicrobial and cytotoxicity efficacy. *Nanomaterials*. 2020;10(5). doi:10.3390/nano10050844
29. Bergamonti L, Graiff C, Bergonzi C, et al. Photodegradation of Pharmaceutical Pollutants: New Photocatalytic Systems Based on 3D Printed Scaffold-Supported Ag/TiO2 Nanocomposite. *Catalysts*. 2022;12(6). doi:10.3390/catal12060580
30. Axpe E, Oyen ML. Applications of alginate-based bioinks in 3D bioprinting. *Int J Mol Sci*. 2016;17(12). doi:10.3390/ijms17121976
31. Aderibigbe BA, Buyana B. Alginate in wound dressings. *Pharmaceutics*. 2018;10(2). doi:10.3390/pharmaceutics10020042
32. Knill CJ, Kennedy JF, Mistry J, et al. Alginate fibres modified with unhydrolysed and hydrolysed chitosans for wound dressings. *Carbohydr Polym*. 2004;55(1):65-76. doi:10.1016/j.carbpol.2003.08.004
33. Inbathamizh L, Ponnu TM, Mary EJ. In vitro evaluation of antioxidant and anticancer potential of Morinda pubescens synthesized silver

nanoparticles. *J Pharm Res*. 2013;6(1):32-38. doi:10.1016/j.jopr.2012.11.010

34. Chernousova S, Epple M. Silver as antibacterial agent: Ion, nanoparticle, and metal. *Angewandte Chemie - International Edition*. 2013;52(6):1636-1653. doi:10.1002/anie.201205923
35. Elviri L, Foresti R, Bergonzi C, et al. Highly defined 3D printed chitosan scaffolds featuring improved cell growth. *Biomedical Materials (Bristol)*. 2017;12(4). doi:10.1088/1748-605X/aa7692
36. Reshmy R, Philip E, Madhavan A, et al. Nanocellulose as green material for remediation of hazardous heavy metal contaminants. *J Hazard Mater*. 2022;424. doi:10.1016/j.jhazmat.2021.127516
37. Sescu AM, Favier L, Lutic D, Soto-Donoso N, Ciobanu G, Harja M. Tio2 doped with noble metals as an efficient solution for the photodegradation of hazardous organic water pollutants at ambient conditions. *Water (Switzerland)*. 2021;13(1). doi:10.3390/w13010019
38. Bergamonti L, Gentili S, Acquotti D, Tegoni M, Lottici PP, Graiff C. Toxic metal sequential sequestration in water using new amido-aminoacid ligand as a model for the interaction with polyamidoamines. *J Hazard Mater*. 2021;410. doi:10.1016/j.jhazmat.2020.124585
39. Karim Z, Claudpierre S, Grahn M, Oksman K, Mathew AP. Nanocellulose based functional membranes for water cleaning: Tailoring of mechanical properties, porosity and metal ion capture. *J Memb Sci*. 2016;514:418-428. doi:10.1016/j.memsci.2016.05.018
40. Mohamed MA, Salleh WNW, Jaafar J, et al. Physicochemical characterization of cellulose nanocrystal and nanoporous self-assembled CNC membrane derived from Ceiba pentandra. *Carbohydr Polym*. 2017;157:1892-1902. doi:10.1016/j.carbpol.2016.11.078

41. Bai H, Li Z, Zhang S, Wang W, Dong W. Interpenetrating polymer networks in polyvinyl alcohol/cellulose nanocrystals hydrogels to develop absorbent materials. *Carbohydr Polym*. 2018;200:468-476. doi:10.1016/j.carbpol.2018.08.041
42. Lewis L, Hatzikiriakos SG, Hamad WY, Maclachlan MJ. Freeze-Thaw Gelation of Cellulose Nanocrystals. *ACS Macro Lett*. Published online 2019:486-491. doi:10.1021/acsmacrolett.9b00140
43. Gorgieva S, Vogrinčič R, Kokol V. The Effect of Membrane Structure Prepared from Carboxymethyl Cellulose and Cellulose Nanofibrils for Cationic Dye Removal. *J Polym Environ*. 2019;27(2):318-332. doi:10.1007/s10924-018-1341-1
44. Wang M, Jia X, Liu W, Lin X. Water insoluble and flexible transparent film based on carboxymethyl cellulose. *Carbohydr Polym*. 2021;255. doi:10.1016/j.carbpol.2020.117353
45. Rahman MS, Hasan MS, Nitai AS, et al. Recent developments of carboxymethyl cellulose. *Polymers (Basel)*. 2021;13(8). doi:10.3390/polym13081345
46. de France KJ, Hoare T, Cranston ED. Review of Hydrogels and Aerogels Containing Nanocellulose. *Chemistry of Materials*. 2017;29(11):4609-4631. doi:10.1021/acs.chemmater.7b00531
47. Nishiyama Y, Kim UJ, Kim DY, Katsumata KS, May RP, Langan P. Periodic disorder along ramie cellulose microfibrils. *Biomacromolecules*. 2003;4(4):1013-1017. doi:10.1021/bm025772x
48. Beck-Candanedo S, Roman M, Gray DG. Effect of reaction conditions on the properties and behavior of wood cellulose nanocrystal suspensions. *Biomacromolecules*. 2005;6(2):1048-1054. doi:10.1021/bm049300p
49. Shibazaki H, Kuga S, Okano T. *Mercerization and Acid Hydrolysis of Bacterial Cellulose*.

50. Potenza M, Bergamonti L, Lottici PP, Righi L, Lazzarini L, Graiff C. Green Extraction of Cellulose Nanocrystals of Polymorph II from Cynara scolymus L.: Challenge for a “Zero Waste” Economy. *Crystals (Basel)*. 2022;12(5). doi:10.3390/cryst12050672

51. Fan XM, Yu HY, Wang DC, Mao ZH, Yao J, Tam KC. Facile and Green Synthesis of Carboxylated Cellulose Nanocrystals as Efficient Adsorbents in Wastewater Treatments. *ACS Sustain Chem Eng*. 2019;7(21):18067-18075. doi:10.1021/acssuschemeng.9b05081

52. Ruiz-Palomero C, Soriano ML, Valcárcel M. β-Cyclodextrin decorated nanocellulose: A smart approach towards the selective fluorimetric determination of danofloxacin in milk samples. *Analyst*. 2015;140(10):3431-3438. doi:10.1039/c4an01967a

53. Zielińska A, Skwarek E, Zaleska A, Gazda M, Hupka J. Preparation of silver nanoparticles with controlled particle size. In: *Procedia Chemistry*. Vol 1. ; 2009:1560-1566. doi:10.1016/j.proche.2009.11.004

54. Popescu CM, Singurel G, Popescu MC, Vasile C, Argyropoulos DS, Willför S. Vibrational spectroscopy and X-ray diffraction methods to establish the differences between hardwood and softwood. *Carbohydr Polym*. 2009;77(4):851-857. doi:10.1016/j.carbpol.2009.03.011

55. Segal L; CJJ; MAE; CCM. An Empirical Method for Estimating the Degree of Crystallinity of Native Cellulose Using the X-ray Diffractometer. *Text Res J*. 1959;29(10):786-794.

56. French AD, Santiago Cintrón M. Cellulose polymorphy, crystallite size, and the Segal Crystallinity Index. *Cellulose*. 2013;20(1):583-588. doi:10.1007/s10570-012-9833-y

57. Habibi Y, Chanzy H, Vignon MR. TEMPO-mediated surface oxidation of cellulose whiskers. *Cellulose*. 2006;13(6):679-687. doi:10.1007/s10570-006-9075-y

58. Larsson PT, WK, & IT. A CP/MAS13C NMR investigation of molecular ordering in celluloses. *Carbohydr Res*. 1997;302(1-2):19-25.
59. Bhattacharjee S. DLS and zeta potential - What they are and what they are not? *Journal of Controlled Release*. 2016;235:337-351. doi:10.1016/j.jconrel.2016.06.017
60. Beck S, Méthot M, Bouchard J. General procedure for determining cellulose nanocrystal sulfate half-ester content by conductometric titration. *Cellulose*. 2015;22(1):101-116. doi:10.1007/s10570-014-0513-y
61. Zhong L, Fu S, Peng X, Zhan H, Sun R. Colloidal stability of negatively charged cellulose nanocrystalline in aqueous systems. *Carbohydr Polym*. 2012;90(1):644-649. doi:10.1016/j.carbpol.2012.05.091
62. Agarwal UP, Ralph SA, Reiner RS, Baez C. Probing crystallinity of never-dried wood cellulose with Raman spectroscopy. *Cellulose*. 2016;23(1):125-144. doi:10.1007/s10570-015-0788-7
63. Cael JJ, Gardner KH, Koenig JL, Blackwell J. Infrared and Raman spectroscopy of carbohydrates. Paper V Normal coordinate analysis of cellulose I. *J Chem Phys*. 1975;62(3):1145-1153. doi:10.1063/1.430558
64. Lee CM, Kafle K, Belias DW, et al. Comprehensive analysis of cellulose content, crystallinity, and lateral packing in Gossypium hirsutum and Gossypium barbadense cotton fibers using sum frequency generation, infrared and Raman spectroscopy, and X-ray diffraction. *Cellulose*. 2015;22(2):971-989. doi:10.1007/s10570-014-0535-5
65. Oh SY, Dong IY, Shin Y, et al. Crystalline structure analysis of cellulose treated with sodium hydroxide and carbon dioxide by means of X-ray diffraction and FTIR spectroscopy. *Carbohydr Res*. 2005;340(15):2376-2391. doi:10.1016/j.carres.2005.08.007

66. Makarem M, Lee CM, Kafle K, et al. Probing cellulose structures with vibrational spectroscopy. *Cellulose*. 2019;26(1):35-79. doi:10.1007/s10570-018-2199-z

67. Maiti S, Jayaramudu J, Das K, et al. Preparation and characterization of nano-cellulose with new shape from different precursor. *Carbohydr Polym*. 2013;98(1):562-567. doi:10.1016/j.carbpol.2013.06.029

68. Mandal A, Chakrabarty D. Isolation of nanocellulose from waste sugarcane bagasse (SCB) and its characterization. *Carbohydr Polym*. 2011;86(3):1291-1299. doi:10.1016/j.carbpol.2011.06.030

69. Bergamonti L, Berzolla A, Chiappini E, et al. Polyamidoamines (PAAs) functionalized with siloxanes as wood preservatives against fungi and insects. *Holzforschung*. 2017;71(1):65-75. doi:10.1515/hf-2016-0010

70. Bergamonti L, Graiff C, Tegoni M, et al. Facile preparation of functionalized poly(amidoamine)s with biocidal activity on wood substrates. *Eur Polym J*. 2019;116:232-241. doi:10.1016/j.eurpolymj.2019.04.027

71. Oh SY, Yoo D il, Shin Y, Seo G. FTIR analysis of cellulose treated with sodium hydroxide and carbon dioxide. *Carbohydr Res*. 2005;340(3):417-428. doi:10.1016/j.carres.2004.11.027

72. Široký J, Blackburn RS, Bechtold T, Taylor J, White P. Attenuated total reflectance Fourier-transform Infrared spectroscopy analysis of crystallinity changes in lyocell following continuous treatment with sodium hydroxide. *Cellulose*. 2010;17(1):103-115. doi:10.1007/s10570-009-9378-x

73. Maréchal Y, Chanzy H. *The Hydrogen Bond Network in I b Cellulose as Observed by Infrared Spectrometry*. www.elsevier.nl/locate/molstruc

74. Nada AMA, Hassan ML. *Thermal Behavior of Cellulose and Some Cellulose Derivatives*.

75. Goswami P, Blackburn RS, El-Dessouky HM, Taylor J, White P. Effect of sodium hydroxide pre-treatment on the optical and structural properties of lyocell. *Eur Polym J*. 2009;45(2):455-465. doi:10.1016/j.eurpolymj.2008.10.030

76. di Maggio R, Dirè S, Callone E, et al. Super-adsorbent polyacrylate under swelling in water for passive solar control of building envelope. *SN Appl Sci*. 2020;2(1). doi:10.1007/s42452-019-1814-4

77. Zhao D, Deng Y, Han D, et al. Exploring structural variations of hydrogen-bonding patterns in cellulose during mechanical pulp refining of tobacco stems. *Carbohydr Polym*. 2019;204:247-254. doi:10.1016/j.carbpol.2018.10.024

78. Eyholzer C, Bordeanu N, Lopez-Suevos F, Rentsch D, Zimmermann T, Oksman K. Preparation and characterization of water-redispersible nanofibrillated cellulose in powder form. *Cellulose*. 2010;17(1):19-30. doi:10.1007/s10570-009-9372-3

79. Pottathara YB, Bobnar V, Gorgieva S, et al. Mechanically strong, flexible and thermally stable graphene oxide/nanocellulosic films with enhanced dielectric properties. *RSC Adv*. 2016;6(54):49138-49149. doi:10.1039/c6ra06744a

80. Cai D, Neyer A, Kuckuk R, Heise HM. Raman, mid-infrared, near-infrared and ultraviolet-visible spectroscopy of PDMS silicone rubber for characterization of polymer optical waveguide materials. *J Mol Struct*. 2010;976(1-3):274-281. doi:10.1016/j.molstruc.2010.03.054

81. Nishiyama Y, Sugiyama J, Chanzy H, Langan P. Crystal Structure and Hydrogen Bonding System in Cellulose Iα from Synchrotron X-ray and Neutron Fiber Diffraction. *J Am Chem Soc*. 2003;125(47):14300-14306. doi:10.1021/ja037055w

82. Nishiyama Y, Langan P, Chanzy H. Crystal structure and hydrogen-bonding system in cellulose Iβ from synchrotron X-ray and neutron fiber diffraction. *J Am Chem Soc*. 2002;124(31):9074-9082. doi:10.1021/ja0257319

83. Langan P, Nishiyama Y, Chanzy H. X-ray structure of mercerized cellulose II at 1 Å resolution. *Biomacromolecules*. 2001;2(2):410-416. doi:10.1021/bm005612q

84. French AD, Santiago Cintrón M. Cellulose polymorphy, crystallite size, and the Segal Crystallinity Index. *Cellulose*. 2013;20(1):583-588. doi:10.1007/s10570-012-9833-y

85. Bates S, Zografi G, Engers D, Morris K, Crowley K, Newman A. Analysis of amorphous and nanocrystalline solids from their X-ray diffraction patterns. *Pharm Res*. 2006;23(10):2333-2349. doi:10.1007/s11095-006-9086-2

86. Lu H, Gui Y, Zheng L, Liu X. Morphological, crystalline, thermal and physicochemical properties of cellulose nanocrystals obtained from sweet potato residue. *Food Research International*. 2013;50(1):121-128. doi:10.1016/j.foodres.2012.10.013

87. Chieng BW, Lee SH, Ibrahim NA, Then YY, Loo YY. Isolation and characterization of cellulose nanocrystals from oil palm mesocarp fiber. *Polymers (Basel)*. 2017;9(8). doi:10.3390/polym9080355

88. Wang N, Ding E, Cheng R. Thermal degradation behaviors of spherical cellulose nanocrystals with sulfate groups. *Polymer (Guildf)*. 2007;48(12):3486-3493. doi:10.1016/j.polymer.2007.03.062

89. Jin E, Guo J, Yang F, et al. On the polymorphic and morphological changes of cellulose nanocrystals (CNC-I) upon mercerization and conversion to CNC-II. *Carbohydr Polym*. 2016;143:327-335. doi:10.1016/j.carbpol.2016.01.048

90. Johar N, Ahmad I, Dufresne A. Extraction, preparation and characterization of cellulose fibres and nanocrystals from rice husk. *Ind Crops Prod*. 2012;37(1):93-99. doi:10.1016/j.indcrop.2011.12.016
91. Sun X, He Q, Yang Y. Preparation of dicarboxyl cellulose nanocrystals from agricultural wastes by sequential periodate-chlorite oxidation. *J Renew Mater*. 2020;8(4):447-460. doi:10.32604/jrm.2020.09671
92. Vanderfleet OM, Reid MS, Bras J, et al. Insight into thermal stability of cellulose nanocrystals from new hydrolysis methods with acid blends. *Cellulose*. 2019;26(1):507-528. doi:10.1007/s10570-018-2175-7
93. Saito T, Isogai A. TEMPO-mediated oxidation of native cellulose. The effect of oxidation conditions on chemical and crystal structures of the water-insoluble fractions. *Biomacromolecules*. 2004;5(5):1983-1989. doi:10.1021/bm0497769
94. Lu P, Hsieh Y lo. Preparation and properties of cellulose nanocrystals: Rods, spheres, and network. *Carbohydr Polym*. 2010;82(2):329-336. doi:10.1016/j.carbpol.2010.04.073
95. Atalla RH, Vanderhart DL. *The Role of Solid State 13 C NMR Spectroscopy in Studies of the Nature of Native Celluloses*. Vol 15. www.elsevier.nlrlocatersolmag
96. J Polym Sci GA, Earl WL, VanderHart DL. *"Proton and Carbon-13 NMR Observations by High-Resolution Carbon-13 Nuclear Magnetic Resonance of Cellulose I Related to Morphology and Crystal Structure*. Vol 14. American Chemical Society; 1981. https://pubs.acs.org/sharingguidelines
97. Atalla RH, Vanderhart DL. *Native Cellulose: A Composite of Two Distinct Crystalline Forms*. Vol 223.; 1984.

98. Agarwal UP, Reiner RS, Ralph SA, et al. Characterization of the supramolecular structures of cellulose nanocrystals of different origins. *Cellulose*. 2021;28(3):1369-1385. doi:10.1007/s10570-020-03590-z

99. Larsson T, Wickholm K, Iversen T. *A CP/MAS 13C NMR Investigation of Molecular Ordering in Celluloses*. Vol 302.; 1997.

100. Wickholm K, Larsson T, Iversen T. *Assignment of Non-Crystalline Forms in Cellulose I by CP/MAS 13 C NMR Spectroscopy*.

101. Hult EL, Larsson T, Iversen T. *A Comparative CP/MAS 13 C-NMR Study of Cellulose Structure in Spruce Wood and Kraft Pulp*. Vol 7.; 2000.

102. Pu Y, Ziemer C, Ragauskas AJ. CP/MAS 13C NMR analysis of cellulase treated bleached softwood kraft pulp. *Carbohydr Res*. 2006;341(5):591-597. doi:10.1016/j.carres.2005.12.012

103. Larsson T, Westermark U, Iversen T. *Determination of the Cellulose I a Allomorph Content in a Tunicate Cellulose by CP/MAS 13C_NMR Spectroscopy*. Vol 278.; 1995.

104. Yamamoto H, Horii F. *CP/MAS 13C NMR Analysis of the Crystal Transformation Induced for Valonia Cellulose by Annealing at High Temperatures*. Vol 26.; 1993. https://pubs.acs.org/sharingguidelines

105. Kono H, Yunoki S, Shikano T, Fujiwara M, Erata T, Takai M. CP/MAS 13C NMR study of cellulose and cellulose derivatives. 1 . Complete assignment of the CP/MAS 13C NMR spectrum of the native cellulose. *J Am Chem Soc*. 2002;124(25):7506-7511. doi:10.1021/ja010704o

106. Newman RH. *Estimation of the Lateral Dimensions of Cellulose Crystallites Using 13 C NMR Signal Strengths*. Vol 15. www.elsevier.nlrlocatersolmag

107. Park S, Baker JO, Himmel ME, Parilla PA, Johnson DK. *Open Access RESEARCH Cellulose Crystallinity Index: Measurement Techniques and*

Their Impact on Interpreting Cellulase Performance.; 2010. http://www.biotechnologyforbiofuels.com/content/3/1/10

108. Geppi M, Forte C. *The SPORT-NMR Software: A Tool for Determining Relaxation Times in Unresolved NMR Spectra*.; 1999. http://www.idealibrary.com
109. Cui Q, Zheng Y, Lin Q, Song W, Qiao K, Liu S. Selective oxidation of bacterial cellulose by NO2-HNO 3. *RSC Adv*. 2014;4(4):1630-1639. doi:10.1039/c3ra44516j
110. Liu P, Pang B, Tian L, et al. Efficient, Self-Terminating Isolation of Cellulose Nanocrystals through Periodate Oxidation in Pickering Emulsions. *ChemSusChem*. 2018;11(20):3581-3585. doi:10.1002/cssc.201801678
111. Lal SS, Mhaske ST. TEMPO-oxidized cellulose nanofiber/kafirin protein thin film crosslinked by Maillard reaction. *Cellulose*. 2019;26(10):6099-6118. doi:10.1007/s10570-019-02509-7
112. Kumar A, Durand H, Zeno E, et al. The surface chemistry of a nanocellulose drug carrier unravelled by MAS-DNP. *Chem Sci*. 2020;11(15):3868-3877. doi:10.1039/c9sc06312a
113. Pettignano A, Charlot A, Fleury E. Solvent-free synthesis of amidated carboxymethyl cellulose derivatives: Effect on the thermal properties. *Polymers (Basel)*. 2019;11(7). doi:10.3390/polym11071227
114. Ruparelia JP, Chatterjee AK, Duttagupta SP, Mukherji S. Strain specificity in antimicrobial activity of silver and copper nanoparticles. *Acta Biomater*. 2008;4(3):707-716. doi:10.1016/j.actbio.2007.11.006
115. Zhang X, Sun H, Tan S, Gao J, Fu Y, Liu Z. Hydrothermal synthesis of Ag nanoparticles on the nanocellulose and their antibacterial study. *Inorg Chem Commun*. 2019;100:44-50. doi:10.1016/j.inoche.2018.12.012

116. Isca C, di Maggio R, Pajares Collado N, Predieri G, Lottici PP. The use of polyamidoamines for the conservation of iron-gall inked paper. *Cellulose*. 2019;26(2):1277-1296. doi:10.1007/s10570-018-2105-8
117. Girardi F, Bergamonti L, Isca C, et al. Chemical–physical characterization of ancient paper with functionalized polyamidoamines (PAAs). *Cellulose*. 2017;24(2):1057-1068. doi:10.1007/s10570-016-1159-8
118. Simão CD, Reparaz JS, Wagner MR, et al. Optical and mechanical properties of nanofibrillated cellulose: Toward a robust platform for next-generation green technologies. *Carbohydr Polym*. 2015;126:40-46. doi:10.1016/j.carbpol.2015.03.032
119. Dufresne A. Nanocellulose: A new ageless bionanomaterial. *Materials Today*. 2013;16(6):220-227. doi:10.1016/j.mattod.2013.06.004
120. Xu Q, Jin L, Wang Y, Chen H, Qin M. Synthesis of silver nanoparticles using dialdehyde cellulose nanocrystal as a multi-functional agent and application to antibacterial paper. *Cellulose*. 2019;26(2):1309-1321. doi:10.1007/s10570-018-2118-3
121. Amini E, Azadfallah M, Layeghi M, Talaei-Hassanloui R. Silver-nanoparticle-impregnated cellulose nanofiber coating for packaging paper. *Cellulose*. 2016;23(1):557-570. doi:10.1007/s10570-015-0846-1
122. Martins NCT, Freire CSR, Pinto RJB, et al. Electrostatic assembly of Ag nanoparticles onto nanofibrillated cellulose for antibacterial paper products. *Cellulose*. 2012;19(4):1425-1436. doi:10.1007/s10570-012-9713-5
123. Cocca M, D'Arienzo L, D'Orazio L. Effects of Different Artificial Agings on Structure and Properties of Whatman Paper Samples. *ISRN Materials Science*. 2011;2011:1-7. doi:10.5402/2011/863083

124. TAPPI T 494 (2001). Tensile properties of paper and paperboard (using constant rate of elongation apparatus). (Revision of T 494 om-01). Technical association of the pulp and paper industry, Atlanta.
125. Ebert B, Singer B, Grimaldi N. Aquazol as a consolidant for matte paint on Vietnamese paintings. *Journal of the Institute of Conservation*. 2012;35(1):62-76. doi:10.1080/19455224.2012.672813
126. la Nasa J, di Marco F, Bernazzani L, et al. Aquazol as a binder for retouching paints. An evaluation through analytical pyrolysis and thermal analysis. *Polym Degrad Stab*. 2017;144:508-519. doi:10.1016/j.polymdegradstab.2017.09.007
127. Ghezzi L, Duce C, Bernazzani L, et al. Interactions between inorganic pigments and rabbit skin glue in reference paint reconstructions. *J Therm Anal Calorim*. 2015;122(1):315-322. doi:10.1007/s10973-015-4759-x
128. Vahur S, Teearu A, Peets P, Joosu L, Leito I. ATR-FT-IR spectral collection of conservation materials in the extended region of 4000-80 cm–1. *Anal Bioanal Chem*. 2016;408(13):3373-3379. doi:10.1007/s00216-016-9411-5
129. Vetter W, Schreiner M. *Characterization of Pigment-Binding Media Systems - Comparison of Non-Invasive In-Situ Reflection FTIR with Transmission FTIR Microscopy*. www.e-PRESERVATIONScience.org
130. Anbalagan G, Mukundakumari S, Murugesan KS, Gunasekaran S. Infrared, optical absorption, and EPR spectroscopic studies on natural gypsum. *Vib Spectrosc*. 2009;50(2):226-230. doi:10.1016/j.vibspec.2008.12.004
131. la Russa MF, Ruffolo SA, Barone G, Crisci GM, Mazzoleni P, Pezzino A. The Use of FTIR and Micro-FTIR Spectroscopy: An Example of Application to Cultural Heritage. *Int J Spectrosc*. 2009;2009:1-5. doi:10.1155/2009/893528

132. Genestar C, Pons C. Earth pigments in painting: Characterisation and differentiation by means of FTIR spectroscopy and SEM-EDS microanalysis. In: *Analytical and Bioanalytical Chemistry*. Vol 382. ; 2005:269-274. doi:10.1007/s00216-005-3085-8

133. Łojewska J, Miśkowiec P, Łojewski T, Proniewicz LM. Cellulose oxidative and hydrolytic degradation: In situ FTIR approach. *Polym Degrad Stab*. 2005;88(3):512-520. doi:10.1016/j.polymdegradstab.2004.12.012

134. Zeng X, Vishtal A, Retulainen E, Sivonen E, Fu S. *Elongation of Paper*. Vol 8.; 2013.

135. Fouda A, Abdel-Maksoud G, Abdel-Rahman MA, Eid AM, Barghoth MG, El-Sadany MAH. Monitoring the effect of biosynthesized nanoparticles against biodeterioration of cellulose-based materials by Aspergillus niger. *Cellulose*. 2019;26(11):6583-6597. doi:10.1007/s10570-019-02574-y

136. Ma X, Li R, Zhao X, et al. Biopolymer composite fibres composed of calcium alginate reinforced with nanocrystalline cellulose. *Compos Part A Appl Sci Manuf*. 2017;96:155-163. doi:10.1016/j.compositesa.2017.02.021

137. Jorfi M, Foster EJ. Recent advances in nanocellulose for biomedical applications. *J Appl Polym Sci*. 2015;132(14). doi:10.1002/app.41719

138. Zheng X, Liu T, Guo M, et al. Impact of heavy metals on the formation and properties of solvable microbiological products released from activated sludge in biological wastewater treatment. *Water Res*. 2020;179. doi:10.1016/j.watres.2020.115895

139. Gorgieva S, Vogrinčič R, Kokol V. The Effect of Membrane Structure Prepared from Carboxymethyl Cellulose and Cellulose Nanofibrils for Cationic Dye Removal. *J Polym Environ*. 2019;27(2):318-332. doi:10.1007/s10924-018-1341-1

140. Vardhan KH, Kumar PS, Panda RC. A review on heavy metal pollution, toxicity and remedial measures: Current trends and future perspectives. *J Mol Liq*. 2019;290. doi:10.1016/j.molliq.2019.111197

141. Fu F, Wang Q. Removal of heavy metal ions from wastewaters: A review. *J Environ Manage*. 2011;92(3):407-418. doi:10.1016/j.jenvman.2010.11.011

142. Mäntele W, Deniz E. UV–VIS absorption spectroscopy: Lambert-Beer reloaded. *Spectrochim Acta A Mol Biomol Spectrosc*. 2017;173:965-968. doi:10.1016/j.saa.2016.09.037

143. Rudzinski W, Plazinski W. Kinetics of solute adsorption at solid/aqueous interfaces: Searching for the theoretical background of the modified pseudo-first-order kinetic equation. *Langmuir*. 2008;24(10):5393-5399. doi:10.1021/la8000448

144. Franca AS, Oliveira LS, Ferreira ME. Kinetics and equilibrium studies of methylene blue adsorption by spent coffee grounds. *Desalination*. 2009;249(1):267-272. doi:10.1016/j.desal.2008.11.017

145. Simonin JP. On the comparison of pseudo-first order and pseudo-second order rate laws in the modeling of adsorption kinetics. *Chemical Engineering Journal*. 2016;300:254-263. doi:10.1016/j.cej.2016.04.079

146. Azizian S. Kinetic models of sorption: A theoretical analysis. *J Colloid Interface Sci*. 2004;276(1):47-52. doi:10.1016/j.jcis.2004.03.048

147. Ho YS, McKay G. A Comparison of chemisorption kinetic models applied to pollutant removal on various sorbents. *Process Safety and Environmental Protection*. 1998;76(4):332-340. doi:10.1205/095758298529696

148. Najafi Nobar S, Farooq S. Experimental and modeling study of adsorption and diffusion of gases in Cu-BTC. *Chem Eng Sci*. 2012;84:801-813. doi:10.1016/j.ces.2012.05.022

149. Zhang N, Zang GL, Shi C, Yu HQ, Sheng GP. A novel adsorbent TEMPO-mediated oxidized cellulose nanofibrils modified with PEI: Preparation, characterization, and application for Cu(II) removal. *J Hazard Mater*. 2016;316:11-18. doi:10.1016/j.jhazmat.2016.05.018

150. Ho YS. Second-order kinetic model for the sorption of cadmium onto tree fern: A comparison of linear and non-linear methods. *Water Res*. 2006;40(1):119-125. doi:10.1016/j.watres.2005.10.040

151. Ho YS, Mckay G. *Pseudo-Second Order Model for Sorption Processes*. Vol 34.; 1999.

152. Revellame ED, Fortela DL, Sharp W, Hernandez R, Zappi ME. Adsorption kinetic modeling using pseudo-first order and pseudo-second order rate laws: A review. *Clean Eng Technol*. 2020;1. doi:10.1016/j.clet.2020.100032

153. Tan KL, Hameed BH. Insight into the adsorption kinetics models for the removal of contaminants from aqueous solutions. *J Taiwan Inst Chem Eng*. 2017;74:25-48. doi:10.1016/j.jtice.2017.01.024

154. Robati D. Pseudo-second-orders kinetic equations for modeling adsorption systems for removal of lead ions using multi-walled carbon nanotube. *J Nanostructure Chem*. 2013;3(1). doi:10.1186/2193-8865-3-55

155. Biemer JJ. *A n Tim Icrobial Susceptibility Testing by the K Irb Y-B Au Er Disc Diffusion M Ethod*.

156. Crini G, Badot PM. Application of chitosan, a natural aminopolysaccharide, for dye removal from aqueous solutions by adsorption processes using batch studies: A review of recent literature. *Progress in Polymer Science (Oxford)*. 2008;33(4):399-447. doi:10.1016/j.progpolymsci.2007.11.001

157. J P Williams BR. THE STABILITY OF COMPLEX IONS WITH SPECIAL REFERENCE TO HYDRATION. *Trans Faraday Soc*. 1954;56(4):121-126. doi:10.3

158. Khan M, Bouet G, Vierling F, Meullemeestre J, Sehwing MJ. Formation of cobalt(II), nickel(II) and copper(II) chloro complexes in alcohols and the Irving-Williams order of stabilities Formation of cobalt(II), nickel(II) and copper(II) chloro com-plexes in alcohols and the Irving-Williams order of stabilities. *Transition Metal Chemistry*. 1996;21:231-234. doi:10.1007/BF00165973ï

159. Fahim Huseien G, Mirza J, Ismail M, Ghoshal SK, Abdulameer Hussein A. Geopolymer mortars as sustainable repair material: A comprehensive review. *Renewable and Sustainable Energy Reviews*. 2017;80:54-74. doi:10.1016/j.rser.2017.05.076

160. Okoye FN. *Geopolymer Binder: A Veritable Alternative to Portland Cement-Review under Responsibility of INTERNATIONAL CONFERENCE ON MULTIFUNCTIONAL MATERIALS FOR DEVICE APPLICATIONS(ICMDA-2016)*. Vol 4.; 2017. www.sciencedirect.comwww.materialstoday.com/proceedings2214-7853

161. Bergamonti L, Taurino R, Cattani L, Ferretti D, Bondioli F. Lightweight hybrid organic-inorganic geopolymers obtained using polyurethane waste. *Constr Build Mater*. 2018;185:285-292. doi:10.1016/j.conbuildmat.2018.07.006

162. Zhang P, Zheng Y, Wang K, Zhang J. A review on properties of fresh and hardened geopolymer mortar. *Compos B Eng*. 2018;152:79-95. doi:10.1016/j.compositesb.2018.06.031

163. Carreño-Gallardo C, Tejeda-Ochoa A, Perez-Ordonez OI, et al. In the CO2 emission remediation by means of alternative geopolymers as substitutes

for cements. *J Environ Chem Eng*. 2018;6(4):4878-4884. doi:10.1016/j.jece.2018.07.033

164. Singh NB, Middendorf B. Geopolymers as an alternative to Portland cement: An overview. *Constr Build Mater*. 2020;237. doi:10.1016/j.conbuildmat.2019.117455
165. Xu H, van Deventer JSJ. *The Geopolymerisation of Alumino-Silicate Minerals*. Vol 59.; 2000. www.elsevier.nlrlocaterijminpro
166. Swanepoel JC, Strydom CA. *Utilisation of Fly Ash in a Geopolymeric Material*. www.elsevier.com/locate/apgeochem
167. Mehta A, Siddique R. An overview of geopolymers derived from industrial by-products. *Constr Build Mater*. 2016;127:183-198. doi:10.1016/j.conbuildmat.2016.09.136
168. Davidovitis 89.
169. Ricciotti L, Molino AJ, Roviello V, Chianese E, Cennamo P, Roviello G. Geopolymer composites for potential applications in cultural heritage. *Environments - MDPI*. 2017;4(4):1-15. doi:10.3390/environments4040091
170. Jantzen CM, Lee WE, Ojovan MI. *Chapter 7 in Radioactive Waste Management and SRNL-STI-2012-00407 Contaminated Site Clean-up: Processes, Technologies and International Experience-1-Radioactive Waste Conditioning, Immobilisation, and Encapsulation Processes and Technologies: Overview and Advances*.
171. Jamieson EJ, Penna B, van Riessen A, Nikraz H. The development of Bayer derived geopolymers as artificial aggregates. *Hydrometallurgy*. 2017;170:74-81. doi:10.1016/j.hydromet.2016.05.001
172. Perná I, Hanzlíček T. The solidification of aluminum production waste in geopolymer matrix. *J Clean Prod*. 2014;84(1):657-662. doi:10.1016/j.jclepro.2014.04.043

173. Dong M, Elchalakani M, Karrech A. Development of high strength one-part geopolymer mortar using sodium metasilicate. *Constr Build Mater*. 2020;236. doi:10.1016/j.conbuildmat.2019.117611
174. Ouyang S, Chen W, Zhang Z, Li X, Zhu W. Experimental study of one-part geopolymer using different alkali sources. In: *Journal of Physics: Conference Series*. Vol 1605. Institute of Physics Publishing; 2020. doi:10.1088/1742-6596/1605/1/012155
175. Zhang HY, Liu JC, Wu B. Mechanical properties and reaction mechanism of one-part geopolymer mortars. *Constr Build Mater*. 2021;273. doi:10.1016/j.conbuildmat.2020.121973
176. Provis JL. Alkali-activated materials. *Cem Concr Res*. 2018;114:40-48. doi:10.1016/j.cemconres.2017.02.009
177. Nematollahi B, Sanjayan J, Shaikh FUA. Synthesis of heat and ambient cured one-part geopolymer mixes with different grades of sodium silicate. *Ceram Int*. 2015;41(4):5696-5704. doi:10.1016/j.ceramint.2014.12.154
178. Nawaz M, Heitor A, Sivakumar M. Geopolymers in construction - recent developments. *Constr Build Mater*. 2020;260. doi:10.1016/j.conbuildmat.2020.120472
179. Shehata N, Sayed ET, Abdelkareem MA. Recent progress in environmentally friendly geopolymers: A review. *Science of the Total Environment*. 2021;762. doi:10.1016/j.scitotenv.2020.143166
180. Michelini E, Ferretti D, Pagliari F, et al. Fracture energy of sustainable geopolymer composites with and without the addition of slaughterhouse by-products as fibre-reinforcement: An experimental investigation. In: *Procedia Structural Integrity*. Vol 39. Elsevier B.V.; 2021:71-80. doi:10.1016/j.prostr.2022.03.074
181. Haach VG, Vasconcelos G, Loureno PB. Influence of aggregates grading and water/cement ratio in workability and hardened properties of mortars.

Constr Build Mater. 2011;25(6):2980-2987. doi:10.1016/j.conbuildmat.2010.11.011

182. EN 998-2 2016. Specification for mortar for masonry - Part 2: Masonry mortar.
183. EN 1015-11 2019. Methods of Test for Mortar for Masonry - Part 11: Determination of Flexural and Compressive Strength of Hardened Mortar.
184. EN1015-12 2016. Methods of test for mortar for masonry - Part 12: Determination of adhesive strength of hardened rendering and plastering mortars on substrates.
185. Simonsen ME, Sønderby C, Li Z, Søgaard EG. XPS and FT-IR investigation of silicate polymers. *J Mater Sci*. 2009;44(8):2079-2088. doi:10.1007/s10853-009-3270-9
186. Wang D, Mousavi P, Hauser PJ, Oxenham W, Grant CS. Quartz crystal microbalance in elevated temperature viscous liquids: Temperature effect compensation and lubricant degradation monitoring. *Colloids Surf A Physicochem Eng Asp*. 2005;268(1-3):30-39. doi:10.1016/j.colsurfa.2005.05.075
187. Bortnovsky O, Dědeček J, Tvarůžková Z, Sobalík Z, Šubrt J. Metal ions as probes for characterization of geopolymer materials. *Journal of the American Ceramic Society*. 2008;91(9):3052-3057. doi:10.1111/j.1551-2916.2008.02577.x
188. Provis JL, Lukey GC, van Deventer JSJ. Do geopolymers actually contain nanocrystalline zeolites? a reexamination of existing results. *Chemistry of Materials*. 2005;17(12):3075-3085. doi:10.1021/cm050230i
189. Chen L, Wang Z, Wang Y, Feng J. Preparation and properties of alkali activated metakaolin-based geopolymer. *Materials*. 2016;9(9). doi:10.3390/ma9090767

190. Palmero P, Formia A, Antonaci P, Brini S, Tulliani JM. Geopolymer technology for application-oriented dense and lightened materials. Elaboration and characterization. *Ceram Int*. 2015;41(10):12967-12979. doi:10.1016/j.ceramint.2015.06.140

191. Kakali G, Perraki T, Tsivilis S, Badogiannis E. *Thermal Treatment of Kaolin: The Effect of Mineralogy on the Pozzolanic Activity*. Vol 20.; 2001. www.elsevier.comrlocaterclay

192. Yunsheng Z, Wei S, Zongjin L. Composition design and microstructural characterization of calcined kaolin-based geopolymer cement. *Appl Clay Sci*. 2010;47(3-4):271-275. doi:10.1016/j.clay.2009.11.002

193. Rees CA, Provis JL, Lukey GC, van Deventer JSJ. In situ ATR-FTIR study of the early stages of fly ash geopolymer gel formation. *Langmuir*. 2007;23(17):9076-9082. doi:10.1021/la701185g

Acknowledgements

The PhD activity was made possible thanks to the collaboration of numerous professional figures. I want to thank Cariparma foundation for funding the research, Davines s.p.a. (A.D. dott. Paolo Goi), EKORU s.r.l. (Volla NA) for demonstrating interest in the researchs conducted. To develop PON project "Ricerca e Sviluppo di nuovi materiali avanzati per costruzioni eco-sostenibili, con caratteristiche di elevata efficienza energetica e sicurezza anti sismica, da ottenersi con sistemi avanzati di produzione ad alte prestazioni, efficienti ed ecocompatibili" Programma Operativo Nazionale «Imprese e Competitività» 2014- 2020 FESR numero F/090017/00/X36, CUP B18l17000450008, the collaboration with prof. Daniele Ferreti, prof.ssa Elena Michelini (Department of Engineering and Architecture, Università di Parma) and dott. Francesco Talento (Bacchi s.p.a.) was foundamental. Thanks to Studio MM s.r.l. (CEO dott. Michele Mazzoni) for the study of geopolymeric materials. The antibacterial activity was made possible thank to prof.ssa Anna Maria Sanangelantoni (Department of Chemistry, Life Science and Environmental Sustainability, Università di Parma), proff.ssa Maria Cristina Ossiprandi and dott.ssa Cinzia Reverberi (Department of Veterinary Science, Università di Parma). Thanks to prof. Ruggero Bettini and prof.ssa Lisa Elviri (Food and drug department, Università di Parma) for the creation of 3D scaffolds. The Raman spectroscopy analysis was made in collaboration with prof. Pier Paolo Lottici and prof. Danilo Bersani (Department of Mathematical, Physical and Computer Sciences, Università di Parma). Thanks to prof.ssa Lara Righi and prof. Matteo Tegoni (Department of Chemistry, Life Science and Environmental Sustainability, Università di Parma) for the scientific support.

I want thank to dott. Laura Lazzarini (Institute of Materials for Electronics and Magnetism, National Research Council, IMEM-CNR, Parma) for the TEM

analysis, prof. Corrado Sciancalepore (Department of Engineering and Architecture) and dott. Luca Barchi (Department of Chemistry, Life Science and Environmental Sustainability, Università di Parma) for the SEM investigation, dott.ssa Claudia Forte and dott.ssa Lucia Calucci (Istituto di Chimica dei Composti Organometallici - Consiglio Nazionale delle Ricerche, ICCOM-CNR, Pisa) for the SSNMR analysis, dott.ssa Roberta Magnani (Department of Chemistry, Life Science and Environmental Sustainability, Università di Parma) for XRPD and TGA investigation, dott. Gianfranco Galli (Department of Mathematical, Physical and Computer Sciences, Università di Parma) for the DLS measurements, prof.ssa Antonella Casoli (Department of Chemistry, Life Science and Environmental Sustainability, Università di Parma) dott. Marco Bartolini, dott.ssa Marcella Ioele, dott.ssa Barbara Lavorini, dott.ssa Patrizia Giacomazzi (Istituto Centrale del Restauro, ICR, Roma e Matera) for the research on cultural heritage.

Finally, thanks to my supervisors Prof. Claudia Graiff and Prof. Laura Bergamonti, for guided and supported me during these three years.